Physics, Performance, and Applications of Plasma Aerocapture

Charles L. Kelly

A dissertation
submitted in partial fulfillment of the
requirements for the degree of

Doctor of Philosophy

University of Washington

2021

Reading Committee:

Justin M. Little, Chair

Uri Shumlak

Mehran Mesbahi

Program Authorized to Offer Degree:
William E. Boeing Department of Aeronautics & Astronautics

University of Washington

Abstract

Physics, Performance, and Applications of Plasma Aerocapture

Charles L. Kelly

Chair of the Supervisory Committee:
Assistant Professor Justin M. Little
William E. Boeing Department of Aeronautics & Astronautics

The feasibility of magnetoshells for drag-modulated plasma aerocapture (DMPA) is investigated using analytical modeling and a novel demonstration experiment. DMPA proposes to generate drag through interaction of the atmosphere with a magnetized plasma. Instead of a rigid aeroshell, it uses a "magnetoshell" consisting of a magnetic field that confines the plasma, attaining very large effective drag area and enabling less risky flight profiles. Although there are clear advantages to magnetoshells over aeroshells, the fundamental physics of their operation is not well characterized. An understanding of these physics is needed to determine how their performance scales with spacecraft and mission design parameters and ultimately inform appropriate mission applications.

An analytical model is developed to describe the interaction of a dipole magnetic plasma with a hypersonic rarefied neutral flow, analogous to a magnetoshell in aerocapture flight. Single particle trajectory analysis reveals a characteristic ion-trapping region enclosed by a particular magnetic flux surface that drives mass and energy capture from the flow by the plasma. The capture and deflection of particles is found to produce strong forces on the magnetic field depending on the extent of the ion-trapping region and the flow reactivity with the plasma. A global model is developed and averaged over the toroidal ion-trapping volume to describe the net mass and energy exchange between the neutral stream and plasma. Simulations over a large range of magnet and freestream parameters reveal three distinct physical regimes that have significant bearing on the magnitude of plasma/flow

interaction. The transitions between these regimes exhibit characteristics of resistive critical ionization, whereby the relative kinetic energy between plasma and neutral gas collisionally heats electrons, driving rapid and complete ionization of the gas. Two regime transitions are observed with sudden exponential increases in plasma density occurring at velocity thresholds that depend on several energy loss mechanisms. The higher-velocity transition is a classical presentation of critical ionization where flow neutrals are ionized directly by plasma electrons. The other is a unique case in which charge exchange between ions and flow neutrals supplies both the particles and energy required to initiate critical ionization. This transition is distinct from any critical ionization effect reported in literature and indicates the existence of a lower critical velocity governed by collisional and diffusive effects as opposed to ionization energy losses only. The critical ionization thresholds increase the force on the magnet by up to two orders of magnitude compared to aerodynamic drag on an equivalently sized flow impediment.

The application of DMPA to outer planet orbiter missions is analyzed in terms of performance results and spacecraft design scaling. A design framework for generating preliminary DMPA mission architectures is presented and a sample design is compared to an existing Neptune orbiter concept that uses an ADEPT drag skirt. Compared to ADEPT, the DMPA architecture is shown to deliver 70% higher orbiter mass and experience 30% lower stagnation heating. It achieves a ballistic coefficient of $\beta = 4$ kg/m^2 with a ballistic coefficient ratio of $\beta_{\max}/\beta_{\min} = 67$, both results indicating a high degree of control authority via the continuous drag modulation scheme. The robustness of DMPA trajectories to perturbations in the atmospheric density and entry flight path angle is analyzed with a Monte Carlo simulation. It is found that DMPA achieves orbit within 1% of the target apoapsis on average while 93% of all cases fall within 12.5% of the target. Compared to a variable-area aeroshell, DMPA achieves lower variance in apoapsis error, a factor of ten reduction in dynamic pressure, and a factor of three reduction in stagnation heating and total heat load. These improvements may be mission-enabling by drastically easing thermal protection system requirements to sub-kW/cm^2 heat rates compatible with heritage heat shield

materials. Recommendations for using the design framework to optimize arbitrary DMPA architectures are discussed while the challenges and associated technology advancements in guidance/navigation, power, and space tethers enabling DMPA are characterized.

Key physical assumptions about energy and momentum exchange during DMPA are tested here by a novel experiment that characterizes the interaction between a hypersonic free-molecular flow and a magnetized plasma. A neutral beam source accelerates ions from a helicon plasma to a conductive plate, neutralizes them, and reflects them as a collimated flow. A hollow cathode plasma with an applied axial magnetic field of 1 kG acts as the target for the flow. It is found that interaction with the flow causes an increase in both density and temperature of the target plasma by up to a factor of two. The voltage required to operate the hollow cathode at a fixed current is reduced by up to 5% while the neutral beam is operating, suggesting power deposition by the flow. A 0-D power balance model is invoked to show that flow kinetic energy is absorbed by the plasma at a rate of up to 50% of the hollow cathode power. This power correlates strongly with the increase in electron temperature, suggesting that flow kinetic energy is converted to electron thermal energy. Deflection of the flow by the plasma is not resolved due to extraneous forces on the measurement device and uncertainties in plasma properties. Using the results found here, it is shown that the experiment can feasibly scale to demonstrate significantly higher energy and momentum transfer as required for a plasma aerocapture proof-of-concept.

TABLE OF CONTENTS

LIST OF FIGURES

LIST OF TABLES

ACKNOWLEDGMENTS

There are many people to whom I owe deep gratitude for any success I have managed in grad school. First and foremost, to my adviser, Justin Little – I will forever appreciate your mentorship, a gift you gave from day one out of nothing but passion for this vocation. You supported my growth as a student and engineer from the time you were a student yourself, through times when other mentors failed me, and finally as my professor. I consider myself lucky to have learned from you and I am proud to be among the first in a sure-to-be long line of Justin-ites that will change the world one Mathematica notebook at a time.

To James and Taylor – thank you for making our five years in Seattle genuinely fun. Taylor, you helped me realize my dream of building a satellite and challenged me to be a better engineer every step of the way. James, you inspired dreams I never knew I had, like conquering mountains and blathering into microphones. Our friendship triangle was a rock for me throughout this chapter of life, and the times the three of us spent together will always define my fondest memories of graduate school.

To my labmates – thank you for fostering an accepting, entertaining, and even sometimes intellectual space to work and grow together over these many years. Anna, you brightened many dark days and always gave me something to laugh about even when I was at my most frustrated. Peter, I never would have graduated without your help, so thank you for the fun times making lightsabers and all other sorts of cool science. Curtis, thank you for being a friend and competitor in lab, on the slopes, and everywhere in between since we started together at UW (also you owe me a muffin).

I would like to thank NASA for supporting me throughout the last three years of school and providing me some life-changing opportunities to work with amazing people. To Bob Moses and Alex Austin, thank you for opening your respective doors to me and showing me an inpsiring new side of space exploration.

To my parents – thank you for inspiring curiosity in me and always supporting me as I followed where it took me. Your confidence in me has helped me more than you know in times when I was challenged and doubted myself. To Jael – thank you for showing me a healthier life, without which I never would have finished my PhD. And above all, to Morgan – the past five years were as much a journey together as they were a personal endeavor. They have been the best of my life thanks to you. Even though we could be happy together in any place doing anything, I am grateful that you have encouraged me to pursue my passions since the beginning and I am excited for where your love and support will continue to take us in life.

DEDICATION

When ships to sail the void between the stars have been built, there will step forth men to sail these ships.

–Johannes Kepler

Chapter 1

INTRODUCTION

1.1 Motivation

Aerocapture is an orbit insertion maneuver that uses drag of a planetary atmosphere on a spacecraft to slow it from a hyperbolic trajectory to a closed elliptic orbit. Hall *et al.* have shown that aerocapture can offer significant cost reduction and increase in delivered mass to all eight solar system destinations with tangible atmospheres [1]. They also identify the maneuver as an enabling technology for missions of interest at Jupiter, Saturn, and Neptune. Several relatively mature aerocapture technologies are being developed, such as the Hypersonic Inflatable Aerodynamic Decelerator (HIAD) [2], the Adaptive Deployable Placement Technology (ADEPT) [3], and ballutes [4], yet none has ever been used on a mission because of the associated risks. These aeroshell devices rely on structures to deflect atmospheric flow and are therefore susceptible to the high heat and dynamic pressure inherent to reentry conditions. Atmospheric entry at the gas and ice giants occurs at velocities in excess of 20 km/s [5] – a recent study showed these extreme environments require advancements in thermal protection technology to implement aerocapture at Uranus and Neptune, while Jupiter and Saturn are not feasible destinations for aeroshells in the near term [6].

One mitigation strategy is the use of drag modulation, whereby the drag area of the entry vehicle is modified inside the atmosphere to target a final orbit more accurately. Simulations have shown that schemes involving staged jettisoning of aeroshell devices (such as [7, 8]) result in greater final orbit accuracy, with the benefit increasing the more one can control the ballistic coefficient [9]. The highest-performing drag modulation scheme is one that can achieve continuous, bidirectional control of a large range of ballistic coefficient values. However, modern aeroshell devices have no reliable mechanism for implementing this type of control.

Drag-modulated plasma aerocapture (DMPA) is an alternative approach that proposes to generate drag through interaction of the atmosphere with a magnetized plasma [10]. Instead of a rigid aeroshell, it uses a "magnetoshell" consisting of a magnetic field that confines the plasma (Fig. 1.1). The device may be either fixed to the spacecraft or towed behind it in a parachute-like configuration. Drag is produced when an atmospheric neutral becomes an ion through charge exchange (CX) or electron-impact ionization. The new ion imparts momentum on the spacecraft when it is either magnetically deflected or confined in the plasma. Though each individual particle produces a minuscule force, the aim is for production of new ions from the flow to be so widespread that significant macroscopic drag can occur. The magnetic field strength controls plasma confinement, affecting the magnitude of the interaction and therefore the drag force. Controlling the magnetic field strength is a matter of adjusting the current applied to an electromagnet, so the drag force can be modulated continuously without moving parts.

Fig. 1.2 shows the general architecture of a DMPA maneuver. The spacecraft arrives at the atmosphere along a hyperbolic orbit. Once in the atmosphere, the magnetoshell is activated by powering the magnet and injecting plasma to seed interaction with the flow. Like a ballute [4], the device may be fixed to the spacecraft or trailed behind it (Fig. 1.2 depicts a trailing configuration). The ballistic coefficient,

$$\beta = \frac{m_{\text{sc}}}{C_D A} \ , \tag{1.1}$$

for spacecraft mass m_{sc} and drag area $C_D A$, is modulated continuously by controlling the magnetic field strength during the maneuver. The magnetoshell may also be deactivated during the maneuver by simply unpowering the magnet to return the spacecraft to a ballistic trajectory. This avoids the risk associated with a mechanical separation during hypersonic flight, a potential concern for aeroshell-jettisoning drag modulation schemes [11], and enables a larger range of β because there is no vehicle mass lost. Upon exiting the atmosphere, the magnet is released from the spacecraft and may ballistically aerobrake in the next orbit(s) until being destroyed in reentry. Meanwhile, the spacecraft performs any necessary trajectory correction maneuvering to enter its final orbit.

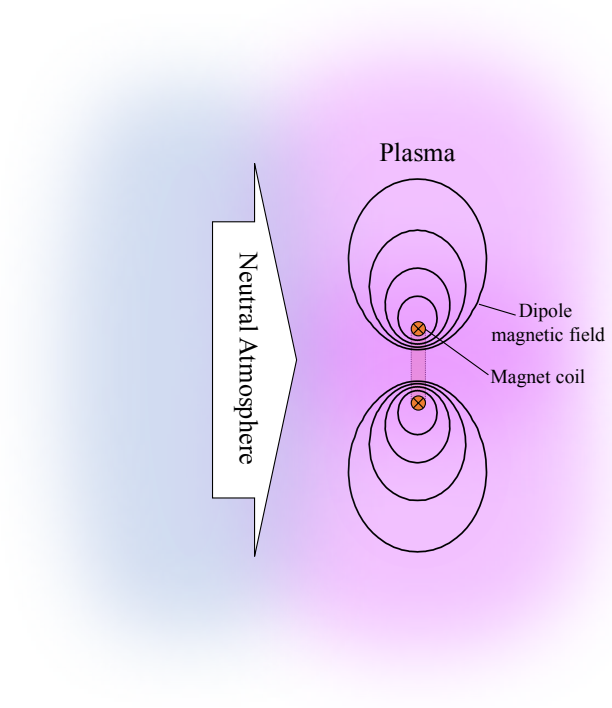

Figure 1.1: Cross section view of the magnetoshell interaction with neutral atmosphere in a spacecraft-fixed frame.

There are numerous proposed advantages to DMPA over conventional aerocapture. Traditional aeroshells generate drag with physical elements, often with deployable elements [12, 13, 14] that must stow within the launch vehicle payload fairing. In contrast, although the magnet itself must fit the same constraint, the magnetoshell's effective drag surface is made up of plasma which can extend tens of meters beyond this size. This means magnetoshells can mitigate pressure and heat loads to the spacecraft by enabling trajectories higher in the atmosphere, easing requirements on thermal protection systems (TPS) that often constrain the feasibility of aerocapture [6]. In certain configurations, the magnetized plasma may even act as a sort of thermal protection since it absorbs and utilizes the flow heat. The magnetoshell plasma is sustained by the trapping of in-situ atmospheric gas and kinetic energy, offering better performance at higher velocity. Thus, it is well suited for enabling fast trip times and ice/gas giant aerocapture.

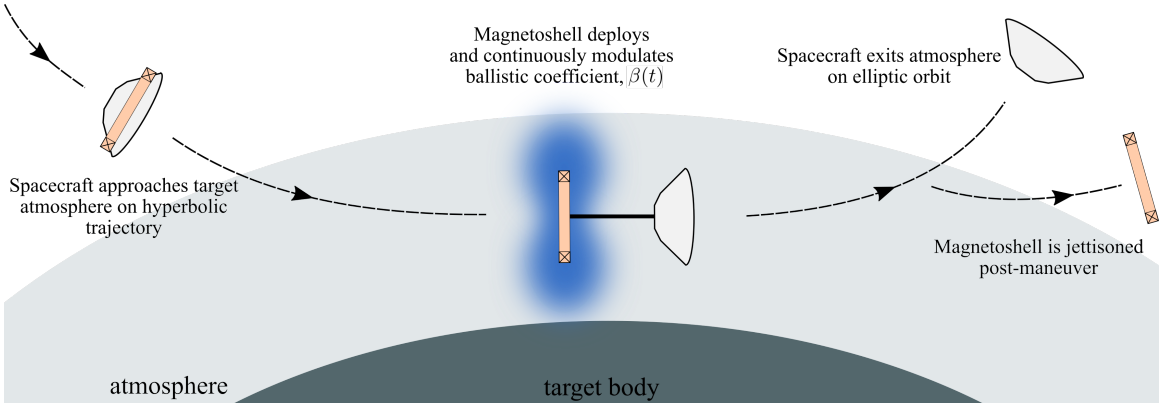

Figure 1.2: Overview of a DMPA maneuver using a trailing magnetoshell.

1.2 Background

The plasma aerocapture concept was first proposed by Slough [10] as a high-beta, rotating magnetic field dipole towed behind a spacecraft like a "plasma parachute." Kirtley [15] furthered its development by conceptualizing a simple electromagnet dipole containing a low-beta plasma, easing both energy requirements and engineering complexity. His work also derived the first analytic model of magnetoshell performance in aerocapture environments. This model was applied to prove the feasibility of using plasma aerocapture for the Human Mars DRA 5.0 cargo payloads [16] and a Neptune orbiter mission [17], in both cases indicating substantial improvements in cost and delivered mass over their proposed traditional aerocapture approaches. Hancock [18] performed an additional system analysis using Kirtley's analytic model, finding that the magnet and power system are the most significant drivers of spacecraft mass. Hancock also developed a trajectory simulation showing that a fixed-area maneuver is highly sensitive to the altitude at which the magnetoshell is activated, indicating that a higher-fidelity physical model enabling drag modulation is needed.

Kirtley also performed the first two technology demonstrations. In the first [15], a small magnetoshell generated significant drag while attached to a thrust stand with an impinging partially ionoized flow of around 1 km/s. The second demonstration [19] showed

the feasibility of using an RF plasma source injected at center-field to seed the magnetoshell plasma. Although a flight demonstration of magnetoshell drag has been proposed, Kelly [20] determined through a CubeSat system analysis that such a mission would be intractable given the mass and volume constraints of a 3U bus. SmallSat class missions (100 kg) may be a good demonstration vehicle for small scale magnetoshells, but the development and launch cost likely exceeds that of experimental demonstration on the ground and limits the physical insight that can be gained.

Although there are clear advantages to plasma aerocapture over other approaches, its physics and performance are still not well characterized. The previous physical analyses provided a basis for conceptualizing mission classes and technology implementation. However, performance prediction relied on a phenomenological model based on single-particle processes rather than the global, coupled interaction of plasma and flow. Also, drag was modeled by approximating a solid body, though more recent work has shown the plasma allows some flow to pass through it [21], highlighting the need for a higher fidelity drag model. There have been no detailed studies of DMPA missions incorporating their continuously-variable drag modulation capability. The performance sensitivity to atmospheric and navigation uncertainties is crucial for any aerocapture system yet remains uncharacterized for DMPA. The demands of drag modulation control on the magnet may have significant implications for the associated spacecraft systems and must be assessed to determine technology development needs. While the technology demonstrations illustrated the concept of drag on a magnetized plasma, the ionized, low-velocity impinging flow did not adequately represent the flow regime expected in a plasma aerocapture maneuver. Accurately ground testing this large-scale device in a rarefied, hypersonic neutral flow that simulates atmospheric entry is not possible in existing wind tunnels. Therefore, novel experimental techniques and simulation approaches must be developed to assess the feasibility of this technology.

1.3 Goals of this thesis

The work presented here aims to characterize the physics, performance, and feasibility of magnetoshells for DMPA. Specifically, it seeks to answer these questions:

1. What are the underlying physical processes governing the interaction between a magnetoshell and neutral flow?

2. How do these physics scale with spacecraft and environmental parameters like magnet size, field strength, velocity, and density?

3. What is the implication of this scaling for the use of magnetoshells in aerocapture at atmospheric celestial bodies?

4. Can the feasibility of magnetoshells be experimentally demonstrated before a flight implementation is developed?

To address these questions, we adopt a comprehensive approach with three main components. The first is an analytical model built from first principles to describe the exchange of mass and energy between a magnetoshell-like plasma and a hypersonic flow representative of the aerocapture environment. The second is a mission design framework that links the physics of magnetoshells to spacecraft scaling laws and aerocapture trajectory models. These tools are used in tandem to answer questions 1–3 above. The third aspect of the work is an experiment using a novel "plasma wind tunnel" approach to launch a hypersonic neutral flow into a magnetized plasma. Results and lessons from this experiment are used to address question 4.

1.4 Thesis structure

In Chapter 2, we derive an analytical model of the interaction between a dipole plasma and a hypersonic neutral flow. Chapter 3 uses this model to generate data across a wide range of relevant flow and plasma conditions. The data are analyzed to determine the scaling of magnetoshell performance with parameters such as magnetic field strength, flow density/velocity, injected power, and system size. Chapter 4 couples the performance scaling insight with a framework that enables preliminary designs of DMPA mission architectures. Orbit trajectory simulations that leverage magnetoshell drag physics are performed to determine the robustness of DMPA to atmospheric and entry state uncertainty. In Chapter

5, we present an experiment to demonstrate some of the physical effects that are crucial to the success of magnetoshells. Finally, Chapter 6 summarizes the work presented and offers final thoughts on the contributions of this thesis.

Chapter 2

NEUTRAL FLOW INTERACTION WITH A MAGNETIC DIPOLE PLASMA

Dipole plasmas interact with particle flows in many settings such as planetary magnetospheres [22, 23], fusion reactors [24], or magnetic sails [25]. The basic proposed architecture of a magnetoshell is a dipole plasma towed behind a spacecraft. As this device flies through the atmosphere, the flow necessarily impinges on the full spatial extent of the plasma. Therefore, a global accounting of the mass, momentum, and energy transferred from the flow is warranted to understand the processes governing this coupled interaction.

Studies of plasma-neutral flow interaction often center on the critical ionization velocity effect (CIV). Critical ionization occurs when plasma and neutrals counterstream in a magnetic field and has been investigated in theory, experiments, and numerical simulations [26, 27, 28, 29, 30]. This phenomenon, whereby background neutrals are rapidly ionized once the plasma flow reaches a threshold velocity, is ubiquitous from space to laboratory plasmas. No single comprehensive theory of critical ionization has yet been established that explains CIV observations across vastly different experimental and simulation conditions. The common mechanism among all observations is an energy feedback loop: ionization deposits the neutral kinetic energy with the ions, which transfer heat to the electrons to drive further ionization. Typically, the ion-electron energy transfer is assumed to come from collective processes [31]. Some studies, however, have shown differences in the threshold velocity and rate of ionization when collisional heating processes are allowed [32, 33], as in a high density plasma where wave heating processes may be damped [30]. Furthermore, neither theory nor experiment has addressed CIV in the context of a magnetic dipole geometry. Dipole plasmas are finite and inhomogeneous whereas most analyses of critical ionization are one-dimensional and assume the plasma is spatially infinite [27]. An investigation of the effects of finite geometry, diffusion, and collisional processes on CIV is warranted to characterize

their role in the dipole-flow interaction.

In this chapter, we present an analytical model of the flow-plasma interaction globally with a detailed accounting of mass and energy transfer processes. We begin with an analysis of single-particle behavior of the flow as it encounters the dipole. This leads to functions describing the capture of mass and energy by the plasma. We also use this to analyze the force produced on a magnetoshell as a result of flow ionization and deflection. The global model is a control volume analysis that leverages the single-particle insights to couple properties of the geometry, magnetic field, plasma, and flow to mass and energy exchange. The goal is to use this model to identify general physical scaling that will inform the feasibility and design of plasma aerocapture techologies. The work presented here is largely reproduced with permission from a pair of papers published in 2020 by Charles Kelly and Justin Little [34, 35].

2.1 Single-Particle Interaction

New ions with charge q_i and mass m_i are generated through charge exchange and electron impact ionization as the neutral flow encounters the dipole plasma. The net behavior of the plasma and neutral flow depends on the trajectories of newly created ions in the vicinity of the magnetic dipole. Understanding the impact of non-uniform magnetic fields on the resulting trajectories will inform not only momentum transfer to the magnet but also the definition of a control volume for energy and mass accounting. Here, we examine ion trajectories as a function of the location at which they are created to understand their behavior in the presence of the dipole magnetic field.

We model the magnetic field as that of a loop of current centered at the origin with radius r_c in cylindrical coordinates (r, θ, z). This is described by Jackson [36] as

$$\mathbf{B} = \frac{1}{r}\hat{\mathbf{e}}_\theta \times \nabla\psi \ , \tag{2.1}$$

$$\psi = \frac{2B_0 r_c^2 r}{\pi}\frac{(2-\kappa^2)K(\kappa^2) - 2E(\kappa^2)}{\kappa^2\sqrt{(r_c^2+r^2)+z^2}} \ , \tag{2.2}$$

$$\kappa^2 = \frac{4rr_c}{(r+r_c)^2+z^2} \ , \tag{2.3}$$

where $\hat{\mathbf{e}}_\theta$ is the azimuthal unit vector, ψ is the magnetic scalar flux function, K and E are

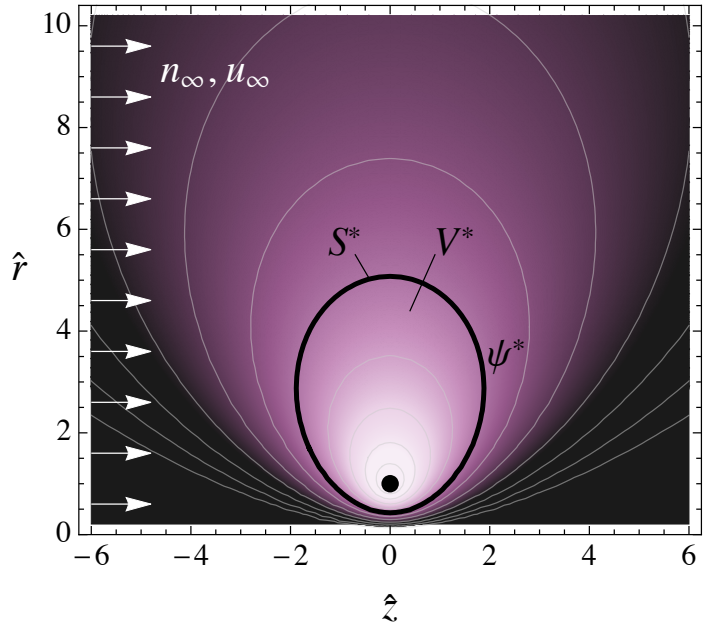

Figure 2.1: The global model is formulated in the z-r plane with symmetry about θ. Level curves of ψ [Eq. (2.2)] are shown in gray with the current loop at (0,1). The plasma density (pink) scales with ψ^α for some constant α [Eq. (2.46)]. The control volume V^* is bounded by the $\psi = \psi^*$ surface, S^*, shown in black. Axially flowing neutrals have freestream density n_∞ and velocity u_∞.

complete elliptic integrals of the first and second kind respectively, and κ is a substitute variable. B_0 is the magnetic field strength at the center of the loop. This magnetic field topology is shown in Fig. 2.1.

The equation of motion for an ion in a magnetic field without collisions can be expressed in dimensionless form as

$$\frac{d\hat{\mathbf{u}}}{d\hat{t}} = \frac{1}{\rho_L}\hat{\mathbf{u}} \times \hat{\mathbf{B}}, \tag{2.4}$$

$$\frac{d\hat{\mathbf{r}}}{d\hat{t}} = \hat{\mathbf{u}}, \tag{2.5}$$

where

$$\rho_L = \frac{m_i u_\infty}{q_i B_0 r_c}, \tag{2.6}$$

represents a characteristic ion Larmor radius normalized by the magnet radius. Here, we have introduced the dimensionless variables: velocity vector $\hat{\mathbf{u}} = \mathbf{u}/u_\infty$, position vector

$\hat{\mathbf{r}} = \mathbf{r}/r_c$, and time $\hat{t} = tu_\infty/r_c$. From Eqs. (2.4) and (2.5), the ion trajectory as a function of time, $\hat{\mathbf{r}}(\hat{t})$, is uniquely determined by ρ_L and the initial ion location and velocity, $\hat{\mathbf{r}}(0)$ and $\hat{\mathbf{u}}(0)$, respectively. Charge exchange (CX) and electron-impact ionization are the two mechanisms by which streaming neutrals become ions. In both cases, the newly formed ion will initially maintain the neutral flow velocity in the axial direction, $\hat{\mathbf{u}}(0) = \hat{\mathbf{e}}_z$, where $\hat{\mathbf{e}}_z$ is the unit vector in the axial direction. Note that while the ion is created by a collision, we consider its resulting trajectory neglecting any further collisions. This is a fair approximation in the limit of an ion Hall parameter $\Omega_i > 1$ applied only for the purpose of determining whether a given ion is trapped by the field.

We examine the influence of the non-uniform magnetic field by considering the trajectory of ions formed at various locations within the $\hat{r}$-$\hat{z}$ plane. Eqs. (2.4) and (2.5) are propagated many times longer than the transit time of an ion across the magnet ($\hat{t}_{\max} = 200$) using the LSODA differential equation solver[37]. A few sample trajectories are depicted in Fig. 2.2. We observe that ions originating upstream of the magnet are either deflected or reflected by an amount that depends largely on their initial radial location, $\hat{r}(0)$. Ions formed away from the magnet (i.e. $\hat{r}(0) > 1$) deflect by an amount that increases as $\hat{r}(0)$ decreases [Figs. 2.2(a)-(c)]. Ions formed on a collision course with the magnet (i.e. $\hat{r}(0) \sim 1$) tend to reflect because they experience stronger magnetic fields throughout their trajectory [Fig. 2.2(d)]. The behavior of ions created near the axis of the magnet ($\hat{z} \sim 0$) is distinct from those created prior to reaching the magnet. Notably, a region of space exists where ions enter into closed (or trapped) trajectories about the magnet [Figs. 2.2(e)-(f)]. A second trapped-orbit region exists at slightly larger initial radii whereby the ion trajectories exhibit orbits similar to the well-known banana orbit in tokamak plasmas [38] [Fig. 2.2(g)]. Finally, ions formed beyond this second trapped region exhibit deflected orbits [Fig. 2.2(h)].

The nature of the different ion orbits is best demonstrated using a heat map of the final axial velocity of each ion, $\hat{u}_{z,f}$, as a function of the location at which the ion was formed. Here, we consider ions formed on a uniform grid with spacing $\Delta\hat{r} = \Delta\hat{z} = 0.1$ and calculate $\hat{u}_{z,f}$ as the average of $\hat{u}_z(\hat{t})$ for $\hat{t} \in [100, 200]$. This averaging reduces the noise associated with trapped orbits for which $\hat{u}_z$ is oscillatory with time. Note that $\hat{u}_{z,f} = 1$ for undeflected ions, $\hat{u}_{z,f} = 0$ for trapped ions, and $\hat{u}_{z,f} = -1$ for fully reflected ions. The heat

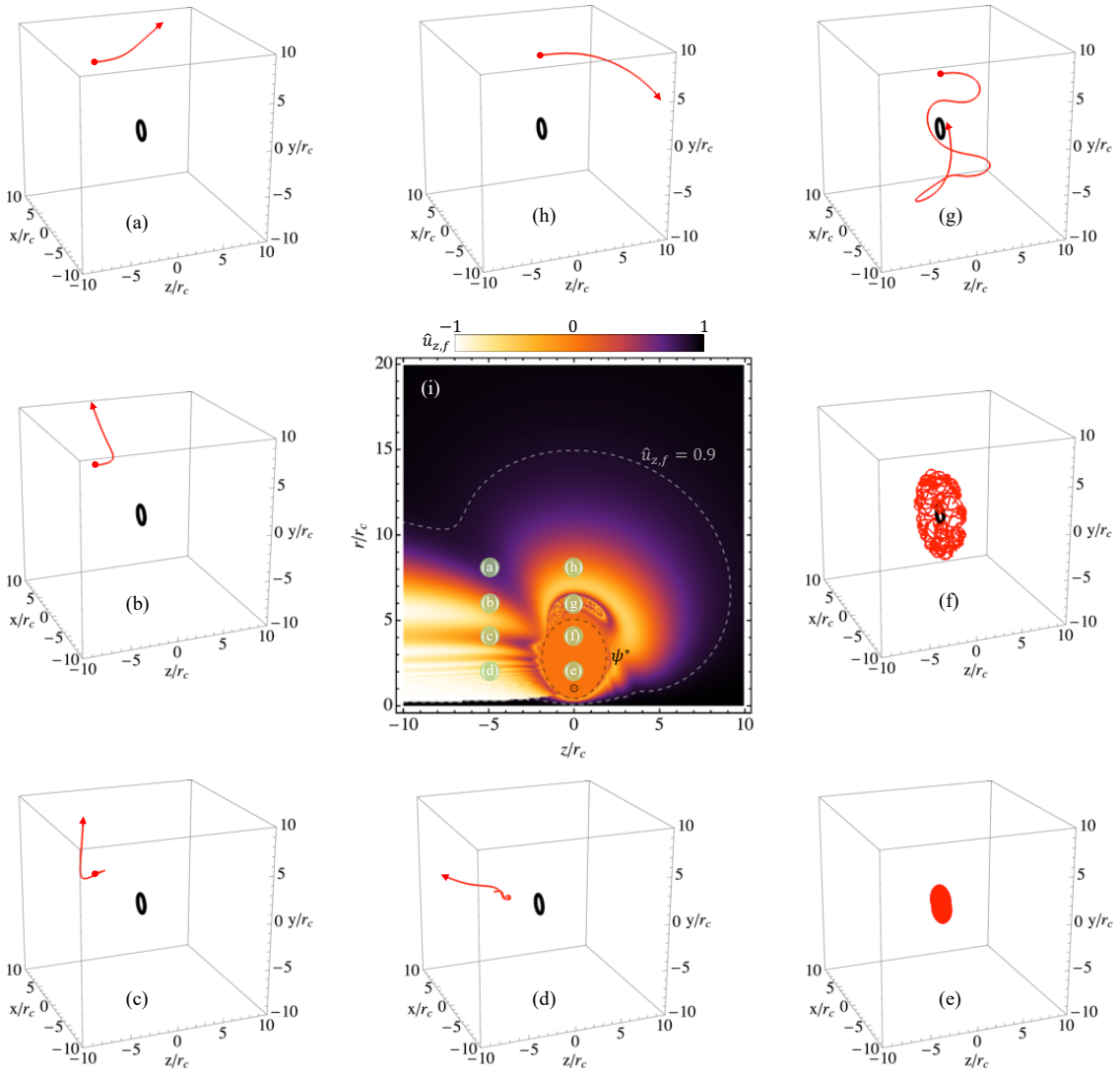

Figure 2.2: Trajectories of ions created near a dipole magnetic field with velocity $\mathbf{u} = u_\infty \hat{\mathbf{e}}_z$ and $\rho_L = 5 \times 10^{-3}$ at the following $[\hat{r}, \hat{z}]$ spatial coordinates: (a) [8,-5], (b) [6,-5], (c) [4,-5], (d) [2,-5], (e) [2,0], (f) [4,0], (g) [6,0], (h) [8,0]. Center frame (i) shows the distribution of the final velocity of deflected ions as a function of the formation location. The black dashed line denotes the trapped-ion flux surface, ψ^*.

map shown in Fig. 2.2(i) clearly shows the spatial distribution of reflected, deflected, and trapped ions. Notably, a region of pass-through orbits exists on-axis because ions formed here do not encounter significant radial magnetic fields. We will ultimately use maps of $\hat{u}_{z,f}$

to calculate the force of the reacting neutral flow on the magnet by taking the summation of the axial momentum change per ion multiplied by the rate at which ions are formed.

Ions with trapped orbits are particularly important because they generally reside near the magnet for timescales long compared to the collisional timescale, allowing them to reach thermal equilibrium with the plasma. As a consequence, trapped ions are a source of plasma mass and energy. Using distributions of $\hat{u}_{z,f}$ for different ρ_L, we observe a characteristic boundary inside which all ions are trapped. This boundary is defined by a specific magnetic flux surface,

$$\hat{\psi}^* = \sqrt{2\rho_L}. \tag{2.7}$$

The resulting magnetic flux contour, depicted in Figure 2.2(i), marks the transition between trapped ions and reflected/deflected ions. In other words, any ion formed from the flow in a location at which $\hat{\psi} > \hat{\psi}^*$ will become trapped by the magnetic field. In 3D space, the $\hat{\psi}^*$ contour forms a toroidal control volume that we will use to examine mass and energy transfer between the neutral flow and plasma. We conservatively neglect the trapped-ion volume formed by the banana orbit region [Fig. 2.2(g)] due to the complexity associated with modeling this irregular shape. This region may be addressed by future higher-order modeling.

2.2 Mass and Energy Capture by the Dipole Plasma

The results of the single particle model provide us with a crucial link between the high-speed neutral gas flow and confined plasma. As neutral particles interact with plasma ions and electrons, new ions can be formed through ionization or charge exchange collisions. Ions formed within the boundary defined by Eq. (2.7) provide a source of mass and energy to the plasma. Here, we use continuity to derive an equation for the neutral particle density spatial distribution as a function of key dimensionless parameters. The neutral density distribution is then used along with our expression for the trapped-particle boundary to determine the rate of mass and energy transfer from the neutral flow to the plasma.

We assume the ion and electron densities are equal everywhere ($n_i = n_e$) to preserve charge neutrality. In the presence of charge exchange reactions and electron impact ioniza-

tion, the steady-state continuity equation then takes the following form

$$\nabla \cdot (n_{sn}\mathbf{u}_{sn}) = -R_{\text{tot}} n_{sn} n_e. \tag{2.8}$$

Here, $R_{\text{tot}} = R_{\text{ion}} + R_{\text{cx}}$ is the sum of the ionization (R_{ion}) and charge exchange (R_{cx}) reaction rates. Note that we have introduced the subscript "*sn*" to distinguish between incident neutral particles (*viz.* stream neutrals) and neutral particles that are formed via charge exchange reactions (*viz.* secondary neutrals). Because the cross-section for collisions between stream neutrals and secondary neutrals is much smaller than ionization and charge exchange cross-sections for the stream energies of interest (> 1 eV), the secondary neutrals do not play a significant role in mass and energy transfer from the neutral flow to the plasma. However, as we will discover in Chapter 3, secondary neutrals play a key role in the global balance of mass and energy within the plasma.

Two simplifying assumptions enable us to reduce Eq. (2.8) into a form amenable to analytical modeling. First, we assume that $\mathbf{u}_{sn} = u_\infty \hat{\mathbf{e}}_z$ everywhere, which is equivalent to saying that the stream neutral flow is directed along $\hat{\mathbf{e}}_z$ with a Mach number $M_{sn} \gg 1$. Second, following Kesner *et al.* [39] we assume the dipole is driven to a stationary state and any fluctuations are damped out on timescales faster than the characteristic evolution time of the system. This second assumption allows us to approximate the electron density as $n_e/n_{e,r} = (\hat{\psi}/\hat{\psi}_r)^\alpha$. Here, $n_{e,r}$ is the electron density along an arbitrary reference surface of constant scalar flux $\hat{\psi}_r$. The parameter α is a constant that represents the steepness of the density profile. In our subsequent analysis we take $\alpha = 4$ to be consistent with theoretical predictions for plasma confined by a strong magnetic dipole [39, 40]. Note the density profile considered here neglects the effects of anisotropy and the interaction between the plasma and magnet surfaces [41, 40]. Diffusion across the $\hat{\psi}^*$ surface is expected to far exceed any possible cross-field loss to the magnet. Despite their limitations, these simplifications enable us to examine the general scaling of mass and energy transfer over a wide parameter space.

With the above simplifications, the solution to Eq. (2.8) is

$$\hat{n}_{sn} = \exp\left(-\zeta_{\text{tot}} I_n\right), \tag{2.9}$$

where $\hat{n}_{sn} = n_{sn}/n_\infty$ and

$$I_n = \int_{-\infty}^{\hat{z}} \left(\frac{\hat{\psi}}{\hat{\psi}_r} \right)^\alpha d\hat{z}. \tag{2.10}$$

Here, I_n is a function of $\hat{r}$ and $\hat{z}$ that depends only on the specific magnetic field topology. According to Eq. (2.9), the stream neutral density distribution forms a wake whose size depends on the dimensionless scalar quantity

$$\zeta_{\text{tot}} \equiv \frac{R_{\text{tot}} n_{e,r}}{u_\infty / r_c}. \tag{2.11}$$

We note that ζ_{tot} scales with the ratio of the characteristic ion formation rate and the characteristic rate at which stream neutrals transit the magnet.

The stream neutral density distribution is shown for four different values of ζ_{tot} in Fig. 2.3. It is clear that the wake formed by the interaction of the neutral flow with the dipole plasma increases in size as ζ_{tot} increases. This result is due to an increased probability that a stream ion undergoes an ionization or charge exchange reaction with the plasma prior to transiting past the magnet. Also shown in Fig. 2.3 are magnetic flux contours that define the trapped-ion volume for three different values of ρ_L, as determined from Eq. (2.7). Notably, for each ρ_L there exists a value of ζ_{tot} above which the trapped-ion volume is shadowed by the wake (i.e. $\hat{n}_{sn} \approx 0$ for $\psi > \psi^*$). This shadowing effect will ultimately play an important role in the transfer of stream neutral flow mass and energy to the plasma.

The total capture rate of stream neutral particles within the trapped-ion control volume ($\dot{N}_{\text{cap}}$) can be determined by integrating the volumetric stream neutral reaction rate over the volume $\psi > \psi^*$. This can be written symbolically as

$$\dot{N}_{\text{cap}} = \oint_{\psi > \psi^*} R_{\text{tot}} n_{sn} n_e dV. \tag{2.12}$$

Recognizing that each stream neutral brings with it $m_{sn} u_\infty^2/2$ worth of kinetic energy, the capture rate of stream neutral energy, or captured power (P_{cap}), is given by

$$P_{\text{cap}} = \frac{1}{2} m_{sn} u_\infty^2 \dot{N}_{\text{cap}}. \tag{2.13}$$

It is important to note that the mass captured by the plasma is divided among the ion and secondary neutral populations by an amount that depends on the ratio of $R_{\text{ion}}/R_{\text{cx}}$. This division will be elucidated by a global plasma model detailed in Section 2.4.

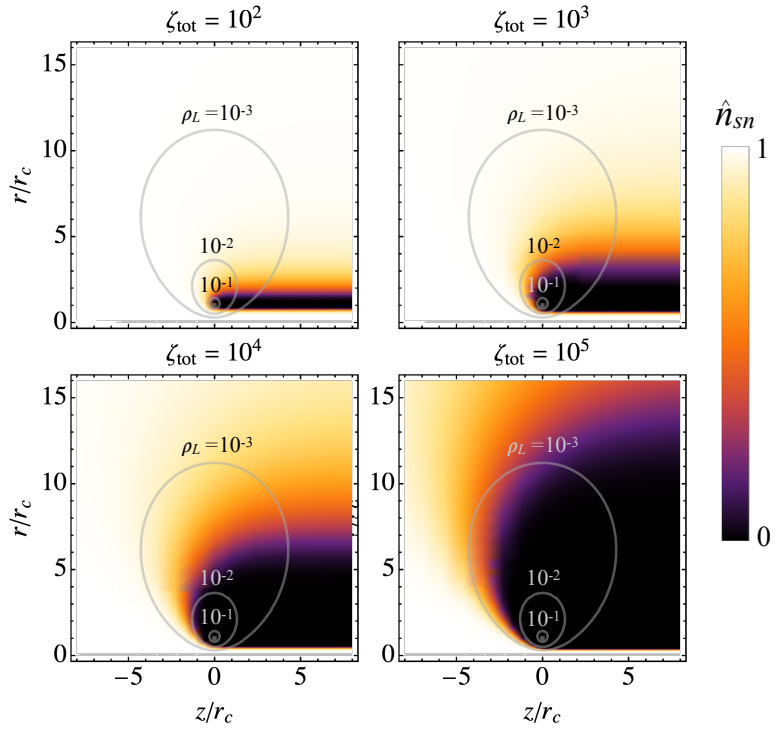

Figure 2.3: Stream neutral density distribution for four values of $\zeta_{\rm tot}$. Ion-trapping magnetic flux surfaces are shown in each plot for three values of ρ_L. Here, $\alpha = 4$ and $\hat{\psi}_r = 1$.

The equations for particle and energy capture can be simplified considerably by introducing the following normalization: $\hat{\dot{N}} \equiv \dot{N}/(n_\infty u_\infty r_c^2)$ and $\hat{P} \equiv 2P/(m_{sn} n_\infty u_\infty^3 r_c^2)$. Here, $\dot{N}$ and P are normalized by the flux of neutral particles and kinetic energy on an area equal to r_c^2, respectively. The dimensionless form of Eqs. (2.12) and (2.13) then becomes

$$\hat{\dot{N}}_{\rm cap} = \hat{P}_{\rm cap} = \zeta_{\rm tot} I_{sn}(\rho_L, \zeta_{\rm tot}), \tag{2.14}$$

where

$$I_{sn}(\rho_L, \zeta_{\rm tot}) = \oint\limits_{\psi > \psi^*} \hat{n}_{sn} \left(\frac{\hat{\psi}}{\hat{\psi}_r} \right)^\alpha d\hat{V}. \tag{2.15}$$

For a given magnetic field topology, the integral I_{sn} is a function of only two dimensionless parameters: the bounds of the integral are governed by ρ_L via Eq. (2.7) and the spatial distribution of $\hat{n}_{sn}$ is governed by $\zeta_{\rm tot}$ via Eq. (2.9). This result suggests that variations

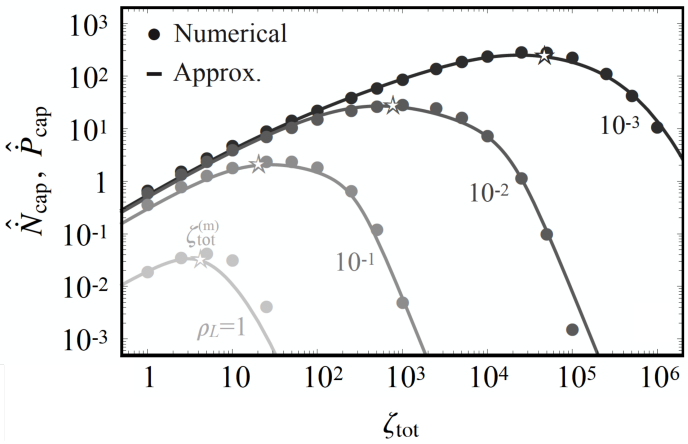

Figure 2.4: Exact numerical solution (circles) and approximation (lines) to the normalized particle capture rate, $\hat{\dot{N}}_{\rm cap}$. Solutions are shown for values of ρ_L across four orders of magnitude. Approximations for $\hat{\dot{N}}_{\rm cap}$ are obtained from Eq. (2.16). Stars denote the location of $\zeta_{\rm tot}^{(m)}$. Here, $\alpha = 4$ and $\hat{\psi}_r = 1$.

in the mass and energy capture rates with the properties of the neutral flow (e.g. density, particle mass, velocity) or magnetized plasma (e.g. magnet strength, size, plasma density, temperature) are similar with respect to ρ_L and $\zeta_{\rm tot}$.

The dimensionless particle (and power) capture rate is shown as a function of ρ_L and $\zeta_{\rm tot}$ in Fig. 2.4. For fixed ρ_L, $\hat{\dot{N}}_{\rm cap}$ increases linearly with $\zeta_{\rm tot}$ at small values of $\zeta_{\rm tot}$. This linear regime results from a weak $\zeta_{\rm tot}$-dependence within the integral I_{sn}, which occurs when $\hat{n}_{sn} \approx 1$ for $\hat{\psi} > \hat{\psi}^*$. Physically speaking, the stream neutral wake does not shadow the ion-trapping volume at low $\zeta_{\rm tot}$ (un-shadowed ψ^*). As $\zeta_{\rm tot}$ increases a maximum capture rate eventually occurs. Just beyond this maximum value, further increases in $\zeta_{\rm tot}$ yield slight reductions in $\hat{\dot{N}}_{\rm cap}$ (partially-shadowed ψ^*). Eventually a regime is reached wherein $\hat{\dot{N}}_{\rm cap}$ decreases rapidly with increasing $\zeta_{\rm tot}$ (fully-shadowed ψ^*).

The solid lines in Fig. 2.4 represent a simple analytical approximation for $\hat{\dot{N}}_{\rm cap}$ For

$\rho_L \lesssim 1$ and $\zeta_{\rm tot} > 0.1$, the particle capture integral is well-approximate by the function

$$I_{sn}(\rho_L, \zeta_{\rm tot}) \approx \frac{s_0(\rho_L)}{1 + (\zeta_{\rm tot}/s_1)^{1/2} + [\zeta_{\rm tot}/s_2(\rho_L)]^{3/2} + [\zeta_{\rm tot}/s_3(\rho_L)]^3 + [\zeta_{\rm tot}/s_4(\rho_L)]^5}, \quad (2.16)$$

where

$$s_0(\rho_L) = 0.66\exp(-3.27\rho_L^{0.73}), \quad (2.17)$$

$$s_1 = 26.81, \quad (2.18)$$

$$s_2(\rho_L) = 0.62\rho_L^{-1.2} + 4.29, \quad (2.19)$$

$$s_3(\rho_L) = 4.02\rho_L^{-1.3} \quad (2.20)$$

$$s_4(\rho_L) = 2.68\rho_L^{-1.6} + 5.36. \quad (2.21)$$

Eqs. (2.16)–(2.21) are important because they enable the mass and energy capture rates to be quickly calculated without needing to solve the full integral in Eq. (2.15). The value of $\zeta_{\rm tot}$ that corresponds to the maximum capture rate can be estimated from this approximate form of $\hat{\dot{N}}_{\rm cap} = I_{sn}\zeta_{\rm tot}$, which to first order is $\zeta_{\rm tot}^{(m)} \approx 0.3/\rho_L^{0.6}$ for $\rho_L \ll 1$. Values of $\zeta_{\rm tot}^{(m)}$ are shown in Fig. 2.4 which indicates that full shadowing of ψ^* occurs for $\zeta_{\rm tot} > 10\zeta_{\rm tot}^{(m)}$. Beyond this limit the vast majority of neutral flow particles ionize and deflect prior to reaching the ion-trapping volume.

2.3 Momentum Transfer to the Dipole Magnet

A force is produced on the dipole magnet when ionized stream neutral particles either deflect or are captured by the magnetic field. In this case, momentum is transferred to the magnet via the interaction between the magnet current and the current density that results from summing over individual ion orbits. For plasma aerocapture, this force represents the drag generated when the magnetized plasma encounters a planetary atmosphere at high velocities – a quantity critical to assessing the feasibility of this technology. Here, we use the particle trajectory maps (Fig. 2.2) and stream neutral density distribution (Fig. 2.3) to derive a scaling law for the drag force generated by a high-speed neutral flow interacting with a dipole plasma.

We define the drag force, F_D, as the axial force imparted by the neutral flow to the magnet. The force density can be written as product of the the volumetric reaction rate of stream neutrals ($R_{\text{tot}} n_{sn} n_e$) and the change in momentum of the newly formed ion ($m_{sn}\Delta u_z$), where $\Delta u_z = u_{z,f} - u_\infty$ is a function of r and z that represents the total change in axial velocity of an ion formed at location (r, z). The volume integral of the force density over all space yields the drag force

$$F_D = \int_\infty R_{\text{tot}} n_{sn} n_e m_{sn} \Delta u_z dV. \tag{2.22}$$

We define the normalized drag force as

$$\hat{F}_D \equiv \frac{2F_D}{m_{sn} n_\infty u_\infty^2 \pi r_c^2}. \tag{2.23}$$

Here, $\hat{F}_D$ effectively represents the drag of the system relative to the drag on a solid disk of radius r_c, and can be thought of as a characteristic drag coefficient that includes the effects of magnetic deflection. With this definition Eq. (2.22) can be written as

$$\hat{F}_D(\rho_L, \zeta_{\text{tot}}) = \zeta_{\text{tot}} I_D(\rho_L, \zeta_{\text{tot}}), \tag{2.24}$$

where

$$I_D(\rho_L, \zeta_{\text{tot}}) = 4 \int_{-\infty}^{\infty} \int_0^{\infty} \hat{n}_{sn} \Delta \hat{u}_z \left(\frac{\hat{\psi}}{\hat{\psi}_r} \right)^\alpha \hat{r} d\hat{r} d\hat{z}. \tag{2.25}$$

We thus arrive at a second integral function that depends on only two dimensionless parameters for a given field topology: $\hat{n}_{sn}$ is governed by ζ_{tot} via Eq. (2.9) and $\Delta \hat{u}_z$ depends on ρ_L as shown in Fig. 2.2.

The force density distribution is shown in Fig. 2.5 for a wide range of ρ_L and ζ_{tot}. Here, the force density is defined as

$$\hat{f}_D = (2/\pi) \zeta_{\text{tot}} \hat{n}_{sn} \Delta \hat{u}_z (\hat{\psi}/\hat{\psi}_r)^\alpha \tag{2.26}$$

such that $\int_\infty \hat{f}_D \, dV = \hat{F}_D$. Values of $\hat{f}_D$ are calculated on an adaptive grid that focuses gridpoints in regions of high reactivity. This technique helps to increase both the resolution of the resulting spatial distribution and numerical precision of the integrated drag force. The general features of the force density distribution can be traced back to the three variables upon which it relies: the dark region near and behind the magnet results from wake

formation in the function $\hat{n}_{sn}$; the streaks in front of the magnet, dark band on the magnet axis, and lobes on the magnet periphery are all features associated with the ion orbit mapping (Fig. 2.2) contained in the function $\Delta\hat{u}_z$; and the region over which the previous two effects are important is localized near a particular flux surface via the plasma density distribution, $\hat{n}_e \propto \hat{\psi}^\alpha$. We observe that the radial extent of $\hat{f}_D$ generally increases with decreasing ρ_L. For a given ρ_L, the radial extent of $\hat{f}_D$ increases with ζ_{tot} before eventually reaching a saturation point at which it ceases to expand. Finally, we note that the value of ζ_{tot} corresponding to the saturation point increases as ρ_L decreases.

Numerical calculations for $\hat{F}_D$ are shown as a function of ζ_{tot} and ρ_L in Fig. 2.6. The solid lines in Fig. 2.6 represent a simple analytical approximation to $\hat{F}_D$ which, for $\rho_L \lesssim 1$ and $\zeta_{\text{tot}} > 0.1$, is given by

$$\hat{F}_D(\rho_L, \zeta_{\text{tot}}) \approx d_1(\rho_L)\left[\frac{\zeta_{\text{tot}}^{0.7}}{d_2(\rho_L) + d_3(\rho_L)/\zeta_{\text{tot}} + \zeta_{\text{tot}}^{0.7}}\right], \tag{2.27}$$

where

$$d_1(\rho_L) = \frac{1.2}{\rho_L + \rho_L^3}, \tag{2.28}$$

$$d_2(\rho_L) = 2.51\rho_L^{-0.97} + 0.12, \tag{2.29}$$

$$d_3(\rho_L) = 1.35\rho_L^{-1}. \tag{2.30}$$

As the $\hat{f}_D$-distributions in Fig. 2.5 suggest, $\hat{F}_D$ generally increases as ρ_L decreases. Furthermore, $\hat{F}_D$ increases with ζ_{tot} for fixed ρ_L up to a saturation point, with saturation occurring at higher values of ζ_{tot} as ρ_L decreases. Even with the saturation effect, drag forces up to three orders of magnitude greater than the purely aerodynamic drag are observed. The scaling of the saturated drag value is revealed by taking the limit $\zeta_{\text{tot}} \to \infty$ of the approximate form of $\hat{F}_D$ [Eq. (2.27)], yielding $\hat{F}_D^{(s)} \approx 1.2/\rho_L$ to first order. Interestingly, this is roughly 70% of the drag that would be generated if the neutral flow were to be replaced by a fully ionized flow with equivalent velocity and density. We find that the reactivity at which saturation occurs is roughly 1-5 times higher than $\zeta_{\text{tot}}^{(m)}$. Therefore, it is possible to approach drag saturation while maintaining significant mass and energy transfer to the plasma. This point has important consequences for plasma aerocapture applications because it suggests the possibility of optimizing in-situ flow utilization without sacrificing drag performance.

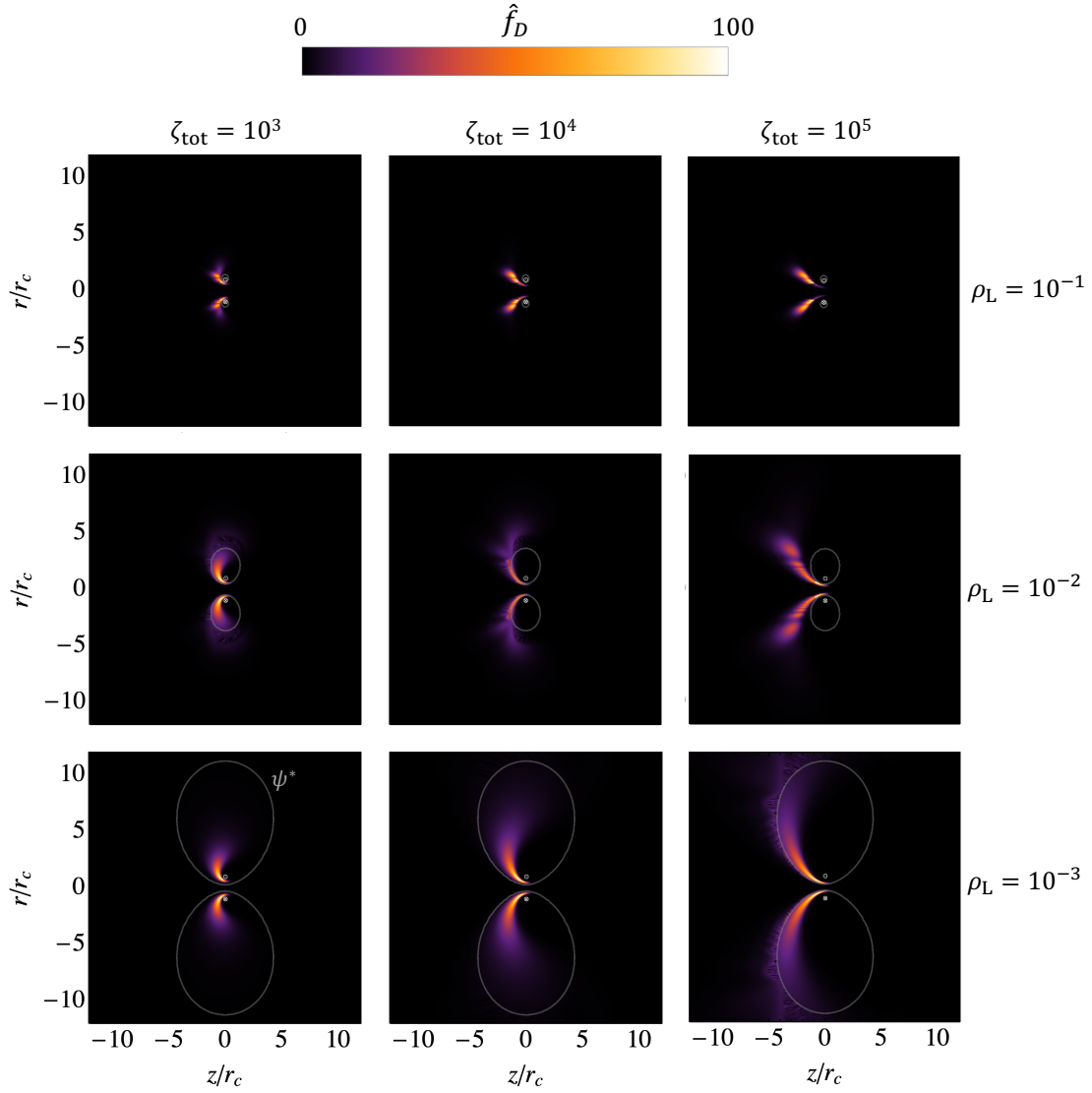

Figure 2.5: Distribution of the drag force density, $\hat{f}_D$, for different values of ζ_{tot} and ρ_L. Gray lines denote the trapped-ion flux surface, $\hat{\psi}^*$. Here, $\alpha = 4$ and $\hat{\psi}_r = 1$.

2.4 Global Plasma Model

The model consists of conservation equations that describe the exchange of mass and energy among the plasma and flow. The equations are normalized, averaged over a control volume, and solved numerically for the time evolution of total populations and energies. The volume-

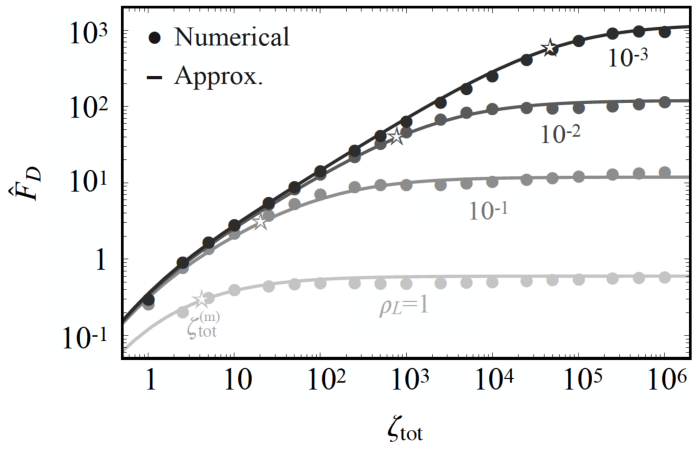

Figure 2.6: Exact numerical solution (circles) and approximation (lines) to the normalized drag, $\hat{F}_D$ [Eqs. (2.22)–(2.24)]. Solutions are shown for values of ρ_L across four orders of magnitude. Approximations for $\hat{F}_D$ are obtained from Eq. (2.27). Stars denote the location of $\zeta_{\text{tot}}^{(m)}$. Here, $\alpha = 4$ and $\hat{\psi}_r = 1$.

averaging approach eases computational load and therefore enables a broad parameter study from which we can identify physical scaling. Fig. 2.1 provides an overview and reference for the problem formulation that is applied throughout this chapter. Additional detail on the implementation of the plasma model is found in Appendix A.

2.4.1 Three-Fluid Model

For a control volume analysis, we start from basic conservation equations which allow us to account for all possible internal sources/sinks as well as flows across the boundary surface. Ions (subscript i), electrons (e), and neutrals are treated as separate species. We distinguish between stream neutrals (sn), which are yet-untouched flow particles, and secondary neutrals ($2n$), i.e. those generated in i-sn charge exchange reactions. Conservation of mass and energy for each population j is described by

$$\frac{\partial n_j}{\partial t} + \nabla \cdot (n_j \mathbf{u}_j) = \sum_s \dot{n}_j^s \,, \tag{2.31}$$

$$\frac{\partial \varepsilon_j}{\partial t} + \nabla \cdot (\varepsilon_j \mathbf{u}_j) = \sum_s \dot{\varepsilon}_j^s \,, \tag{2.32}$$

where n_j is the number density, ε_j is the energy density, $\mathbf{u}_j$ is the bulk fluid velocity, and $\partial/\partial t$ is the partial derivative with respect to time t. The right hand sides of Eqs. (2.31) and (2.32) represent summation over all contributing sources and losses, where $\dot{x}_j^s$ is a rate of change of variable x in species j due to process s. The energy density is defined following Meier and Shumlak [42] as

$$\varepsilon_j = \frac{1}{2} m_j n_j u_j^2 + p_j/(\gamma - 1) \ , \tag{2.33}$$

where m_j is the particle mass, p_j is the species pressure, and γ is the ratio of specific heats. With these general equations established, the problem is now constrained to enable formulation of an analytic model.

Model Constraints

In order to facilitate a global approach over a detailed computational model, we reduce the problem complexity with a series of assumptions. Although these provide a simplistic approach, they enable us to attain broad physical insight from modeling before adding complexity in later analyses. They are as follows:

1. The system of equations is reduced by (1) considering only a single atomic constituent for the stream, ions, and secondary neutrals; (2) recognizing that energy conservation of stream neutrals is irrelevant since ε_{sn} is, by definition, fixed; and (3) assuming quasineutrality and singly-charged ions ($n_i = n_e$). The latter argument equating ion and electron continuity implies that plasma diffusion is ambipolar.

2. We assume a dense ($n_e > 10^{16}$ m^{-3}), collisional plasma with electron Hall parameter $\Omega_e \gg 1$. Electrons are thus magnetized and diffuse across field lines due to heavy particle collisions. By assuming diffusion is much slower than collisional timescales, energy distributions are Maxwellian and species act as ideal gases with isotropic temperature ($p_j = n_j T_j$).

3. We take the magnetic pressure to dominate that of the plasma (i.e. low beta) and the stream dynamic pressure. For low-temperature plasma ($T < 100$ eV), this implies a

lower bound on applied field strength for a given plasma density, generally ranging from 10–100 mT in this model. This assumption allows us to neglect magnetic fields induced by either plasma motion or diamagnetic currents [43].

4. By neglecting parallel currents [41, 39] and toroidal drifts, we may assume the perpendicular diffusion is the only bulk fluid motion besides the freestream flow. The freestream is taken to be in free molecular flow and hypersonic so that its energy density is essentially kinetic.

A discussion of the validity and consequences of these assumptions is found in Section 3.6 at the end of the chapter. We now develop the model equations with specified mass and energy transfer processes according to the applied constraints.

Sources and Losses

For this collisional, partially ionized plasma, the primary sources and sinks for mass and energy are ionization, charge exchange, Coulomb interaction, and plasma injection. Fig. 2.7 serves as a visual guide to these mass and energy transfer processes among the model species. The treatment of each is detailed here and is largely founded on the plasma-neutral fluid model developed by Meier and Shumlak [42].

Ionization (iz) Both stream neutrals and secondary neutrals can be ionized by electron impact. In general, ionization of neutral species j (superscript iz, j) occurs at a rate

$$\dot{n}_i^{\mathrm{iz},j} = n_j n_e R_{\mathrm{iz}} \ , \tag{2.34}$$

denoting the rate coefficient of a reaction s as R_s. Neutral energy is absorbed by the ion population while electrons incur a loss of ϵ_{ion}, which is the effective ionization cost including losses due to scattering and excitation:

$$\dot{\varepsilon}_i^{\mathrm{iz},j} = \frac{3}{2} T_j \dot{n}_i^{\mathrm{iz},j} \ , \tag{2.35}$$

$$\dot{\varepsilon}_e^{\mathrm{iz},j} = \dot{n}_i^{\mathrm{iz},j} \left(\frac{3}{2} M_{e/j} T_j - \epsilon_{\mathrm{ion}} \right) \ , \tag{2.36}$$

where $M_{k/j} \equiv m_k/m_j$ is the mass ratio of species k and j.

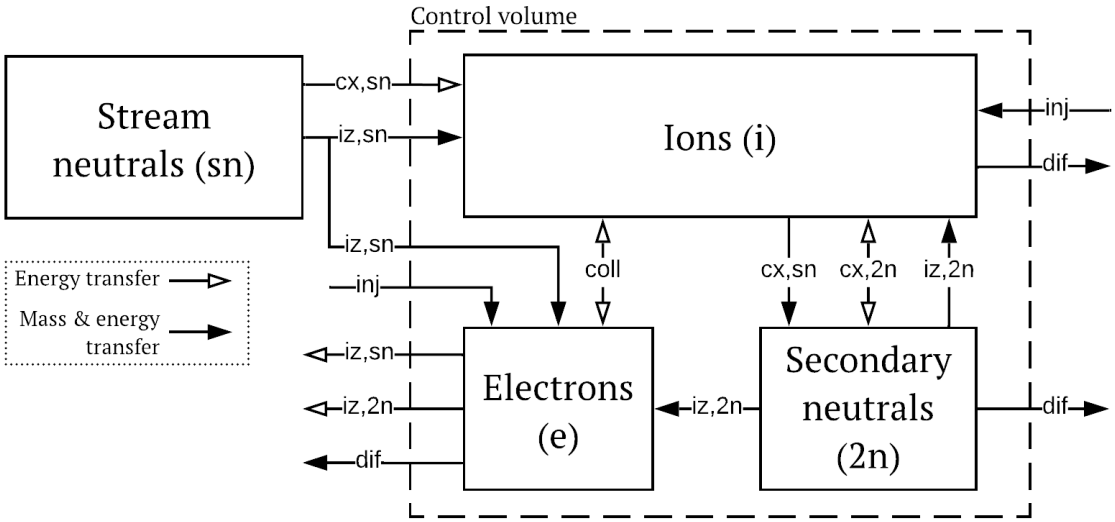

Figure 2.7: Diagrammatic representation of the global model. Ionization of neutral species j (iz,j), charge exchange with neutral species j (cx,j), Coulomb collisions (coll), artificial plasma injection (inj), and diffusion (dif) are the processes contributing to mass and energy transfer between the populations sn, i, e, and $2n$. Some of these processes involve both mass and energy transport (shaded arrows) while others only transfer energy (unshaded arrows).

Charge Exchange (cx) Ions undergo charge exchange (CX) with both neutral species, but only CX with the stream produces a net mass change by creating secondary neutrals from the ion population,

$$\dot{n}_{2n}^{\mathrm{cx},sn} = n_i n_{sn} R_{\mathrm{cx}} \ . \tag{2.37}$$

In general, each particle will maintain the energy it had before the reaction:

$$\dot{\varepsilon}_i^{\mathrm{cx}} = Q_{i,2n}^{\mathrm{cx},2n} - Q_{2n,i}^{\mathrm{cx}} + \frac{1}{2} m_i u_\infty^2 \dot{n}_{2n}^{\mathrm{cx},sn} \ , \tag{2.38}$$

$$\dot{\varepsilon}_{2n}^{\mathrm{cx}} = -Q_{i,2n}^{\mathrm{cx},2n} + Q_{2n,i}^{\mathrm{cx}} \ . \tag{2.39}$$

Here, $Q_{j,k}^s$ is a heat transfer from species k to j associated with reaction s [Eq. (A.12)]. The first two terms in each of Eqs. (2.38) and (2.39) represent the exchange of thermal energy between ions and secondary neutrals during CX reactions. The third term in Eq. (2.38) representing power absorbed by the ions during stream CX is therefore an energy source for the system.

Collisions (coll) Energy transfer in Coulomb collisions between ions and electrons is described by Braginskii [44] who expresses the transfer rate as

$$\dot{\varepsilon}_i^{\rm coll} = -\dot{\varepsilon}_e^{\rm coll} = \frac{n_e}{\tau_{ie}}(T_e - T_i) \ , \tag{2.40}$$

where τ_{ie} is the ion-electron collision time [Eq. (A.1)]. Note that this is the only energy channel between ions and electrons; we explicitly neglect collective processes, which are usually invoked to heat electrons in CIV models. Still, the model can be adapted to consider turbulent heating in later work by simply changing this thermalization term.

Injection (inj) Lastly, we account for the possibility of an artificial plasma source inside the control volume. In practice, this may represent a mechanism to seed ionization in the magnetoshell or modulate the plasma-flow interaction. It is modeled as a source of total particles N and total energy E that are distributed about the populations rapidly with respect to the timescales of interest. Ions and electrons are injected with a mass flow rate $\Gamma^{\rm inj}$ at fixed temperatures $T_{i,{\rm inj}}$ and $T_{e,{\rm inj}}$, respectively, such that the particle and energy rates are

$$\dot{N}_i^{\rm inj} \approx \frac{\Gamma^{\rm inj}}{m_i} \ , \tag{2.41}$$

$$\dot{E}_j^{\rm inj} = \frac{5}{2} T_{j,{\rm inj}} \dot{N}_i^{\rm inj} \ , \tag{2.42}$$

where j represents ions or electrons and perfect gas enthalpy, $5nT/2$, is assumed [45].

Diffusion

The flux divergence terms in Eqs. (2.31) and (2.32) account for any fluid motion across the control volume boundary. Recall that we assume diffusion is ambipolar, perpendicular to the field, and governed by electrons. Recall also that diffusion is the only bulk fluid motion and therefore the only boundary flux. The energy lost is thermal only, i.e. $\varepsilon_j \approx p_j/(\gamma - 1)$. Considering only perpendicular diffusion, we have [45]

$$n_j \mathbf{u}_j = -D_j \nabla_\perp n_j \ , \tag{2.43}$$

$$\varepsilon_j \mathbf{u}_j = -\frac{T_j}{\gamma - 1} D_j \nabla_\perp n_j \ , \tag{2.44}$$

where $\nabla_\perp$ is the field line-normal gradient operator and T_j is the species temperature in energy units. Note that energy flux is scalar with particle flux due to the ideal gas assumption, $p_j = n_j T_j$.

In order to derive diffusion terms for the three populations, we must determine the proper coefficient D_j for each. With electrons governing the ambipolar plasma diffusion rate, it is appropriate to consider anomalous Bohm effects and electron collisions with both ions and secondary neutrals. Therefore, the effective diffusion coefficient for electrons (and, by symmetry, ions) is $D_e = D_i = D_B + D_c$. The Bohm diffusion coefficient, D_B, and collisional coefficient, D_c, are given by Lieberman [45] and Goldston [46] respectively. Detailed descriptions are provided in Eqs. (A.3)–(A.8). Secondary neutral diffusion arises from momentum transfer collisions with ions and gas-kinetic collisions with other neutrals. We use a general form for gas diffusion given by Lieberman [45] and adapt it for these two collision types to obtain the secondary neutral diffusion coefficient, D_{2n}, which is detailed in Eqs. (A.19)–(A.20).

Normalization

The three-fluid model will be simulated for a wide range of flow and plasma conditions. Therefore, we normalize the model so that self-similar physical scaling laws are readily identified. Because they are fixed inputs, freestream parameters (subscript ∞) are primarily used for normalization. The following scheme is employed:

$$\begin{gathered}(\hat{z}, \hat{r}) = (z, r)/r_c \qquad \hat{t} = t u_\infty / r_c \qquad \hat{n}_j = n_j / n_\infty \\ \hat{\mathbf{u}}_j = \mathbf{u}_j / u_\infty \qquad \hat{\varepsilon}_j = \varepsilon_j / \varepsilon_\infty \qquad \hat{T}_j = T_j / T_\infty \\ \hat{\mathbf{B}} = \mathbf{B}/B_0 \qquad \hat{\psi} = \psi/(B_0 r_c^2)\end{gathered} \tag{2.45}$$

The stream is hypersonic with freestream velocity $u_\infty \hat{\mathbf{e}}_z$ and freestream density n_∞ (see Fig. 2.1). Thus, the freestream energy density is primarily kinetic, i.e. $\varepsilon_\infty \approx m_{sn} n_\infty u_\infty^2/2$. We define an effective temperature of the incoming flow, T_∞, such that $\varepsilon_\infty = (3/2) n_\infty T_\infty$. The normalization scheme in (2.45) yields a number of dimensionless parameters that govern the system physics, as we will see in the next two sections.

2.4.2 Control Volume Averaging

To describe the global system, the normalized equations are integrated over the control volume (CV). The CV representing the dipole plasma describes the spatial extent to which newly formed ions are trapped by the magnetic field. As described in Section 2.1, we defined the CV the region enclosed by the ψ^* contour [Eq. (2.7)]. Fig. 2.1 shows the azimuthal cross-section of the CV boundary surface, S^*, which encloses the volume of the toroid, V^*. Eqs. (2.7) and (2.6) demonstrate simple scaling between model parameters and the CV: as ρ_L increases, the CV shrinks.

The volume-averaging process is simplified considerably by assuming a particular form for the density distribution. Dipole plasmas are challenging to model with high physical fidelity. Power-law density scaling is commonly employed [41, 40, 47], i.e.

$$n_j = n_{j,r} \left(\frac{\hat{\psi}}{\hat{\psi}_r} \right)^{\alpha} , \tag{2.46}$$

where $n_{j,r}$ is the invariant density on an arbitrary flux contour ψ_r and the parameter α depends on a variety of factors [40], but is usually between 1∼10. Eq. (2.46) implies that density is constant along magnetic field lines and, therefore, along our CV boundary. We assume that n_i, n_e, and n_{2n} are described by this profile, which is represented in Fig. 2.1. Any perturbations to this profile are assumed to be damped on timescales much shorter than the characteristic system evolution, so interspecies reactions ($\propto n_j n_k$) do not result in higher order terms. While these assumptions sacrifice physical fidelity, they simplify the model such that spatial dependencies are functions of ψ and B only. This, combined with the fixed CV size, facilitates global modeling by reducing integrals over the CV to fixed values for a given set of input conditions. We leverage this to volume-average the model equations and drastically reduce computational load. A discussion of the validity of Eq. (2.46) and ways to build complexity in future analyses is provided in Section 3.6.

The dimensionless model equations after CV-averaging describe the rate of change of the total population and energy present in the volume. The model variables are the total normalized populations in the CV, $\hat{N}_j$, and the normalized temperatures, $\hat{T}_j$, of each tracked species as a function of time, $\hat{t}$. We derive these by normalizing and integrating the

conservation equation variables, n_j and ε_j:

$$\hat{N}_j = \oint_{V^*} \hat{n}_j \, d\hat{V} \ , \tag{2.47}$$

$$\hat{E}_j = \oint_{V^*} \hat{\varepsilon}_j \, d\hat{V} = \frac{2/3}{\gamma - 1} \hat{N}_j \hat{T}_j \ . \tag{2.48}$$

Here, $\hat{E}_j$ is the normalized total energy of species j in the CV. Combining Eqs. (2.46) and (2.47) gives the useful relation

$$\hat{n}_{j,r} = \hat{N}_j / I_{\psi^\alpha} \ , \tag{2.49}$$

where

$$I_{\psi^\alpha} = \oint_{V^*} \left(\frac{\psi}{\psi_r} \right)^\alpha \, d\hat{V} \tag{2.50}$$

is a magnetic field integral reflecting the density profile in Eq. (2.46). Relation (2.49) allows us to describe the spatially-resolved density profile, $\hat{n}_j$, from the CV-averaged solution, $\hat{N}_j$, through Eq. (2.46). Recall that V^* (defined by $\hat{\psi} > \hat{\psi}^*$) is a function of ρ_L only and $\hat{\psi}_r$ is fixed.

Interactions between tracked species, of the form $\dot{n}_j^s \propto n_j n_k R_s$, depend spatially on the species densities which both follow Eq. (2.46). Such interactions include $2n$ ionization and i-$2n$ charge exchange. After volume averaging, these terms have the form $\hat{\dot{N}}_j^s \propto \hat{n}_{j,r} \hat{n}_{k,r} I_{\psi^{2\alpha}} / \hat{\tau}_s$, where

$$I_{\psi^{2\alpha}} = \oint_{V^*} \left(\frac{\psi}{\psi_r} \right)^{2\alpha} \, d\hat{V} \tag{2.51}$$

is a magnetic field integral resulting from taking the product of tracked species densities. $\hat{\tau}_s$ is a dimensionless parameter describing the characteristic timescale of reaction s compared to its transit time across the magnet, defined as

$$\hat{\tau}_s = \frac{u_\infty / r_c}{R_s n_\infty} \ . \tag{2.52}$$

Interactions of tracked species with the neutral stream, having the form $\dot{n}_j^s \propto n_j n_{sn} R_s$, are more complicated because n_{sn} does not follow Eq. (2.46). The resultant volume-averaged interaction has the form $\hat{\dot{N}}_j^s \propto \hat{n}_{e,r} I_{sn} / \hat{\tau}_s$, where the so-called "capture integral" I_{sn} is defined as

$$I_{sn} = \int_{V^*} \left(\frac{\hat{\psi}}{\hat{\psi}_r} \right)^\alpha \hat{n}_{sn} \, d\hat{V} \ . \tag{2.53}$$

Computing this integral requires knowledge of $\hat{n}_{sn}$. Recall from Section 2.2 that we derived $\hat{n}_{sn}$ by recognizing that the only stream-plasma interactions are ionization and CX and assuming the interaction is steady-state. Thus, the stream continuity equation has the form

$$\nabla \cdot (n_{sn} u_\infty \hat{\mathbf{e}}_z) = -R_{\text{tot}} n_e n_{sn} \tag{2.54}$$

where $R_{\text{tot}} = R_{\text{iz}} + R_{\text{cx},sn}$ is the total stream reaction rate. Eq. (2.54) is normalized and solved to yield

$$\hat{n}_{sn} = \exp\left[-\frac{\hat{n}_{e,r}}{\hat{\tau}_{\text{cap}}} \int_{-\infty}^{\hat{z}} \left(\frac{\psi}{\psi_r} \right)^\alpha d\hat{z}' \right] . \tag{2.55}$$

The stream capture timescale, $\hat{\tau}_{\text{cap}}$, is defined as in Eq. (2.52) for reaction rate R_{tot}. Therefore, $\hat{n}_{e,r}/\hat{\tau}_{\text{cap}}$ represents the characteristic rate at which stream neutrals interact with the plasma. I_{sn} must be computed at each time step of the numerical solution, unlike the other CV integrals. Eq. 2.16 provides a functional fit for $I_{sn}(\rho_L, \hat{n}_{e,r}/\hat{\tau}_{\text{cap}})$ that facilitates rapid computation with reasonable accuracy.

Finally, tracked species diffusion, with the form $\dot{n}_j^{\text{dif}} \propto \nabla \cdot (D_j \nabla_\perp n_j)$, depends on the different diffusion models described in Section 2.4.1. Volume averaging results in a common scaling for each, $\hat{\dot{N}}_j^{\text{dif}} \propto \hat{D}_j \hat{n}_{j,r} I_{\text{D}}$. Here, $\hat{D}_j$ is a dimensionless, spatially invariant form of D_j specific to each diffusion model. I_D are magnetic field integrals that reflect the spatial scalings associated with D_B, D_c, D_{2n}, and density gradients. The respective integrals are

$$I_B = \oiint_{S^*} \frac{4\hat{r}}{\hat{\psi}} \left(\frac{\hat{\psi}}{\hat{\psi}_r} \right)^\alpha d\hat{S} , \tag{2.56}$$

$$I_c = \oiint_{S^*} \frac{4\hat{r}}{\hat{\psi}\hat{B}} \left(\frac{\hat{\psi}}{\hat{\psi}_r} \right)^{2\alpha} d\hat{S} , \tag{2.57}$$

$$I_{2n} = \oiint_{S^*} \frac{4\hat{r}\hat{B}}{\hat{\psi}} \, d\hat{S} . \tag{2.58}$$

Note these are surface integrals over S^* owing to Gauss' theorem. Once again, I_B, I_c, and I_{2n} are all functions of the magnetic field only. It is the different scaling with B in each D_j that yields three unique integrals.

To facilitate efficient propagation of the model, many of these control volume integrals may be approximated by functional fits. Eq. (2.16) gives a function for I_{sn}. The remaining

integrals are approximated as follows:

$$I_{\psi^4}(\hat{\psi}^*, \hat{\psi}_r) \approx \frac{0.406^{\hat{\psi}^*} - 0.309}{\hat{\psi}_r^4} , \tag{2.59}$$

$$I_{\psi^8}(\hat{\psi}^*, \hat{\psi}_r) \approx \frac{0.399 - 0.083(\hat{\psi}^*)^{3.955}}{\hat{\psi}_r^8} , \tag{2.60}$$

$$I_B(\hat{\psi}^*, \hat{\psi}_r) \approx \frac{4}{\hat{\psi}_r^4}\left(0.825 + \frac{1.35(\hat{\psi}^*)^{2.455}}{0.195 + (\hat{\psi}^*)^{2.455}}\right) , \tag{2.61}$$

$$I_{2n}(\hat{\psi}^*, \hat{\psi}_r) \approx 50.264/\hat{\psi}^* , \tag{2.62}$$

$$I_c(\hat{\psi}^*, \hat{\psi}_r) \approx \begin{cases} \frac{0.62(\hat{\psi}^*)^{1.047}}{\hat{\psi}_r^8} & \text{for } \hat{\psi}^* < 0.218 , \\ \frac{1.368(\hat{\psi}^*)^{1.564}}{\hat{\psi}_r^8} & \text{for } \hat{\psi}^* \geq 0.218 . \end{cases} \tag{2.63}$$

Note that the approximations are functions of $\hat{\psi}^*$ and $\hat{\psi}_r$ only. These functions are accurate to within $\sim$5% over a range of $\psi^* \in [.01, 1]$.

2.4.3 Global Model Equations

The final global model equations are the result of applying the volume-averaging in Section 2.4.2 to the conservation equations developed in Section 2.4.1. This system consists of five nonlinear ordinary differential equations and is solved for the time evolution of five unknowns: $\hat{N}_i$, $\hat{N}_{2n}$, $\hat{T}_i$, $\hat{T}_e$, and $\hat{T}_{2n}$. The equations describe ion/electron continuity (2.64), secondary neutral continuity (2.65), ion energy (2.67), electron energy (2.68), and secondary neutral energy (2.69) which are coupled via mass and energy transport terms. Note that the appearance of $\hat{n}_{j,r}$ is replaced with $\hat{N}_j/I_{\psi^\alpha}$ using Eq. (2.49) to highlight the model dependence on the five dimensionless variables and the CV integrals. Underbrackets are used as an aid to the reader indicating the physical process represented by each term.

Continuity Equations

Recall from Section 2.4.1 that $n_i = n_e$, so ions and electrons are described by the same continuity equation (presented here for ions). Recall also that the solution to the stream neutral continuity equation is already known [Eqs. (2.54)–(2.55)]. Thus, global model continuity consists only of that for ions and secondary neutrals:

$$\frac{d\hat{N}_i}{d\hat{t}} = - \underbrace{\left[\hat{D}_B\hat{T}_eI_B + \hat{D}_c(\hat{T}_e+\hat{T}_i)I_c\right]\frac{\hat{N}_i}{I_{\psi^\alpha}}}_{\text{dif}} + \underbrace{\hat{\dot{N}}_{\text{inj}}}_{\text{inj}} + \underbrace{\frac{\hat{N}_e\hat{N}_{2n}}{\hat{\tau}_{\text{iz}}}\frac{I_{\psi^{2\alpha}}}{(I_{\psi^\alpha})^2}}_{\text{iz},2n}$$
$$+ \underbrace{\frac{\hat{N}_e}{\hat{\tau}_{\text{iz}}}\frac{I_{sn}}{I_{\psi^\alpha}}}_{\text{iz},sn} , \tag{2.64}$$

$$\frac{d\hat{N}_{2n}}{d\hat{t}} = \underbrace{\frac{\hat{N}_i}{\hat{\tau}_{\text{cx},sn}}\frac{I_{sn}}{I_{\psi^\alpha}}}_{\text{cx},sn} - \underbrace{\hat{D}_{2n}\hat{T}_{2n}^{1/2}\hat{N}_{2n}I_{2n}}_{\text{dif}} - \underbrace{\frac{\hat{N}_e\hat{N}_{2n}}{\hat{\tau}_{\text{iz}}}\frac{I_{\psi^{2\alpha}}}{(I_{\psi^\alpha})^2}}_{\text{iz},2n} . \tag{2.65}$$

Diffusion is a loss for both species, with $\hat{D}_B$, $\hat{D}_c$, and $\hat{D}_{2n}$ being dimensionless, spatially invariant forms of the diffusion coefficients. These are defined in Appendix A Eqs. (A.7), (A.8), and (A.20) respectively. The particle injection rate,

$$\hat{\dot{N}}_{\text{inj}} = \frac{\dot{N}_i^{\text{inj}}}{n_\infty u_\infty r_c^2} , \tag{2.66}$$

represents the volume-averaged plasma source injection as a fraction of the characteristic stream neutral flux.

Eqs. (2.64) and (2.65) reveal how the capture integral, I_{sn}, acts to couple the flow and plasma. There is a direct source of plasma from ionization of stream neutrals, as well as an indirect source when CX with the stream creates $2n$s that are reionized. Both of these stream interaction processes are functions of I_{sn} and supply ions from outside the CV with no corresponding loss term from another model equation.

Energy Equations

Conservation of energy is considerably more complex. Despite eliminating the need for sn energy balance in Section 2.4.1, tracking system energy requires three distinct, nonlinear equations describing ions, electrons, and secondary neutrals:

$$\frac{2/3}{\gamma-1}\frac{d(\hat{N}_i\hat{T}_i)}{d\hat{t}} = - \underbrace{\frac{2/3}{\gamma-1}\left[\hat{D}_B\hat{T}_eI_B+\hat{D}_c(\hat{T}_e+\hat{T}_i)I_c\right]\frac{\hat{N}_i\hat{T}_i}{I_{\psi^\alpha}}}_{\text{dif}} + \underbrace{\left(\frac{1}{\hat{\tau}_{\text{cx},sn}}-\hat{Q}_{sn,i}\right)\hat{N}_i\frac{I_{sn}}{I_{\psi^\alpha}}}_{\text{cx},sn}$$
$$+ \underbrace{\frac{\hat{N}_e}{\hat{\tau}_{\text{iz}}}\frac{I_{sn}}{I_{\psi^\alpha}}}_{\text{iz},sn} + \underbrace{\hat{P}_{i,\text{inj}}}_{\text{inj}} + \underbrace{\frac{3}{2}\left(\hat{Q}_{i,2n}-\hat{Q}_{2n,i}\right)\hat{N}_i\hat{N}_{2n}\frac{I_{\psi^{2\alpha}}}{(I_{\psi^\alpha})^2}}_{\text{cx},2n} + \underbrace{\frac{\hat{N}_e\hat{N}_{2n}\hat{T}_{2n}}{\hat{\tau}_{\text{iz}}}\frac{I_{\psi^{2\alpha}}}{(I_{\psi^\alpha})^2}}_{\text{iz},2n}$$
$$+ \underbrace{2M_{e/i}\frac{\hat{N}_e^2}{\hat{\tau}_{ie}}\frac{\hat{T}_e-\hat{T}_i}{\hat{T}_e^{3/2}}\frac{I_{\psi^{2\alpha}}}{(I_{\psi^\alpha})^2}}_{\text{coll}} \ , \tag{2.67}$$

$$\frac{2/3}{\gamma-1}\frac{d(\hat{N}_e\hat{T}_e)}{d\hat{t}} = \underbrace{\left(M_{e/sn}-\hat{\epsilon}_{\text{ion}}\right)\frac{\hat{N}_e}{\hat{\tau}_{\text{iz}}}\frac{I_{sn}}{I_{\psi^\alpha}}}_{\text{iz},sn} + \underbrace{\hat{P}_{e,\text{inj}}}_{\text{inj}} + \underbrace{\left(M_{e/2n}\hat{T}_{2n}-\hat{\epsilon}_{\text{ion}}\right)\frac{\hat{N}_e\hat{N}_{2n}}{\hat{\tau}_{\text{iz}}}\frac{I_{\psi^{2\alpha}}}{(I_{\psi^\alpha})^2}}_{\text{iz},2n}$$
$$- \underbrace{\frac{2/3}{\gamma-1}\left[\hat{D}_B\hat{T}_eI_B+\hat{D}_c(\hat{T}_e+\hat{T}_i)I_c\right]\frac{\hat{N}_e\hat{T}_e}{I_{\psi^\alpha}}}_{\text{dif}}$$
$$- \underbrace{2M_{e/i}\frac{\hat{N}_e^2}{\hat{\tau}_{ie}}\frac{\hat{T}_e-\hat{T}_i}{\hat{T}_e^{3/2}}\frac{I_{\psi^{2\alpha}}}{(I_{\psi^\alpha})^2}}_{\text{coll}} \ , \tag{2.68}$$

$$\frac{2/3}{\gamma-1}\frac{d(\hat{N}_{2n}\hat{T}_{2n})}{d\hat{t}} = \underbrace{\frac{3}{2}\left(\hat{Q}_{2n,i}-\hat{Q}_{i,2n}\right)\hat{N}_i\hat{N}_{2n}\frac{I_{\psi^{2\alpha}}}{(I_{\psi^\alpha})^2}}_{\text{cx},2n} + \underbrace{\hat{N}_i\hat{Q}_{sn,i}\frac{I_{sn}}{I_{\psi^\alpha}}}_{\text{cx},sn} - \underbrace{\frac{\hat{N}_e\hat{N}_{2n}}{\hat{\tau}_{\text{iz}}}\hat{T}_{2n}\frac{I_{\psi^{2\alpha}}}{(I_{\psi^\alpha})^2}}_{\text{iz},2n}$$
$$- \underbrace{\frac{2/3}{\gamma-1}\hat{D}_{2n}\hat{T}_{2n}^{3/2}\hat{N}_{2n}I_{2n}}_{\text{dif}} \ . \tag{2.69}$$

Notice that many energy terms result simply from the transfer of internal energy associated with the continuity terms. The dimensionless injected power,

$$\hat{P}_{j,\text{inj}} = \frac{5}{3}\hat{T}_{j,\text{inj}}\dot{\hat{N}}_{\text{inj}} \ , \tag{2.70}$$

is scalar with dimensionless particle injection following Eqs. (2.41)–(2.42). Several more terms in Eqs. (2.64)–(2.65) result from energy transfer processes without an associated net particle transfer. For instance, CX reactions and Coulomb collisions conserve particle populations but are mechanisms for exchanging thermal energy between species [with $\hat{Q}_{j,k}$ and $\hat{\tau}_{ie}$ defined in Eqs. (A.12) and (A.2), respectively]. Although ionization terms are similar

to their continuity counterparts for i and $2n$, the electrons incur an additional loss of

$$\hat{\epsilon}_{\text{ion}} = \frac{\epsilon_{\text{ion}}}{m_{sn} u_\infty^2 / 2} \tag{2.71}$$

which is the effective ionization cost [Eq. (A.16)] normalized by stream kinetic energy.

2.5 Conclusion

The global model described by Eqs. (2.64), (2.65), (2.67), (2.68), and (2.69) is a useful tool for simulating the flow interaction with the magnetoshell dipole plasma. In the derivation of this model, we have considered the species and reactions abstractly, neglecting the implementation for any particular atmosphere. In Chapter 3, we will solve the model using argon to understand the physics that govern the interaction and extract scaling laws to inform plasma aerocapture design.

Chapter 3

PHYSICS AND SCALING OF MAGNETOSHELL PLASMAS

In this chapter, we investigate the role of the processes described in Chapter 2 in driving the overall behavior of the magnetoshell in a hypersonic neutral flow. First, the implementation of the global model for an argon flow/plasma is detailed. We then examine the evolution of the system from the initiation of the simulation to a steady state equilibrium. Steady state conditions across a range of input parameters are analyzed to determine how magnetoshell performance scales with relevant design variables. Distinct physical regimes are found and the conditions for transition between them are derived.

3.1 Model Implementation

The interaction is simulated for argon flow and plasma by solving Eqs. (2.64)–(2.65) and (2.67)–(2.69) over a timescale long enough to reach equilibrium. Details of the argon model are provided in Appendix A. The LSODA differential solver [37] is used and outputs the time evolution of $\hat{N}_i$, $\hat{N}_{2n}$, $\hat{T}_i$, $\hat{T}_e$, and $\hat{T}_{2n}$. We first use these to examine the nature of the system as it evolves toward a steady state in a particular simulation. Then, we run an array simulations across broad ranges of inputs n_∞, u_∞, r_c, B_0, and Γ_{inj}, extracting the equilibrium solutions to examine physical scaling with these parameters.

In the following, the reference surface for computations such as Eq. (2.50) is $\hat{\psi}_r = \hat{\psi}^*$ unless otherwise noted. We use $\alpha = 4$ for the density profiles given by Eq. (2.46). While this approach is a simplification, there are several justifications. First, this value of α commonly appears in the literature for the theoretical stationary state of a dipole plasma [39, 40, 48]. Second, a constant α enables computation of the CV integrals independent of the numerical evolution of the system, a stated motivation for our global model approach. Finally, we observe that the results to follow are not qualitatively sensitive to the specific density profile employed. Previous work using $n_j \propto B$ exhibited the same general character

of the plasma-flow interaction [21, 49]. Thus, the present implementation provides a lens to obtain physical insight into the interaction such that appropriate complexity can be developed later.

3.2 Temporal Behavior

To gain intuition on how the coupled mass and energy transfer processes in Section 2.4.1 drive the system toward equilibrium, we first examine the initial time evolution of the interaction during a single simulation. Fig. 3.1 shows the output of a simulation with $n_\infty = 10^{18}$ m^{-3}, $u_\infty = 12$ km/s, $B_0 = 0.25$ T, $r_c = 1$ m, and $\Gamma^{\text{inj}} = 5$ mg/s. At these conditions, $\hat{t} = 12$ corresponds to $t = 1$ ms. The initial conditions are $\hat{N}_i(0) = \hat{N}_{2n}(0) = 1$ and $\hat{T}_i(0) = \hat{T}_{2n}(0) = \hat{T}_e(0) = 0.1$. The populations $\hat{N}_i$ and $\hat{N}_{2n}$ both build up gradually before suddenly increasing exponentially to their equilibria. This sudden increase is accompanied by a sharp drop in all species temperatures relative to the stream energy. The system effectively reaches equilibrium within about 20 ms ($\hat{t} \sim 240$), though this time decreases if the initial conditions $\hat{N}_i(0)$ and $\hat{N}_{2n}(0)$ are increased. The steady-state populations and temperatures, however, are only sensitive to the scaling parameters (n_∞, etc.) and not the initial conditions. Note that the timescale of evolution in Fig. 3.1 is much slower than the characteristic particle transit time ($\hat{t} \gg 1$). This justifies our earlier assumption that density distrubutions can be described by their equilibrium profiles.

Fig. 3.2 shows what this density evolution looks like spatially. At first, the control volume contains very little plasma and the flow is only affected by the extreme magnetic fields at the ring current [Fig. 3.2(a)]. After the sharp jump [Fig. 3.2(b)], the density has increased substantially and the flow is impeded in the region around the magnet. The plasma continues to absorb flow particles, eventually reaching a steady state [Fig. 3.2(c)] where its density is orders of magnitude higher than the freestream throughout the CV and it produces a wake several times the size of the magnet. Note at steady state that the neutral flow is entirely absorbed over the radial extent of the control volume.

Fig. 3.3 reveals the underlying processes behind this evolution to steady state. Charge exchange between ions and stream neutrals begins depositing secondary neutrals in the control volume, which are lost entirely to diffusion for $\hat{t} < 100$ [Fig. 3.3(b)]. Meanwhile, ions

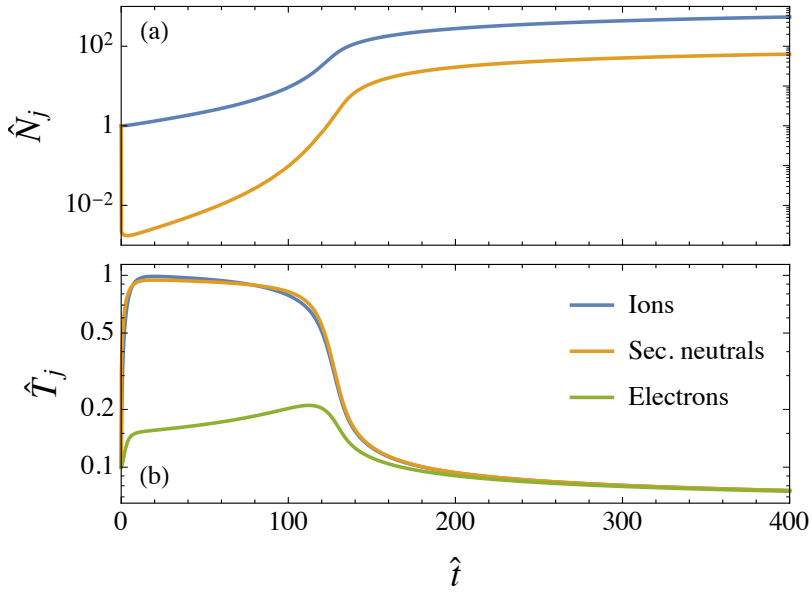

Figure 3.1: Time-resolved numerical solutions to the model outputs: (a) populations $\hat{N}_i$ and $\hat{N}_{2n}$ and (b) temperatures $\hat{T}_i$, $\hat{T}_e$, and $\hat{T}_{2n}$. Simulation conditions are $n_\infty = 10^{18}$ m^{-3}, $u_\infty = 12$ km/s, $B_0 = 0.25$ T, $r_c = 1$ m, and $\Gamma^{\text{inj}} = 5$ mg/s.

and electrons build up slowly from ionization of stream neutrals during this time [Fig. 3.3(a)]. As the ion population grows, charge exchange becomes more frequent, producing more secondary neutrals. This results in a runaway effect where the growing reservoir of neutrals becomes an ionization source that causes an apparent critical ionization effect around $\hat{t} = 100$. Here the plasma population exponentially increases [Fig. 3.3(a)], driven by ionization of secondary neutrals produced from charge exchange with the stream. In steady state, the energetic electrons sustain this secondary neutral ionization [Fig. 3.3(e)]. Their energy is derived from collisions with ions that are heated by charge exchange with the stream [Fig. 3.3(c)]. In this manner, charge exchange provides both the neutral reservoir and the energy source for a critical ionization effect to take place in the control volume.

3.3 Steady State Regimes

Together, Figs. 3.1–3.3 provide comprehensive intuition about the nonlinear interdependence of the model equations and the coupled interaction between the plasma and flow. We

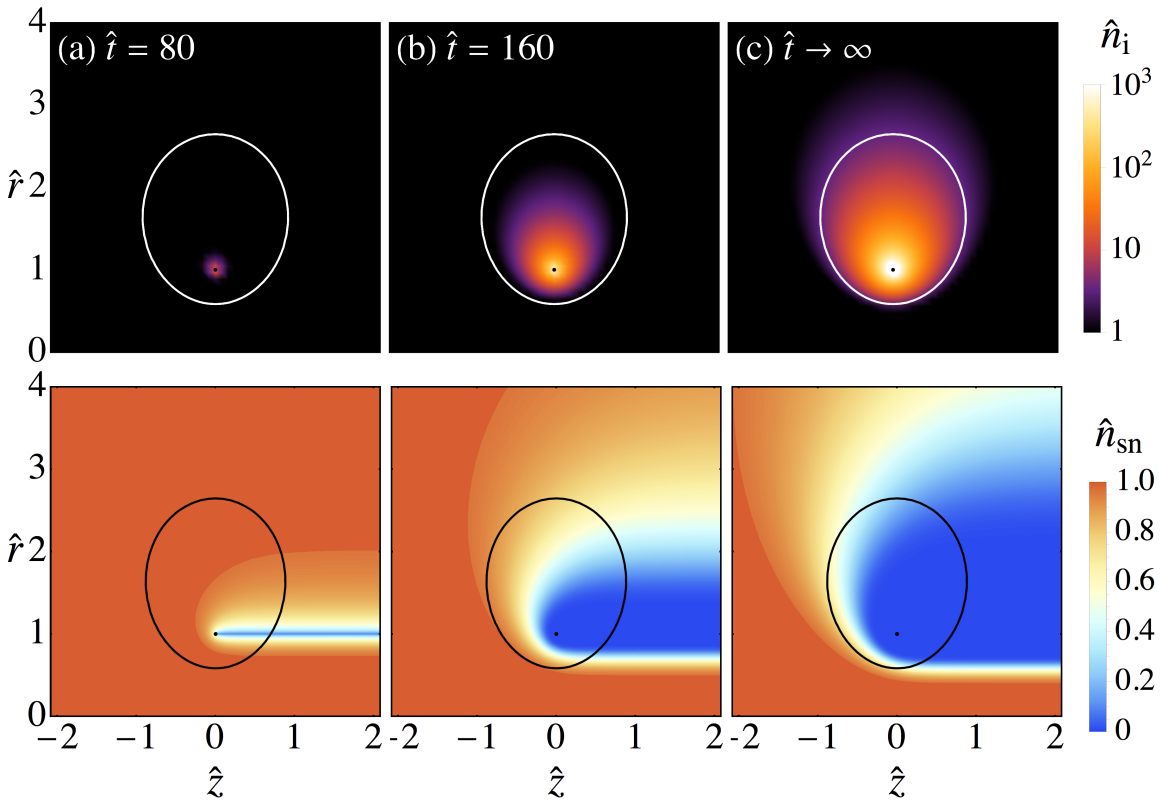

Figure 3.2: Spatial distribution of plasma and stream densities as the system evolves to steady state. Three times are sampled: (a) right before the sudden density increase depicted in Fig. 3.1; (b) right after the sudden density increase; (c) steady state. The control volume boundary is shown as a solid line. Simulation conditions are $n_\infty = 10^{18}$ m^{-3}, $u_\infty = 12$ km/s, $B_0 = 0.25$ T, $r_c = 1$ m, and $\Gamma^{\text{inj}} = 5$ mg/s.

now seek to identify physical regimes and scaling of the interactions by investigating the steady-state solutions to an array of simulations, each with different magnet and flow conditions. Fig. 3.4 shows the dependence of the boundary density $\hat{n}^*$ (i.e. on ψ^*) and average temperatures $\hat{T}$ on the freestream velocity u_∞. In contrast to the three tracked species, $\hat{n}_{sn}$ is not invariant along field lines, so we compute $\hat{n}^*_{sn}$ at the furthest downstream point on S^* as a characteristic measure of sn density. Note in Fig. 3.4 that velocity is normalized by Alfvén's [26] critical velocity,

$$u_{\text{cr}} = \sqrt{\frac{2U_{\text{iz}}}{m_{sn}}} \tag{3.1}$$

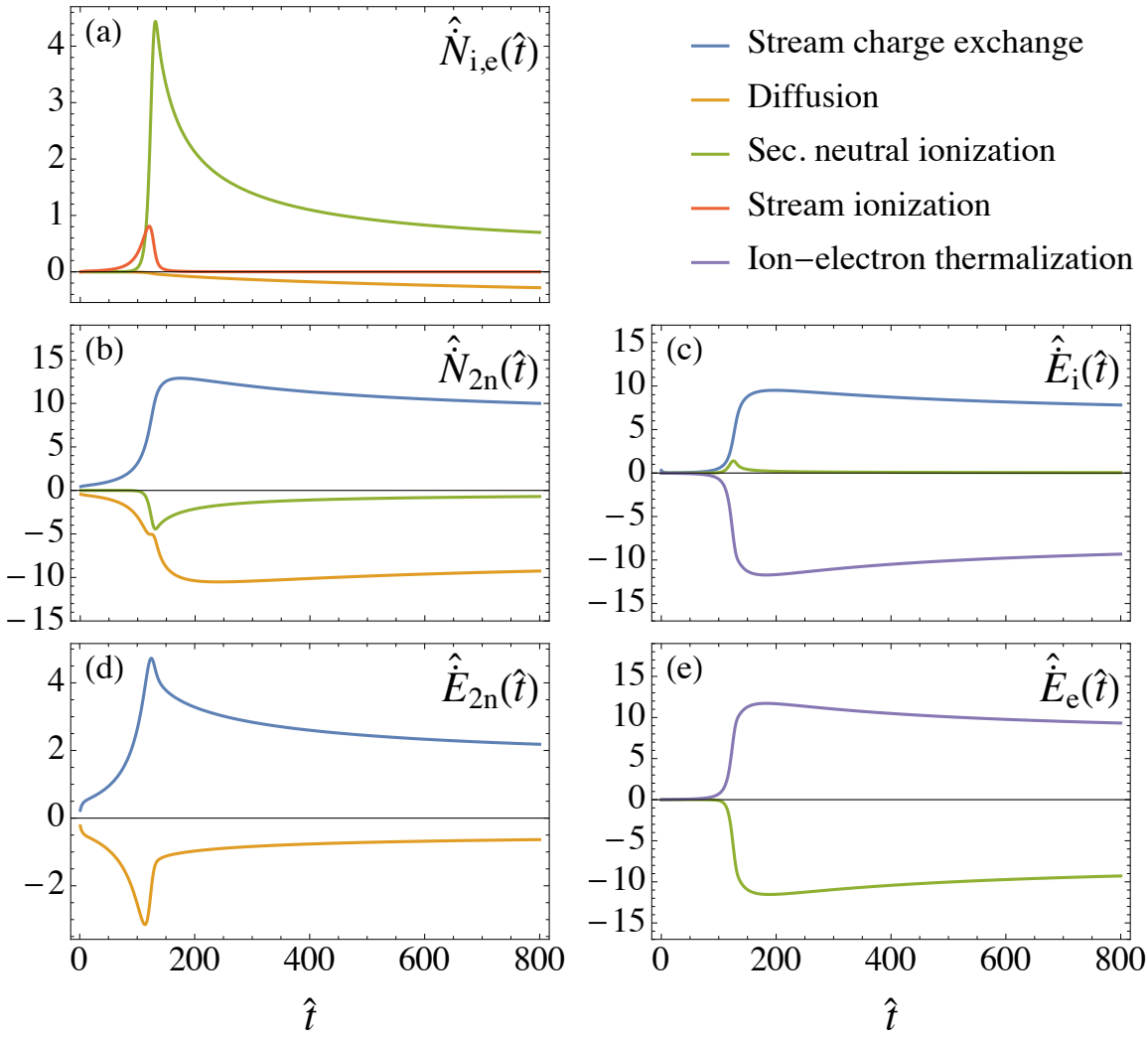

Figure 3.3: Temporal solution of the contributing terms in the control volume equations. Plots correspond to the dimensionless model equations as follows: (a) Eq. (2.64), (b) Eq. (2.65), (c) Eq. (2.67), (d) Eq. (2.69), and (e) Eq. (2.68). The simulation conditions are $n_\infty = 10^{18}$ m^{-3}, $u_\infty = 12$ km/s, $B_0 = 0.25$ T, $r_c = 1$ m, and $\Gamma^{\text{inj}} = 5$ mg/s.

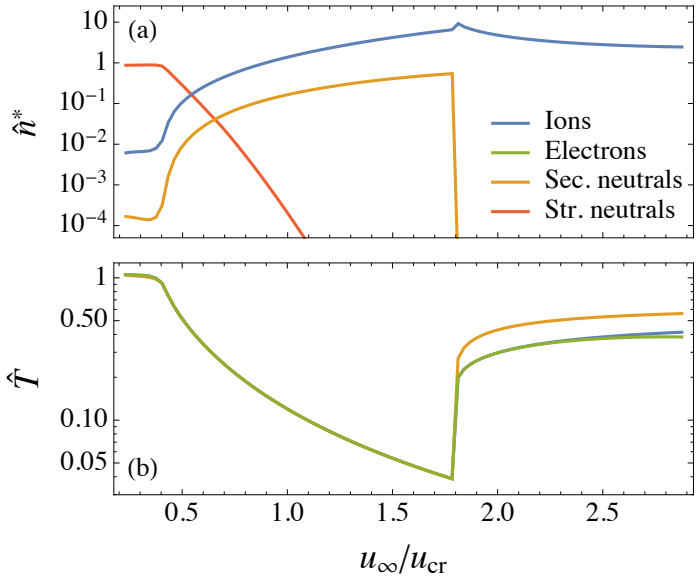

Figure 3.4: (a) Reference densities, $\hat{n}^*$, and (b) average temperatures, $\hat{T}$, of all system species. $\hat{n}_{i,e}$ and $\hat{n}^*_{2n}$ are invariant on the reference surface S^* while $\hat{n}^*_{sn}$ is computed at the downstream-most point of the reference surface. The fixed conditions are $n_\infty = 10^{18}$ m^{-3}, $B_0 = 0.25$ T, $r_c = 1$ m, and $\Gamma^{\text{inj}} = 5$ mg/s.

where U_{iz} is the first ionization energy ($u_{\text{cr}} = 8.7$ km/s for argon). Like in the temporal solutions, a critical ionization effect is apparent. At low velocities, very little of the flow is converted to plasma ($\hat{n}^*_{sn} \sim 1$) and few ions are present. The model species are thermalized with the stream ($\hat{T} \sim 1$) by CX interaction. As the velocity increases past $u_\infty \sim 0.4u_{\text{cr}}$, there is a sudden exponential increase in plasma and secondary neutral density, while $\hat{n}^*_{sn}$ begins gradually sinking to zero. This is accompanied by a sharp drop in the species temperatures. While plasma dominates in this velocity range, there is a significant fraction of secondary neutrals present, with $\hat{n}^*_{2n}$ roughly 10% of $\hat{n}^*_i$. Increasing velocity past $u_\infty \sim 1.8u_{\text{cr}}$, a third distinct regime is apparent where the plasma becomes fully ionized. Secondary neutral density effectively reduces to zero though the plasma maintains its high density. The plasma density spikes for a brief window where stream CX remains a significant plasma source (evidenced later by Fig. 8), then gradually declines with increasing velocity due to increased diffusion and a shrinking CV [Eq. (2.6)]. Species temperatures approach the order of the stream energy and continue to rise with increasing velocity.

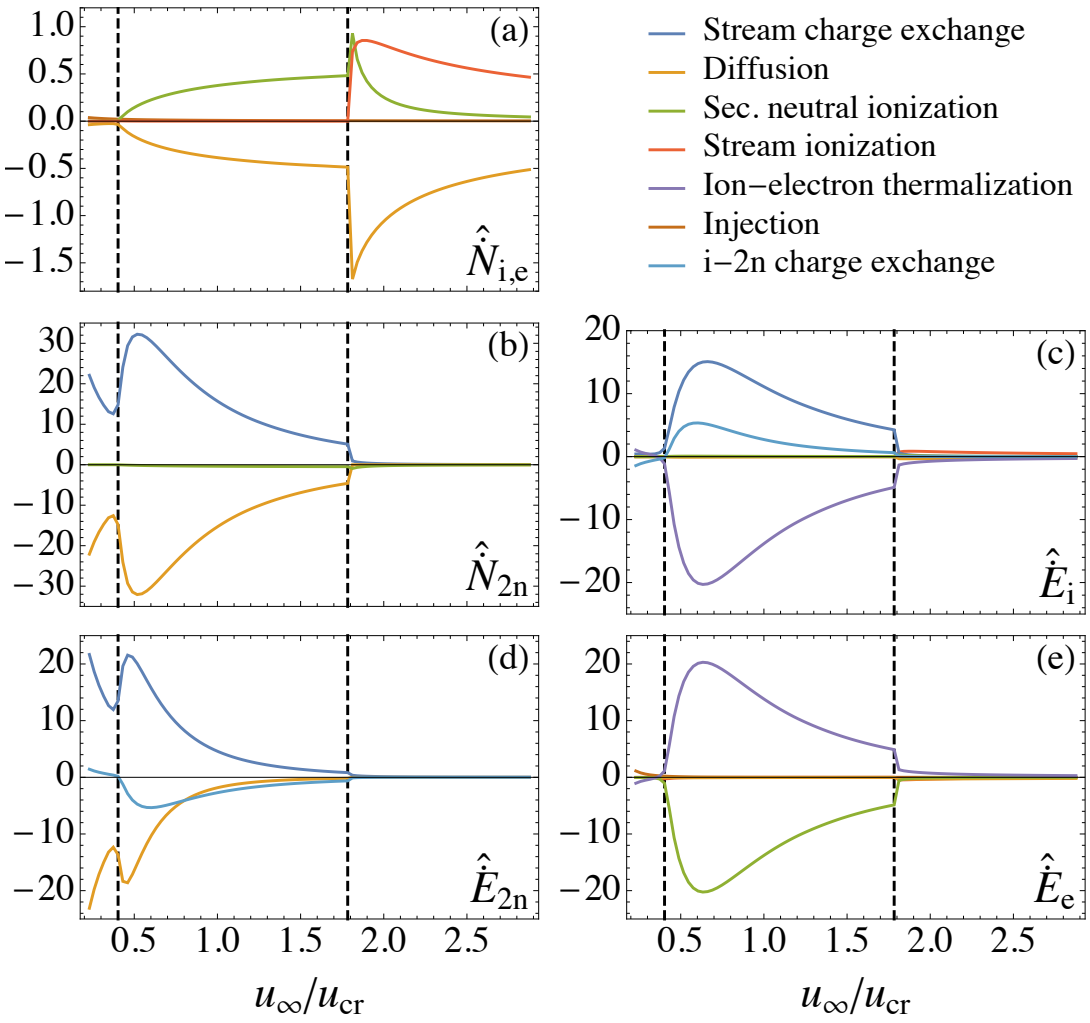

Figure 3.5: Steady state of significant contributing terms in the control volume equations as a function of stream velocity. Plots correspond to the dimensionless model equations as follows: (a) Eq. (2.64), (b) Eq. (2.65), (c) Eq. (2.67), (d) Eq. (2.69), and (e) Eq. (2.68). Black dotted lines distinguish the three physical regimes I (left), CX (middle), and CIV (right). The fixed conditions are $n_\infty = 10^{18}$ m^{-3}, $B_0 = 0.25$ T, $r_c = 1$ m, and $\Gamma^{\text{inj}} = 5$ mg/s.

As with the temporal solutions of Figs. 3.1–3.3, the steady-state regimes observed in Fig. 3.4 are governed by the physical processes that connect the model equations. In Fig. 3.5, we show the steady-state contributions of mass and energy transfer terms that drive the equilibrium solutions as a function of the input u_∞. In other words, all of the curves shown correspond to the steady-state values of right hand-side terms in Eqs. (2.64), (2.65), (2.67), (2.68), and (2.69). Black dotted lines indicate the transitions between the three regimes that we characterize according to the main source of plasma sustainment as follows:

- **Injection (I) regime:** At low velocities, the only energy deposited into the plasma comes from the power injection term $\hat{P}_{\text{inj}}$ [Fig. 3.5(e)]. All injected mass and energy diffuses from the control volume. There is substantial charge exchange with the stream [Fig. 3.5(b)] but it makes no net contribution because the ionization time is much longer than the $2n$ diffusion time. Interestingly, even though stream charge exchange supplies new ions, the kinetic energy of flow neutrals is too low to heat the ion population. In fact, CX is mostly an energy sink in this regime [Fig. 3.5(c)]. Because the injected power and mass dominate over any plasma/flow interaction, we define this as the "injection regime." Note that plasma sustainment in the I regime requires an artificial source, without which the plasma would extinguish.

- **Charge exchange (CX) regime:** In the mid-velocity regime, a large spike is observed in the stream CX contribution to the ion energy equation [Fig. 3.5(c)], heating the ions with flow kinetic energy. This energy, in addition to that from CX with $2n$s, is transferred to the electron population via Coulomb interaction. Electrons subsequently have enough energy to ionize some of the $2n$ resevoir resulting from the original stream CX reactions [Fig. 3.5(e)]. This forms a critical ionization feedback loop: ion-stream CX produces abundant secondary neutrals and simultaneously heats the electron population; electron ionization of $2n$s augments the ion population, further increasing CX with the stream. This process is distinct from most models of critical ionization in that it is driven by charge exchange, so we refer to this as the "CX regime." Note that negligible energy is lost in plasma diffusion, instead leaving the system entirely through $\hat{\epsilon}_{\text{ion}}$ (i.e. ionization and radiation) and $2n$ diffusion

[Fig. 3.5(d)]. This effect eases the energy burden on electrons to sustain critical ionization, ultimately enabling the low threshold velocity observed.

- **Critical ionization velocity (CIV) regime:** The second regime transition at high velocities occurs when the plasma starts ionizing the stream directly. Ionization supplies the bulk of ion energy by converting stream kinetic energy to the plasma [Fig. 3.5(c)]. This again serves to heat the electrons through Coulomb interaction, enabling them to continue ionizing stream particles directly. This feedback loop of energy transfer is the classic manifestation of the critical ionization phenomenon, so we term this the "CIV regime." Because the electron temperature is higher in this regime, failed ionizations (scattering and excitations) are less likely so ionization losses are reduced. Therefore, diffusion becomes an equally important energy loss mechanism for electrons. Note also that $\hat{n}_i^*$ now decreases with u_∞ due to a combination of increased Bohm diffusion as $\hat{T}_e$ rises and shrinking of the ion-trapping region according to Eq. (2.7).

Figs. 3.4 and 3.5 clearly demonstrate that plasma sustainment is driven by injection, charge exchange, and ionization in three distinct regimes. We are primarily interested in the extent to which coupling between the flow and plasma drives this behavior. Recall from Section 2.4.2 that $\hat{n}_{e,r}/\hat{\tau}_{\text{cap}}$ is the critical term that couples the plasma properties to the flow through I_{sn} [Eq. (2.53)]. Whereas earlier this parameter was defined for an arbitrary contour ψ_r, here we define it on the CV boundary, $\psi_r = \psi^*$, to represent the lower bound of reaction rate in the CV. We examine the behavior of ζ_s^* in the three regimes where

$$\zeta_s^* = \frac{R_s n_e^*}{u_\infty / r_c} = \hat{n}_e^* / \hat{\tau}_s \tag{3.2}$$

is the rate of reaction s (either CX or ionization) on stream neutrals at the CV boundary compared with the neutral rate of transit across the magnet. Thus, $\zeta_s^* \gtrsim 1$ implies significant flow-plasma interaction (and therefore mass and energy absorption) within the control volume.

Since the stream only undergoes CX or ionization by the plasma, let us define the total reaction parameter $\zeta_{\text{tot}}^* = \zeta_{\text{cx},sn}^* + \zeta_{\text{iz}}^*$. These three rates are shown as a function of

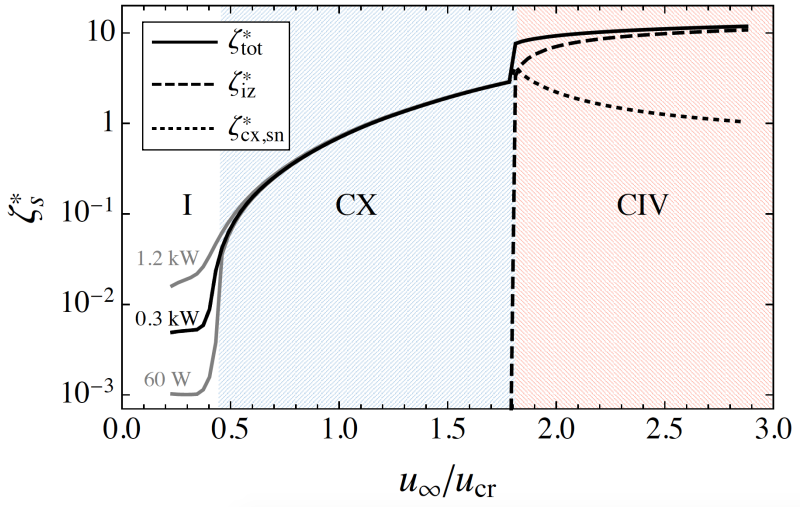

Figure 3.6: The reaction rates, ζ_s^*, reveal three distinct physical regimes. Plasma-flow interaction strengthens with increasing injection power ($\dot{E}_e^{\text{inj}} = 60$ W–1.2 kW) in the I regime. The CX regime is dominated by charge exchange reactions while the CIV regime exhibits strong ionization of the stream. The reference surface is $\psi_r = \psi^*$ and the fixed conditions are $n_\infty = 10^{18}$ m^{-3}, $B_0 = 0.25$ T, $r_c = 1$ m, and $\Gamma^{\text{inj}} = 5$ mg/s (corresponding to the 0.3 kW curve).

freestream velocity in Fig. 3.6. In the injection regime, overall reaction with the plasma is quite low, though CX dominates over ionization. This explains why Figs. 3.5(a-b) show substantial charge exchange with the stream but no significant accumulation of plasma in the injection regime. Fig. 3.6 also demonstrates that increasing injected power directly impacts ζ_{tot}^* in the I regime. The CX regime is characterized by a sharp and monotonic increase in $\zeta_{\text{cx},sn}^*$, which drives ζ_{tot}^* high enough to yield significant interaction between the plasma and flow. ζ_{iz}^* remains quite low until a drastic jump denoting the CIV regime. Here, stream ionization is so strong it drives ζ_{tot}^* to its maximum even while the CX rate declines. Figs. 3.5 and 3.6 offer an understanding of the governing physics within these three regimes; we now examine the mechanisms by which the system transitions between these states.

3.4 Regime Transitions

The existence and nature of the flow interaction regimes described in Section 3.3 strongly depend on the properties of the neutral flow and magnet. Little and Kelly [34] have previously derived theoretical threshold criteria for the I (injection), CX, and CIV regimes as a function of the normalized electron diffusion timescale ($\hat{\tau}_e$), particle capture timescale ($\hat{\tau}_{\text{cap}}$), ion-electron energy transfer timescale ($\hat{\tau}_{ie}$), and the ratio of the effective ionization energy cost to the kinetic energy of stream neutrals ($\hat{\epsilon}_{\text{ion}}$). Here, we examine these thresholds from the perspective of the global modeling results to understand the transition between regimes now that particular mass and energy transfer processes are considered.

In Fig. 3.7(a), we show how the I, CX, and CIV regimes manifest in $\hat{N}_i$ as a function of u_∞ for a range of magnetic field strengths. For four cases of $B_0 \geq 25$ mT, the plasma undergoes both I-CX and CX-CIV mode transitions as u_∞ is increased. Interestingly, the I-CX threshold velocity decreases as B_0 increases, exhibiting values both less than and greater than u_{cr}. Unlike the I-CX mode transition, the threshold value of u_∞ for the CX-CIV mode transition is always greater than u_{cr} and insensitive to B_0. It is also clear from Fig. 3.7(a) that neither of the CX or CIV flow-sustained regimes exists below a critical magnetic field strength, irrespective of the flow velocity. Notably, a modest reduction in B_0 from 25 mT to 10 mT can have profound consequences on the steady-state nature of the flow/plasma interaction for the conditions considered in Fig. 3.7(a). This result implies that the lower limit on magnetic field strength observed in CIV studies [27] may be understood from energy confinement considerations without invoking collective heating; this is discussed in Section 3.6.

Little and Kelly [34] derived a general set of physical requirements for each flow regime and presented a map of these requirements as a function of the quantities $\hat{\tau}_e/\hat{\tau}_{\text{cap}}$, $\hat{\tau}_{ie}/\hat{\tau}_{\text{cap}}$, and $\hat{\epsilon}_{\text{ion}}$. The regime mapping in the limit $\hat{\tau}_{ie} \ll \hat{\tau}_{\text{cap}}$ (which is valid across all simulation cases) is reproduced here in Fig. 3.7(b), onto which the data presented in Fig. 3.7(a) are projected. Fig. 3.7 demonstrates clear agreement between the theoretical framework describing the steady-state regimes and the results of empirical data-supported global modeling. For large B_0, increasing u_∞ within the I regime decreases both $\hat{\epsilon}_{\text{ion}}$ (leftward shift) and $\hat{T}_i$ (up-

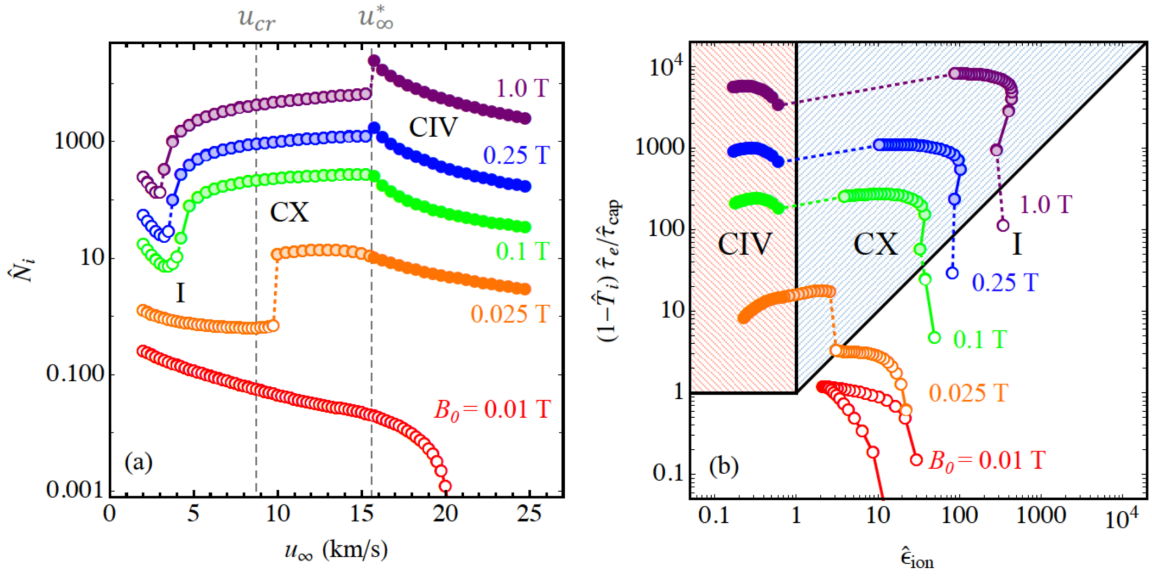

Figure 3.7: (a) Ion population, $\hat{N}_i$, as a function of neutral flow velocity, u_∞, for magnetic field strengths from $B_0 = 0.01$ to 1 T. The fixed conditions are $n_\infty = 10^{18}$ m^{-3}, $r_c = 1$ m, and $\Gamma_{\text{inj}} = 3$ mg/s. Data points indicate: (○) I regime; (●) CX regime; and (●) CIV regime. Dashed vertical lines denote u_{cr} [Eq. (3.1)] and the CIV threshold velocity, u^*_∞ [Eq. (3.4)]. Results from panel (a) are plotted on the flow regime map in panel (b). Solid black lines mark the flow regime boundaries derived by Little and Kelly [34].

ward shift). Eventually the I-CX mode transition boundary is reached where the energy deposited into the plasma via stream charge exchange is large enough to outweigh ionization losses. The curves shift upward following the I-CX mode transition due to a combination of decreased $\hat{T}_i$ and increased $\hat{\tau}_e$. The slight rightward shift immediately after the transition can be explained by increased collisional excitation losses associated with a decrease in $\hat{T}_e$ [Appendix A, Eqs. (A.16)–(A.18)]. Further increasing u_∞, the flow eventually transitions into the CIV regime where the energy deposited into the plasma via stream neutral ionization outweighs losses due to both ionization and thermal diffusion. The regime requirements mapping also explains why the $B_0 = 0.01$ T case in Fig. 3.7(a) does not transition into a flow-sustained regime with increasing u_∞. Specifically, since the diffusion coefficients scale inversely with B, the energy lost to particle diffusion is greater than the energy captured from the neutral flow for all values of u_∞.

The CX-CIV threshold velocity can be derived analytically using the energy constraint for the CIV mode. Detailed by Little and Kelly [34] and summarized here, the total energy balance for the system is observed to consist of the kinetic energy gained from ionizing a stream particle and the subsequent loss due to ionization cost and ultimate diffusion of the resulting charged particles. In the limit $\hat{\tau}_{ie} \ll \hat{\tau}_{\text{cap}}$, $\hat{T}_e \approx \hat{T}_i$, in which case the dimensional CIV mode energy balance can be written

$$\frac{1}{2} m_{sn} u_\infty^2 = \epsilon_{\text{ion}}(T_e) + 3T_e \equiv \epsilon_{\text{tot}}(T_e), \tag{3.3}$$

where we have defined ϵ_{tot} as the sum of energy lost to ionization and thermal diffusion of ions and electrons. Because $\epsilon_{\text{ion}}(T_e)$ decreases monotonically with T_e [Eq. (A.16)], $\epsilon_{\text{tot}}(T_e)$ has a definite minimum. Therefore, there exists a minimum value of u_∞ to satisfy Eq. (3.3), below which the equality does not hold and the CIV regime cannot exist. This threshold can be written symbolically as

$$u_\infty^* = \sqrt{\frac{2\text{min}\{\epsilon_{\text{tot}}(T_e)\}}{m_{sn}}} \ . \tag{3.4}$$

For the argon model used here, we find the minimum occurs around $T_e \approx 6$ eV and has a value $\epsilon_{\text{tot}} \approx 51$ eV. Using Eq. (3.4), the threshold velocity is calculated to be $u_\infty^* \approx$ 15.6 km/s. This value, marked in Fig. 3.7(a), accurately predicts the CX-CIV transition observed from the global model results.

3.5 Plasma/Flow Coupling

The global model approach thus far provides a detailed look at the net exchange of mass and energy between the flow and plasma. This total exchange is especially important to plasma aerocapture technologies which propose to leverage the atmospheric flow for plasma sustainment. However, the control volume by definition only represents particles trapped by the dipole field. We seek to distinguish these so-called "absorbed" particles from those that may be ionized outside the control volume, which are not accounted for in the model but may still influence the coupling between the plasma and stream.

We examine flow absorption by summing the stream ionization and stream CX contributions to mass/energy in the global model equations. Fig. 3.8 shows this for three different

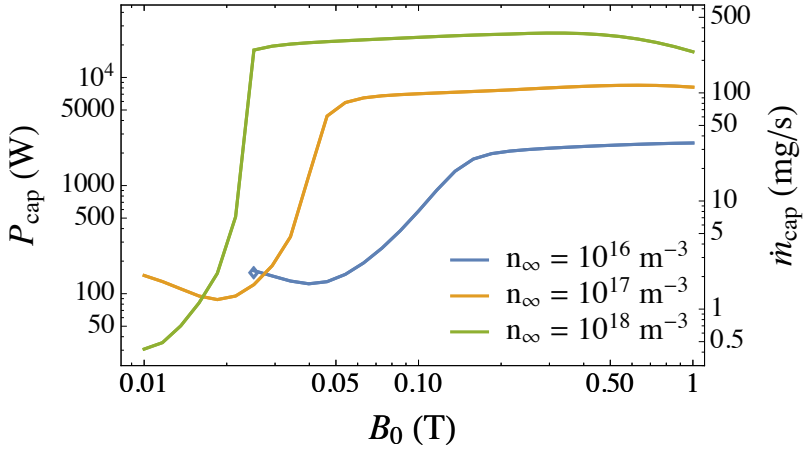

Figure 3.8: Rate of energy (P_{cap}) and flow mass ($\dot{m}_{\text{cap}}$) absorption by the plasma. The fixed conditions are $u_\infty = 12$ km/s, $r_c = 1$ m, $\Gamma^{\text{inj}} = 5$ mg/s, and $P_{\text{inj}} = 300$ W. The model solution is intractable at $n_\infty = 10^{16}$ m^{-3} for $B_0 < 25$ mT, implying the dipole is unsustainable below this field strength for the low density case.

cases of n_∞ exhibiting I-CX mode transitions. P_{cap} and $\dot{m}_{\text{cap}}$ represent the rates of energy and mass absorption, respectively, from the stream by the plasma. The transition to the CX regime is apparent as an order-of-magnitude enhancement in flow absorption. Interestingly, the mode transition is observed here where B_0 is the variable parameter instead of u_∞. This is consistent with the scaling predicted by Little and Kelly [34]; the characteristic electron diffusion time increases with magnetic field strength, eventually reaching a threshold where the diffusion time exceeds a critical value, $\hat{\tau}_e > \hat{\tau}_e^*$, and massive intake of flow energy is possible. The shift of the mode transition to lower B_0 at higher n_∞ is also expected, since faster characteristic diffusion can be tolerated with the increase in captured energy. Consistent with our understanding of the I regime, we see that the flow mass absorbed before the mode transition is on the order of the injected mass, while after the transition the flow sustains the plasma with several orders more mass and many kW of power. This has implications for the potential of a dipole plasma to effectively utilize in-situ atmospheric flow to fuel a plasma aerocapture maneuver.

Although absorption by the plasma is substantial in the CX and CIV regimes, we notice in Fig. 3.2 that much of the ionizing interaction occurs outside the control volume, where

ions are not trapped. This produces significant deflected flow as these new ions are turned away by the field. A force is imparted by this deflection resulting from the interaction of the applied magnetic field with the diamagnetic current produced by newly formed ions [43]. Recall that the magnetic field induced by this current does not significantly alter the applied field provided that the dipole magnetic pressure dominates freestream dynamic pressure.

In Chapter 2, we presented a single-particle modeling approach to derive the total drag F_D on the dipole as a function of ζ_s^* and ρ_L. This force is plotted in Fig. 3.9(a) using the functional approximation, Eq. (2.27), for three cases of n_∞. We observe a sharp jump in F_D when the plasma transitions from the I to CX regime, reaching hundreds of N at moderate field strengths for $n_\infty = 10^{18}$ m^{-3}. To contextualize these results, we compare the drag on a dipole plasma to that of a rigid body by examining the normalized drag, $\hat{F}_D$ [Eq. (2.23)]. Recall that this is a measure of momentum transfer to the plasma compared to the force expected on a generic magnet-sized body under the same flow conditions. Fig. 3.9(b) shows that before the CX regime, the force imparted on the plasma is weak ($\hat{F}_D < 1$). Transitioning to the CX regime yields significant enhancement to the momentum transferred from flow to magnet. The drag can be tens of times larger than that on a rigid body immersed in this flow. It is notable that the general shape of Fig. 3.9(b) is consistent with that predicted theoretically by Little and Kelly [34].

3.6 Context of Results

Our analysis reveals that critical ionization occurrs as a result of global interaction between a neutral flow and dipole plasma, leading to an order-of-magnitude increase in flow absorption by the plasma. This analysis differs from most CIV models which typically use one spatial dimension and are limited to describing the plasma/flow interaction locally (or assuming infinite extent). The CIV phenomenon is usually described for a plasma flowing relative to a stationary neutral gas and magnetic field (a notable exception is the model of McKenzie and Varma [50], although they explicitly omit consideration of the mechanism for energy transfer to the electrons). Prevailing theory states that the counterstreaming plasma induces turbulent heating of the electrons that drives ionization of the gas [31]. In this model, we instead describe a confined plasma considering only collisional energy transfer between

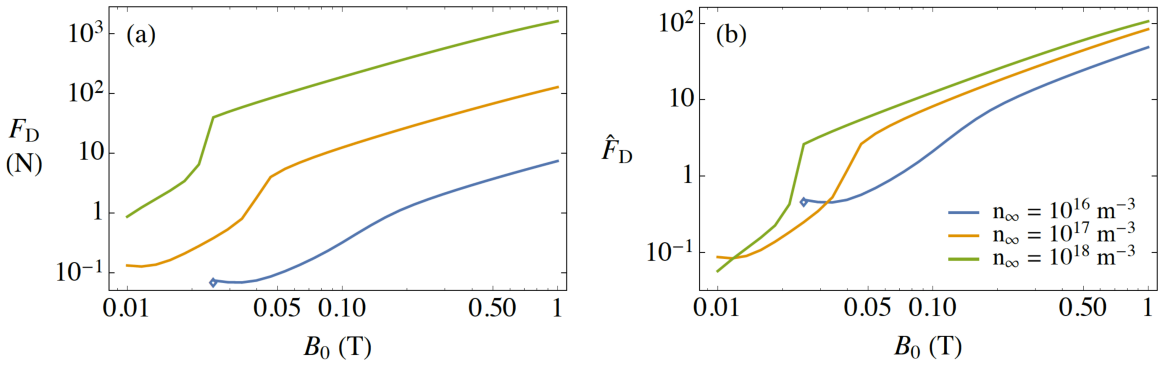

Figure 3.9: (a) Drag force, F_D, and (b) normalized drag force, $\hat{F}_D$, on the magnet are modulated by the applied field strength, B_0. The fixed conditions are $u_\infty = 12$ km/s, $r_c = 1$ m, and $\Gamma^{\text{inj}} = 5$ mg/s. The model solution is intractable at $n_\infty = 10^{16}$ m^{-3} for $B_0 < 25$ mT, implying the dipole is unsustainable below this field strength for the low density case.

species. Furthermore, the plasma is stationary with respect to the magnetic field rather than impinging as a beam. Our observation of critical ionization even after changing the classical assumptions adds to the wealth of evidence in literature for the ubiquity of the CIV phenomenon.

This model supports the effects anticipated by the theory of Little and Kelly [34]. We observe that changing the velocity, density, and magnetic field strength has significant impact on the mode of interaction as mapped in Fig. 3.7(b). These results are a direct consequence of including diffusion as a primary loss mechanism. For example, the I-CX threshold velocity is reduced as B_0 is increased because electron energy is confined longer and therefore less flow heating of electrons is required to sustain the plasma. The effect of diffusion on critical ionization in a closed field geometry is profound, but it remains uncharacterized in the literature. One exception is an early analysis of homopolar device experiments by Lehnert [51], but he uses parallel diffusive loss to argue that thermal electron-impact ionization could not account for observed CIV effects. As we have shown, this argument does not necessarily hold when plasma is confined along the field lines and instead diffuses perpendicularly. Our study is the first comprehensive investigation of critical ionization physics for such a closed-field geometry where perpendicular diffusion dominates the particle and

energy balance.

Möbius et al. [33] previously discussed the effects of various energy transfer processes on the interaction of a plasma beam with a neutral gas. Notably, a threshold velocity was derived that implied critical ionization could initiate below u_{cr} provided that the CX reaction rate dominates ionization. They concluded that CX can thus be a "triggering process" for critical ionization because it adds energy to the plasma beam without an associated depletion of tail electron energy. McNeil et al. [32] similarly identified the importance of CX to enabling critical ionization when electron energy is scarce. The CX regime presented here is distinct from these observations, however, because it is not an enhancement to CIV; it exhibits characteristically different physics. Specifically, in the CX regime, the neutral reservoir feeding critical ionization is not the flow but rather the secondary neutrals arising from the ion population. Charge exchange thus acts as the primary source of both neutrals and the energy to ionize them, a unique distinction from present theory.

No well-characterized experimental observation of this CX regime transition exists in literature. This is likely due to open field geometries that do not confine electron energy well. In traditional CIV experiments, heating of the electrons to $\sim$100 eV is observed [52], which is necessary to achieve ionization times faster than the rapid loss timescale. At these energies, flow ionization is so efficient that the CX regime would collapse and the observed transition would be from I to CIV, as indicated by Fig. 9(b) of Little and Kelly [34]. However, some anomalous experimental results are potentially explained by collisional effects. For example, Himmel et al. [53] observed three regimes in their rotating plasma investigation of critical ionization, with threshold velocities below u_{cr} measured at very high background pressures. They made no explicit connection to collisional heating, but Machida and Goertz [29] briefly theorized that the observation could be explained by an electron energy balance between resistive heating and effective ionization losses, which is consistent with our results. However, we note that the neutral densities in these experiments ($n_\infty > 10^{22}$ m^{-3}) are well outside the free molecular neutral flow regime assumed by our model ($n_\infty \lesssim 10^{19}$ m^{-3}). Venkataramani and Mattoo [54] also found that plasma deceleration through a neutral gas cloud was far more rapid than could be explained by ionization alone. The authors postulated that resonant charge exchange could explain the enhanced momentum loss at

higher neutral densities. This seems to agree with Machida and Goertz' simulation study [29], which predicted that resistive processes should dominate collective ones at high neutral densities. Indeed, in our study, we observe starker critical ionization thresholds to the CX regime as density is increased (see Fig. 3.8, for example). The species, velocities, densities, and field strengths in Venkataramani's experiment are remarkably similar to the parameters used in this chapter. Their conclusions may serve as a useful backdrop for laboratory investigations of the CX regime transition, but ultimately novel experimentation is needed to clarify and validate the physical regimes identified here. A preliminary experimental investigation is detailed in Chapter 5.

Brenning and Axnäs [55] have discussed some of the "unsolved problems" in CIV theory. One in particular is the effect of magnetic field strength on the interaction. They indicated there is evidence the flow must be subalfvénic ($u_\infty < v_A$) in order for turbulent heating not to be damped, imposing a lower bound on the magnetic field strength depending on neutral density. We have shown a lower bound on magnetic field arising even when only collisional heating is allowed. This suggests the link between critical ionization and field strength may be nonspecific to turbulent heating while still being consistent with experimental observations. Similarly, they described two distinct regimes within the collective-heating models that depend on neutral density. We show here this distinction exists with collisional heating as well, suggesting an underlying mechanism agnostic to the energy transfer channel.

Future work is required to expand the physical fidelity and complexity of this model. The density profile in Eq. (2.46), which is supported by theory [39, 56], was primarily adopted to simplify the model formulation. However, it may be modified to more closely represent realistic dipole plasmas. Pressure profiles are known [41] to depend on plasma beta and, in the laboratory, on anisotropy, finite coil effects, and plasma currents [40], which are all neglected in the model. Even the presence of a mechanical support, which will be required in an experimental validation of dipole/flow interaction, modifies the density scaling with ψ considerably [40]. An additional simplification is the assumption that secondary neutrals share the same density profile as the plasma. In a real system, they are more likely to exist at the interaction front since they result from CX with the stream. Fig. 3.2 demonstrates that the plasma density is a reasonable geometric proxy for the interaction region and therefore

secondary neutral production. Future higher fidelity simulations must examine the steady state $\hat{n}_{2n}$ accounting for spatially accurate neutral production and depletion. We reiterate that the general results found here are insensitive to a change in the assumed density profile, as evidenced by similar previous results using a different density scheme [21, 49]. Further model development is required to represent atmospheric species of interest for aerocapture missions, such as CO_2, H_2, or N_2, involving considerably more conservation equations of greater intricacy.

Finally, we note the importance of the model results for application to plasma aerocapture technology. Fig. 3.8 indicates that in order to sustain a critical ionization discharge in the dipole, tens of kW of plasma heating is required. Artificially supporting this discharge from a spacecraft-based power source would negate the mass savings that motivate the use of aerocapture. Therefore, these results provide bounds on the magnet design and atmospheric flight trajectory for a mission using plasma aerocapture. The demands of aerocapture can be extreme; drag forces on the order of 100 kN are needed to decelerate massive spacecraft by several km/s in a few minutes. A systems analysis of plasma aerocapture [49] shows that at the outer planets, without excessive onboard fuel and power, this may only be achieved by utilizing the flow-sustained regimes (CX and CIV). Additionally, the variation of drag force with magnetic field strength shown in Fig. 3.9 implies the capability for continuously-variable drag modulation, an aerocapture flight control scheme that dramatically improves accuracy and reduces risk [9]. This would be a significant technological leap for aerocapture concepts as modern proposed devices have no mechanism for this type of drag modulation.

3.7 Conclusion

Chapters 2 and 3 detail an analytical model of the global interaction between a rarefied, hypersonic neutral flow and magnetic dipole plasma. By simulating over a large parameter range, the global model reveals three distinct physical regimes governed by injection (I), charge exchange (CX), and ionization (CIV). These regimes, discussed in Section 3.3, are equivalent to those derived theoretically by Little and Kelly [34]. While the theory treated various timescales and reaction rates as independent parameters, the present analysis demonstrates the existence of the two critical ionization thresholds (I-CX and CX-CIV)

even when accounting for nonlinearly coupled physics. Notably, this global model has not invoked plasma instabilities or other collective electron heating processes; instead, we demonstrate that critical ionization is not only possible with but enhanced by charge exchange and Coulomb collisions. As anticipated by theory, the threshold velocity for the I-CX regime transition can be considerably lower than u_{cr} while the CX-CIV transition is necessarily higher. These thresholds induce a significant enhancement of the global interaction between the plasma and stream. Substantial flow mass and energy are deposited to naturally sustain the plasma discharge while large forces are coupled to the magnetic field.

The use of a global model in the investigation of a hypersonic flow interacting with magnetized plasma offers certain advantages. Numerical studies of confined plasmas are usually computationally intensive and thus must be constrained to very specific parameters for their application. In the model derived here, geometric assumptions allow us to numerically solve a large system in a few seconds. This enables its use for a broad array of simulation conditions as seen in this study. The species interactions are input from experimental data or functional approximations thereof, allowing for the addition of far more species and reactions so long as the limiting assumptions are not violated. These features of the model make it applicable to many types of investigations, such as validation of experimentally observed plasma/neutral interactions, simulation of space plasmas, or performance scaling of plasma aerocapture and propulsion concepts. In Chapter 4, we will leverage this versatility as well as the insights gained from Chapters 2 and 3 to design and analyze preliminary plasma aerocapture mission concepts.

Chapter 4

PLASMA AEROCAPTURE MISSION DESIGN

Chapters 2 and 3 provided valuable insight into the physics of magnetoshell operation. In particular, we found that leveraging flow sustainment of the plasma offers massive performance benefits that are technology-enabling. In this chapter, we investigate how to design DMPA missions to take advantage of this newfound physical understanding. We first review some results of modeling pertaining to magnetoshell performance in a hydrogen environment relevant to ice and gas giant atmospheres. We then present a general framework of magnetoshell systems design that informs the basic elements of a DMPA mission concept. Performance sensitivities are addressed using a custom trajectory tool that incorporates magnetoshell drag physics and magnetic field control. We demonstrate the use of this code for a reference DMPA mission design at Neptune. The solver is then used in a Monte Carlo simulation to determine the performance sensitivity of DMPA to realistic dispersions in vehicle entry state and Neptunian atmospheric conditions. Finally, these results are compared with similar sensitivity studies of aeroshell technologies to determine the benefits of DMPA and the areas where technology development is needed.

4.1 Hydrogen Plasma Model

For the analysis in this chapter, we generate performance results using the global model derived in Chapter 2. Currently, the global model describes alike atomic particle interactions to simplify the highly complex molecular plasma chemistry present in a real DMPA setting. To approximate the atmospheres of the outer planets, we assume an atomic hydrogen flow and plasma and include an energy loss term to account for dissociation of H_2 and other loss mechanisms that may affect performance. Future work will incorporate full H_2 plasma chemistry to derive more exact performance scaling; for now, the present results are sufficient for a first-order analysis.

While the model is fundamentally unchanged, new data and functions are required to describe hydrogen interaction processes instead of argon. The momentum transfer cross section of H–H^+ collisions is $\sigma_{Q_m} = 6 \times 10^{-19}$ m^2, given by Brennan [57]. Energy-dependent charge exchange cross sections for H–H^+ are given by Barnett [58]. The momentum transfer cross section for e^-–H collisions is given by Banks [59] as 1.5×10^{-20} m^2. The ionization reaction rate coefficient is given in functional form by Voronov [60] as

$$R_{\text{iz}}(T_e) = 2.91 \times 10^{-8} \frac{1}{.232 + U_{\text{iz}}/T_e} \left(\frac{U_{\text{iz}}}{T_e}\right)^{0.39} \exp\left[-\frac{U_{\text{iz}}}{T_e}\right] \tag{4.1}$$

where R_{iz} is in m^3/s. The effective ionization cost including scattering and excitation losses, ϵ_{ion}, is given by a functional fit determined by Little [61] to data from Dugan and Sovie [62],

$$\begin{aligned} \epsilon_{\text{ion}}/U_{\text{iz}} &= \left(246.7 \exp\left[\frac{-13.6 U_{\text{ex}}}{U_{\text{iz}}}\right] + 0.4\right) \exp\left[\left(-\frac{1.9 U_{\text{ex}}}{U_{\text{iz}}} + 1.8\right) \frac{U_{\text{iz}}}{T_e}\right] \\ &\quad - \frac{4.3 U_{\text{ex}}}{U_{\text{iz}}} + 4.7 \ , \end{aligned} \tag{4.2}$$

where U_{ex} is the first excitation energy of H. For every H particle interacting with the plasma we incur a loss from the electron population equal to half the dissociation energy of H_2, $\epsilon_{\text{diss}} = 4.5$ eV, to provide a first-order approximation for molecular effects.

The DMPA system design is strongly driven by the magnetoshell performance scaling, which depends on the results of the analytical plasma model. While the performance scaling is not anticipated to change drastically with the development of a molecular chemistry model, we briefly describe here how we extrapolate results of atomic modeling to the Neptunian atmosphere (or any other predominantly H_2 atmosphere). Assuming that the H atoms impacting the magnetoshell result from electron dissociation of H_2 in the flow, the number density of H, n_∞, is correlated to the mass density of the local atmosphere ρ_{atm} by

$$n_\infty = 2 f_{\text{H}_2} \frac{\rho_{\text{atm}}}{\overline{M}_{\text{atm}} m_p} \tag{4.3}$$

where f_{H_2} is the fraction of H_2 by volume, $\overline{M}_{\text{atm}}$ is the mean molecular weight of the atmosphere, and m_p is the proton mass. This is a broad simplification that neglects plasma chemistry, other significant species (such as He which has $f_{\text{He}} = 0.19$ at Neptune), and

the dependence of composition on altitude. Ultimately, the DMPA design scaling will take these into account with a comprehensive plasma simulation and the use of planetary -GRAM models for accurate representation of the freestream flow.

4.2 Performance Scaling for Outer Planets

In Chapter 3 we discovered a velocity threshold below which the performance of magnetoshells is insufficient for plasma aerocapture. A systems analysis found that this threshold poses significant challenges to the use of DMPA in low-velocity entry conditions such as those typical of Venus, Earth, Mars, and Titan aerocapture [49]. Instead, the performance scaling indicates that magnetoshells serve to enable high-velocity entries at the outer planets Jupiter, Saturn, Uranus, and Neptune. Here we discuss the implications of global modeling in that context.

4.2.1 Hydrogen Magnetoshell Physics

Recall the parameter ζ^* [Eq. (3.2)] that describes the rate of magnetoshell interaction with incident atmospheric gas compared with the particle rate of transit across the magnet. Fig. 4.1 shows the dependence of ζ^* on u_∞ for four different cases of seed plasma injected power P_{inj}. As before, we observe a sharp transition between injection-sustained and flow-sustained regimes as a function of u_∞. However, in a hydrogen flow, the threshold velocity is significantly higher than for argon owing to its small mass [Eq. (3.1)]; for the conditions shown in Fig. 4.1, the spacecraft must exceed 25 km/s to leverage flow sustainment. In Fig. 4.2 we plot the rate of mass and energy absorption by the plasma ($\dot{m}_{\text{cap}}$ and P_{cap}, respectively) as a function of magnetic field strength for several freestream densities. Compared to Fig. 3.8, the magnetoshell absorbs nearly ten times more power from the flow, largely due to the extreme velocity associated with outer planet aerocapture.

4.2.2 Magnetic Field Drag Modulation

A distinguishing feature of aerocapture is the high drag force required to achieve several km/s of Δv in just a few minutes. In contrast to aeroshells, magnetoshells have no physical

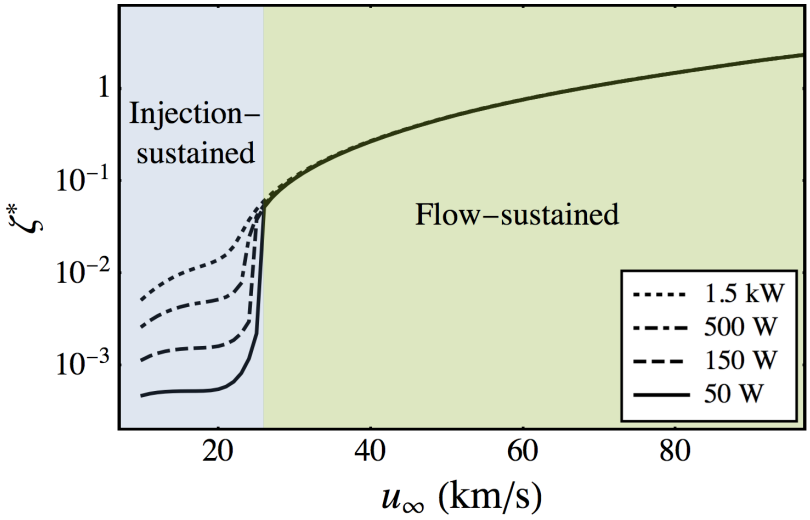

Figure 4.1: The flow/magnetoshell interaction strength, ζ^*, increases significantly from the injection-sustained to the flow-sustained regime. Four increasing values of the artificially injected plasma power P_{inj} show how it modulates the interaction at low velocity but has negligible effect in the flow-sustained regime. The fixed conditions are $n_\infty = 10^{18}$ m^{-3}, $B_0 = 500$ G, and $r_c = 1$ m.

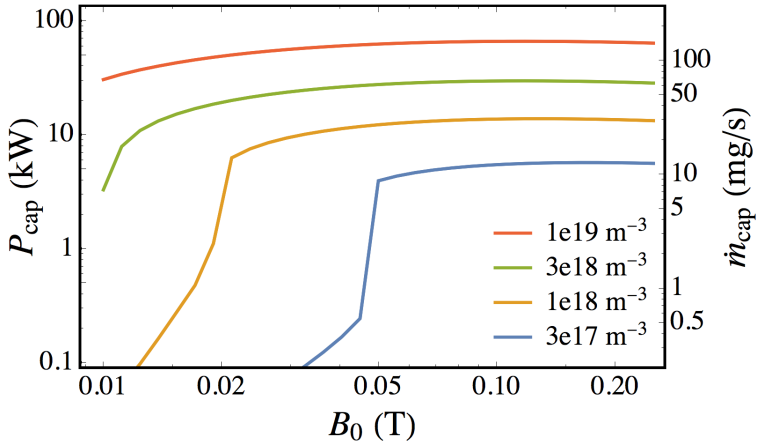

Figure 4.2: The rate of capture of flow energy (P_{cap}) and mass ($\dot{m}_{\text{cap}}$) by the magnetoshell increases significantly in the flow-sustained regime, indicated by the massive jumps as magnetic field strength B_0 is increased. Four freestream particle densities n_∞ are shown, with higher capture and wider flow-sustained regimes for increasing n_∞. The fixed conditions are $u_\infty = 30$ km/s, $r_c = 1$ m, and $P_{\text{inj}} = 50$ W.

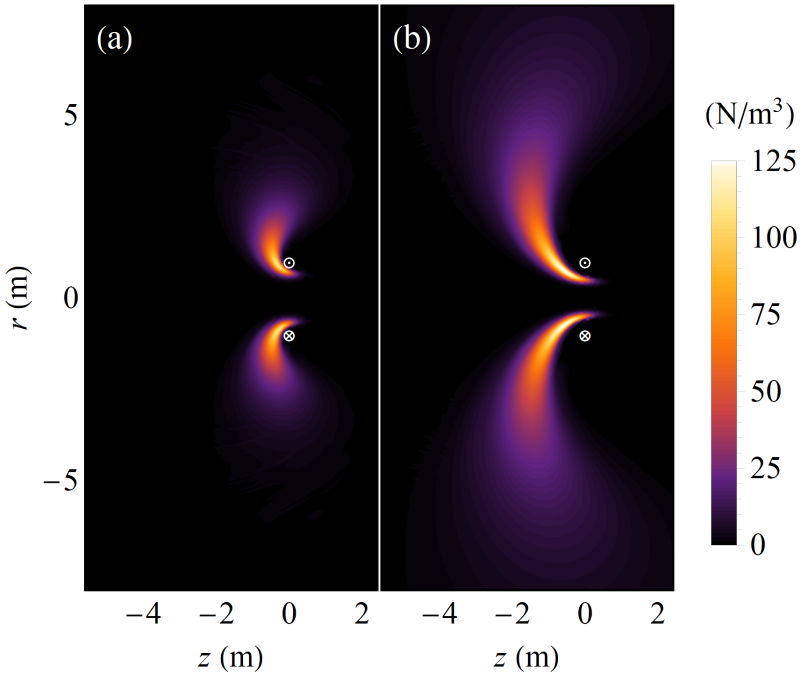

Figure 4.3: The magnetoshell drag per unit volume for (a) $B_0 = 0.2$ kG and (b) $B_0 = 2$ kG. The atmosphere flows along $+z$ at $u_\infty = 25$ km/s with a density of $1.25{\times}10^{-8}$ kg/m^3 of atomic hydrogen. The magnet is a circular loop of current of radius $r_c = 1$ m.

surface to generate aerodynamic drag, instead relying on magnetic capture and deflection of ionized atmospheric flow to impart momentum on the spacecraft. In Fig. 2.5, we saw how the effective drag surface scales with the dimensionless parameters ρ_L and ζ_{tot}. To gain a more application-focused intution, in Fig. 4.3 we show the distribution of the volumetric drag force for conditions relevant to aerocapture in an ice or gas giant atmosphere. The flow velocity is $u_\infty = 25$ km/s with a freestream mass density of $\rho_\infty = 1.25 \times 10^{-8}$ kg/m^3. This plot demonstrates the mechanism by which magnetoshells achieve continuously-variable drag modulation. All other conditions equal, only the magnetic field strength is increased from 0.2 kG in 4.3(a) to 2 kG in 4.3(b). We can see that the region of momentum transfer grows much larger as the field strength is increased, and indeed the total drag force increases from $F_D = 2.2$ kN to $F_D = 22.1$ kN. This behavior is leveraged during the aerocapture maneuver to modulate the drag force in response to local perturbations and uncertainties without any mechanical actuation.

Although the spatial extent of drag on the plasma is evidently large, the interaction is not discrete but rather gradually weakens radially away from the magnet. In order to more directly compare magnetoshell performance with aeroshells, we define an effective surface area

$$(C_{\mathrm{D}}A)_{\mathrm{eff}} = \frac{F_D}{\rho_\infty u_\infty^2/2} \tag{4.4}$$

where $\rho_\infty = m_{sn} n_\infty$ is the freestream mass density. Eq. (4.4) normalizes the magnetoshell drag by the freestream dynamic pressure; in this sense, $(C_{\mathrm{D}}A)_{\mathrm{eff}}$ represents the area of a solid body that would generate a drag force equivalent to that of the diffuse plasma. Fig. 4.4 shows this area in terms of a diameter, D_{eff} [where $(C_{\mathrm{D}}A)_{\mathrm{eff}} = \pi D_{\mathrm{eff}}^2/4$], as a function of ρ_∞ and B_0. At higher field strengths and densities, we observe an effective diameter on the order of 10–40 m, significantly larger than what is achieved by modern-day deployable aeroshells. A sharp performance drop is apparent in the lower left of the plot as a region of low D_{eff}; this is a result of the transition discussed in Chapter 3 out of the CX regime into the injection-sustained plasma regime.

Note in Fig. 4.4 that at a fixed ρ_∞ and u_∞, D_{eff} is a strong function of magnetic field strength. This phenomenon is crucial to DMPA. The freestream density and velocity are entirely functions of the spacecraft trajectory through the atmosphere; therefore, at any given point in the trajectory, $(C_{\mathrm{D}}A)_{\mathrm{eff}}$ can be modulated by an order of magnitude via the magnet. The vehicle ballistic coefficient, β, is defined for a spacecraft of mass m_{sc} as

$$\beta = \frac{m_{\mathrm{sc}}}{C_{\mathrm{D}}A} \ . \tag{4.5}$$

Trajectory studies indicate that the ratio of maximum to minimum β achieved by a drag-modulation decelerator is the strongest driver of final orbit accuracy [9]. Staged jettison aeroshells have typical β ratios of about 10. Because magnetoshells can be deactivated mid-maneuver without jettisoning mass, their β ratio is simply the effective plasma area over the aerocapture vehicle's nominal solid area $(C_{\mathrm{D}}A)_{\mathrm{sc}}$,

$$\frac{\beta_{\max}}{\beta_{\min}} = \frac{(C_{\mathrm{D}}A)_{\mathrm{eff}}}{(C_{\mathrm{D}}A)_{\mathrm{sc}}} \tag{4.6}$$

The large effective area and the ability to deactivate the magnetoshell can result in order-of-magnitude improvements to β ratio over aeroshell drag modulation. Combined with

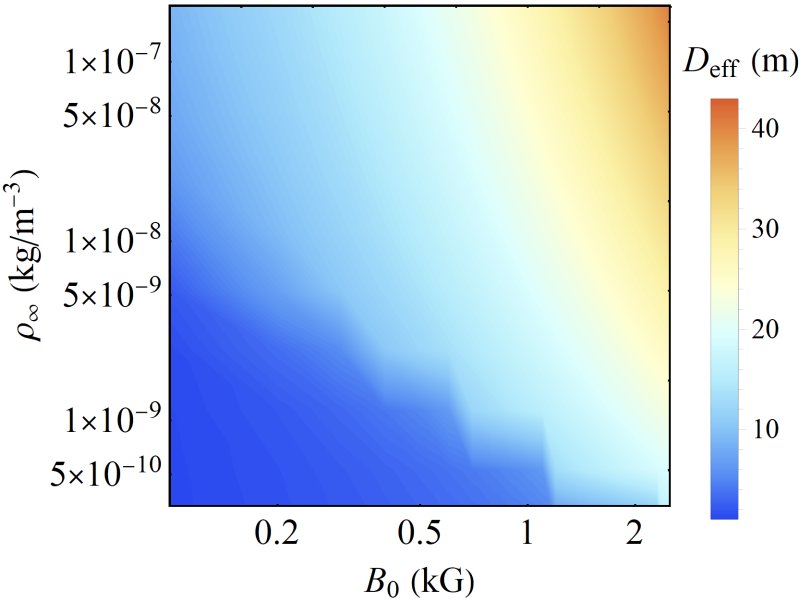

Figure 4.4: The effective drag surface diameter of the magnetoshell, D_{eff}, is a strong function of magnetic field strength and can reach tens of meters with only a 2 m-diameter magnet. The fixed conditions are $u_\infty = 25$ km/s and $r_c = 1$ m.

the potential to continuously modulate β through $(C_{\text{D}}A)_{\text{eff}}$, this represents a significant technological leap in drag-modulation aerocapture, the implications of which are examined in Section 4.5.

4.3 Guidance and Control

A custom orbit code is developed that takes plasma model results as inputs, enabling the application of magnetic field drag modulation control and analysis of its robustness to atmospheric and trajectory uncertainties. The equations of motion of a spacecraft through the atmosphere of an oblate, rotating planet are given by Lu [63] and modified to exclude

lift:

$$\dot{r} = v\sin\gamma \tag{4.7}$$

$$\dot{\theta} = \frac{v\cos\gamma\sin\psi}{r\cos\phi} \tag{4.8}$$

$$\dot{\phi} = \frac{v\cos\gamma\cos\psi}{r} \tag{4.9}$$

$$\dot{v} = -F_D - g_r\sin\gamma - g_\phi\cos\gamma\cos\psi + \Omega^2 r\cos\phi(\sin\gamma\cos\phi - \cos\gamma\sin\phi\cos\psi) \tag{4.10}$$

$$\dot{\gamma} = \frac{1}{v}\left[\left(\frac{v^2}{r} - g_r\right)\cos\gamma + g_\phi\sin\gamma\cos\psi + 2\Omega v\cos\phi\sin\psi + \Omega^2 r\cos\phi(\cos\gamma\cos\phi + \sin\gamma\cos\psi\sin\phi)\right] \tag{4.11}$$

$$\dot{\psi} = \frac{1}{v}\left[\frac{v^2}{r}\cos\gamma\sin\psi\tan\phi + g_\phi\frac{\sin\psi}{\cos\gamma} - 2\Omega v(\tan\gamma\cos\psi\cos\phi - \sin\phi) + \frac{\Omega^2 r}{\cos\gamma}\sin\psi\sin\phi\cos\phi\right] \tag{4.12}$$

where r is radial distance to the planet center, θ is longitude, ϕ is latitude, v is spacecraft velocity, γ is flight path angle, and ψ is heading angle (for a detailed derivation of these equations and conventions for these variables, see Chapter 3 of Vinh [64]). Note that Eqs. (4.7)–(4.12) give the spacecraft state in the planet-fixed frame. The atmosphere is assumed to have no wind and rotate with the planet at angular rate Ω. The oblateness of the planet is accounted for through the terms

$$g_r = \frac{\mu}{r^2}\left[1 + J_2\left(\frac{R_p}{r}\right)^2(1.5 - 4.5\sin^2\phi)\right] , \tag{4.13}$$

$$g_\phi = \frac{\mu}{r^2}\left[J_2\left(\frac{R_p}{r}\right)^2(3\sin\phi\cos\phi)\right] , \tag{4.14}$$

where μ is the planet's gravitational parameter, R_p is the planet radius, and J_2 is the second zonal harmonic coefficient of the planet.

Drag force F_D impacts the spacecraft trajectory through Eq. (4.10). To model magnetoshell drag, we use the standard aerodynamic drag equation,

$$F_D = q_\infty C_D A\,, \tag{4.15}$$

where $q_\infty = \rho_\infty v^2/2$ is the freestream dynamic pressure. Although the physics of magnetoshell drag are different from aerodynamic drag, a function or lookup table for the effective

area $(C_D A)_{\text{eff}}$ can be substituted into Eq. (4.15) for the trajectory solver. This table is generated for a range of relevant input conditions using the plasma model described in Section 2.4. Notably, $(C_D A)_{\text{eff}}$ is a function of B_0, ρ_∞, and u_∞. The latter two are prescribed by the spacecraft altitude and velocity so that the drag term in Eq. (4.10) can be modified by adjusting B_0.

To implement magnetic drag modulation in our simulation, we devise a control scheme to target a specific apoapsis radius upon atmospheric exit. First, an upper and lower bound on magnetic field are defined such that $B_0 \in [B^{\min}, B^{\max}]$ while the magnetoshell is active. The upper bound is constrained by the power system ability to generate the required current, while the lower bound is imposed by plasma physical constraints. The simulation begins at atmospheric entry, which we define as a maximum altitude, with B_0 initiated at some predefined value. An onboard density model, ρ_{est}, is used for trajectory estimation that is updated throughout the maneuver using the scheme described by Putnam and Braun [9]. The trajectory is estimated at each time step by propagating Eqs. (4.7)–(4.12) assuming B_0 is held constant up to atmospheric exit and the resulting apoapsis is computed. The change in magnetic field between time steps is proportional to the apoapsis error,

$$B_0(t + \Delta t) = B_0(t) \times \left(1 + K_B \frac{r_a^{\text{proj}} - r_a^{\text{targ}}}{r_a^{\text{targ}}} \right) , \tag{4.16}$$

where Δt is the simulation time increment, K_B is an arbitrary gain, r_a^{proj} is the projected apoapsis, and r_a^{targ} is the target apoapsis. Another trajectory is computed using the ballistic area of the vehicle (i.e. assuming the magnetoshell is turned off); if the resulting apoapsis is within a specified error tolerance, B_0 is set to 0 and is only turned back on at a later time step if the apoapsis error exceeds tolerance. At each time step, a truth trajectory is computed using the actual density profile, ρ. It is assumed the spacecraft has knowledge of its current truth state as initial conditions for the trajectory estimation at each time step.

4.4 Mission Design Considerations

The magnetoshell enabling DMPA is a novel technology with little prior hardware development. Here, we lay out an initial framework that can be used to obtain first-order design scaling of a magnetoshell meeting the needs of a given mission. This framework takes into

account notional mission parameters such as entry velocity and Δv; spacecraft limitations such as size, weight, power, and TPS; and magnetoshell performance parameters such as drag force and controllability. It is intended to be a "first pass" to generate a mission design that roughly closes before moving on to a more thorough analysis of hardware requirements and drag modulation trajectories.

4.4.1 Mission Architecture

An overview of the mission profile for DMPA is shown in Fig. 1.2. Although significant technological advancement is required to implement DMPA, we aim to leverage contemporary state-of-the-art wherever possible to limit bottlenecks imposed by more advanced concepts. Therefore, we restrict the design architecture in the following ways. Large magnets (meters-scale) with high field strengths ($\sim$kG) are required to generate sufficient drag for successful aerocapture. A standard electromagnet of aluminum or copper wire is proposed for the magnetoshell. Superconducting magnets can reach these high field strengths, but their implementation in space systems requires significant technological breakthroughs; permanent magnets offer simplicity, but stacking them to achieve the required field strength is mass-prohibitive. While feasible to construct, the electromagnet approach places a high demand on power (ten to hundreds of kW) that cannot be delivered by solar arrays or near-future generators. Instead, a high-energy battery bank is kept charged during cruise and discharged as a power source during the maneuver. A power processing unit (PPU) will be utilized similar to those used in modern electric propulsion spacecraft. Finally, TPS mass is estimated as a fraction of the system mass based on heritage designs. For the purposes of design scaling, we assume these elements (electromagnet, batteries, PPU, and TPS) mainly comprise the architecture and impose the biggest constraints on mass, size, and technology development.

4.4.2 DMPA Design Scaling

The goal of this framework is to produce a first order magnetoshell design that (1) has the desired performance for the given destination and (2) closes with modern technology

constraints. A fundamental determinant of performance needs for an interplanetary orbiter is the Δv of the insertion maneuver. We roughly estimate the average drag force necessary for a given DMPA maneuver, $F_{D,\text{avg}}$, as

$$F_{D,\text{avg}} = \frac{m_{\text{sc}}\Delta v}{\Delta t_{\text{atm}}} \tag{4.17}$$

where Δt_{atm} is the time spent in the sensible atmosphere. The mass of the vehicle delivered to the target pre-maneuver (m_{sc}) is largely a function of the launch vehicle and trajectory design, whereas Δt_{atm} depends on the destination and can be estimated based on existing aerocapture simulations. The magnetoshell must be designed to the maximum drag force that will be required during the maneuver, which we estimate as $F_{D,\text{max}} \approx 3F_{D,\text{avg}}$. The analytical model can then be used to determine combinations of input conditions that can produce this drag, forming the magnetoshell design space.

Any number of different magnet designs may be able to attain $F_{D,\text{max}}$. However, the design must not only meet the performance goal but also be optimized for diameter, power, mass, and overheating avoidance. The magnet consists of wire wound circularly with N total turns. A magnet of average radius r_c produces a magnetic field at its center of

$$B_0 = \frac{\mu_0 N I}{2r_c} \tag{4.18}$$

where I is the applied current through the wire. The power P_m required to drive the magnet current is ohmic, i.e. $P_m = I^2 R$. The current I and total resistance R can be tuned by adjusting the wire gauge/material and parallelizing multiple loops. However, our design space is driven from simulations dictating r_c and B_0 and mission constraints dictating the mass. We therefore wish to cast the power requirement in terms of these parameters.

The mass of the magnet coil, m_c, is given by

$$m_c = l_w A_w \rho_w \tag{4.19}$$

where l_w is the overall wire length, A_w is the wire cross-sectional area (i.e. gauge selection), and ρ_w is the mass density of the wire (i.e. material selection). The total resistance of the winding is

$$R = \frac{l_w}{A_w \sigma_w} \tag{4.20}$$

where σ_w is the wire conductivity. Assuming r_c is the average coil radius regardless of its overall thickness, the wire length is given by

$$l_w = 2\pi r_c N \ . \tag{4.21}$$

Finally, Eqs. (4.18)–(4.21) are combined to give the magnet power,

$$P_m = I^2 R = \left(\frac{4\pi}{\mu_0}\right)^2 \frac{B_0^2 r_c^4 \rho_w}{m_c \sigma_w} \ . \tag{4.22}$$

Note this equation couples several magnet design parameters (power, size, strength, mass, and material selection) while being agnostic to the electrical design (current, voltage, series-parallel configuration). Crucially, this enables straighforward design optimization of the basic mission architecture described in Section 3.1.

The power requirement given by Eq. (4.22) subsequently drives the battery and PPU designs. For this first-order design, we are primarily concerned with the mass and volume of these elements to ensure they can reasonably fly aboard the aerocapture vehicle. We compute the battery energy storage requirement assuming the maximum power P_m is applied for the full duration of Δt_{atm} and applying a 2x margin. For gravimetric and volumetric battery energy densities $\alpha_{b,g}$ and $\alpha_{b,V}$, respectively, the battery mass and volume are estimated as

$$m_b = 2\alpha_{b,g} P_m \Delta t_{\text{atm}} \ , \tag{4.23}$$

$$V_b = 2\alpha_{b,V} P_m \Delta t_{\text{atm}} \ . \tag{4.24}$$

Similarly, the PPU mass m_{ppu} is a function of the max power requirement. Assuming a specific mass of α_{ppu}, we have

$$m_{\text{ppu}} = \alpha_{\text{ppu}} P_m \ . \tag{4.25}$$

The final check is to ensure ohmic dissipation will not internally overheat the magnet. We estimate the magnet heating rate $\dot{T}_m$ as

$$\dot{T}_m = \frac{P_m}{m_c c_p} \tag{4.26}$$

where c_p is the heat capacity of the wire material. With P_m a function of B_0, r_c, and m_c, the magnetoshell system is easily optimized for the minimum total mass m_{tot} satisfying the

design requirements. We estimate this as the sum of the three main elements,

$$m_{\text{tot}} = 1.5(m_c + m_b + m_{\text{ppu}}), \tag{4.27}$$

where a 50% margin is applied to conservatively account for the structural mass associated with the magnetoshell system.

To see how the above framework enables optimized design considerations, we examine different magnetoshell configurations that have identical discharge power requirements, $P_m = 100$ kW, and coil masses, $m_c = 1200$ kg. Assuming aluminum wire ($\rho_w = 2700$ kg/m^3, $\sigma_w = 3.77 \times 10^7$ S/m), Eq. (4.22) dictates a locus of magnet diameters $d_c = 2r_c$ and strengths B_0 satisfying the power and mass constraints. In Fig. 4.5, we show $(C_{\text{D}}A)_{\text{eff}}$ as a function of flow velocity and density (mapped to Neptune altitude) for four such magnet configurations. We observe that, for equal power and coil mass, larger diameter magnets with weaker fields are capable of significantly higher effective drag area than small magnets with strong fields. Recall that higher β ratio yields better orbit targeting accuracy and that the denominator in Eq. (4.6) is fixed. Thus, Fig. 4.5 clearly demonstrates this design should be optimized for maximum magnet size. The freestream density n_∞ is correlated to an altitude at Neptune using Eq. (4.3) and the Neptune-GRAM-derived density profile given by the open-source Aerocapture Mission Analysis Tool (AMAT) [65]. These plots therefore represent a "flight envelope" performance map for Neptunian DMPA for these specific magnetoshell designs. We see the transition to the flow-sustained regime clearly defines the region of applicability to $u_\infty > 15$ km/s at the least, a threshold that increases with altitude. This again highlights that the impact of the critical ionization physics discussed in Section 2.2 is to restrict DMPA to high-velocity applications, motivating the consideration of outer planet missions.

4.4.3 Example Mission Design

Using the design framework presented in the previous section, we can generate preliminary DMPA mission designs for given sets of constraints. Here we use a Neptune orbiter mission concept developed by JPL and NASA Ames [7, 66] as a reference point for constraints and comparison. This drag-modulation aerocapture (DMA) mission would deliver an aerocap-

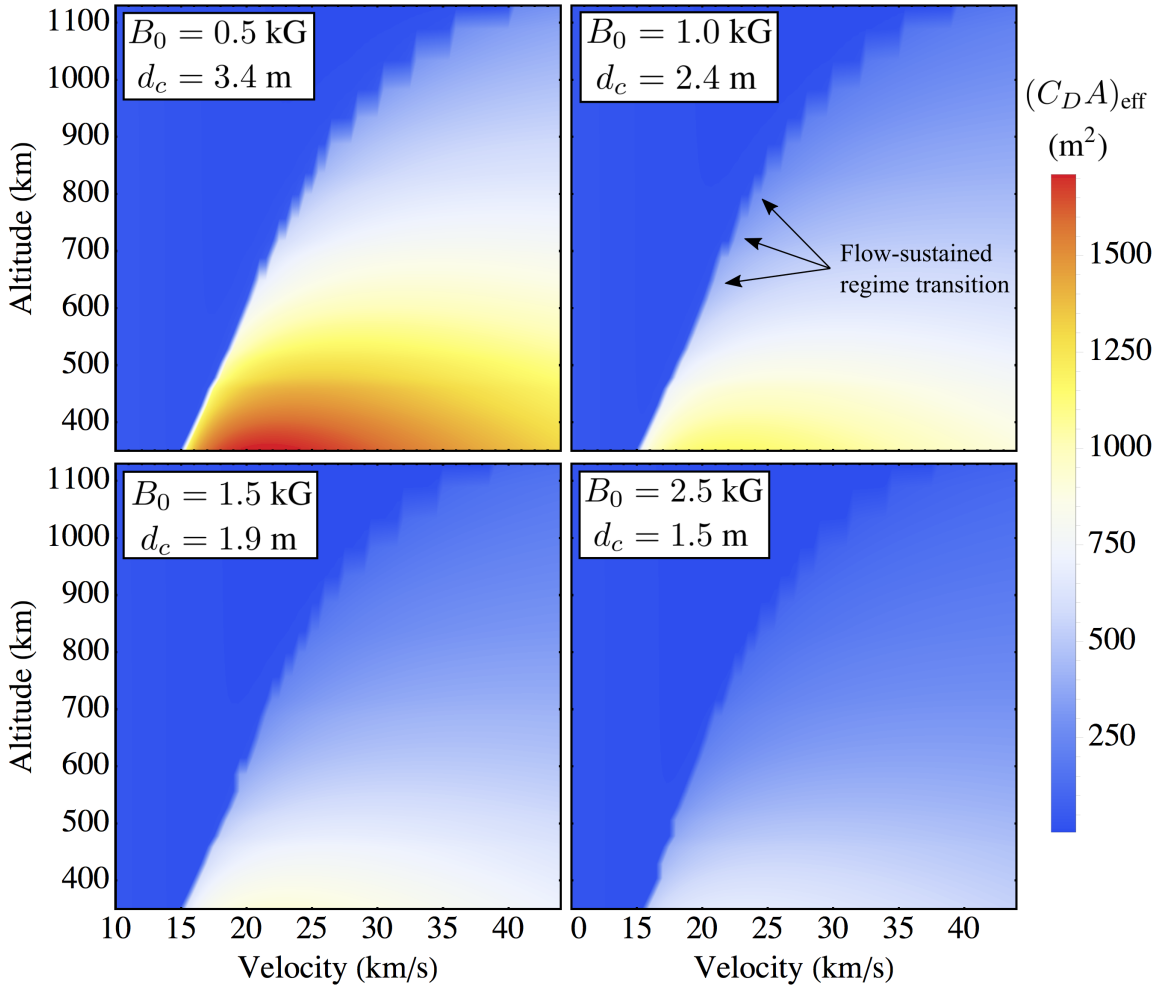

Figure 4.5: Maximum effective drag area, $(C_{\mathrm{D}}A)_{\mathrm{eff}}$, in Neptune's atmosphere for four magnet strengths (B_0) and diameters (d_c). The magnet mass, $m_c = 1200$ kg, and magnet power, $P_m = 100$ kW, are equal for all four cases, highlighting the incentive to maximize d_c. $(C_{\mathrm{D}}A)_{\mathrm{eff}}$ can be over 1500 m^2, providing a high degree of β control. The flow-sustained threshold demonstrates a clear lower bound on spacecraft velocity defining the Neptune flight envelope.

ture vehicle with mass $m_{\mathrm{sc}} = 5{,}725$ kg to the atmospheric interface at Neptune. The vehicle consists of a 4 m-diameter capsule with an attached 12 m-diameter ADEPT drag skirt that is jettisoned during the maneuver in a single-event drag modulation scheme. The skirt stows during launch concentrically around the rear of the capsule to fit within a 5 m fairing. The ADEPT skirt has a mass of 3,145 kg with an additional 1,100 kg of heat shielding on

the capsule so that the final payload mass delivered to orbit is 1,480 kg [7]. One of the significant advantages of the mission is the potential to reduce trip time to Neptune from 12-13 years using an all-propulsive architecture to 9 years using aerocapture.

In order to compare DMPA design and performance with the ADEPT concept, we first select some representative mission constraints given by [7]. The entry velocity is 25 km/s with respect to the atmosphere, the time spent in the sensible atmosphere is $\Delta t_{\text{atm}} = 350$ s, and the required Δv is about 5.5 km/s. From this we estimate a drag force requirement of $F_{D,\max} \approx 270$ kN as a design point for magnetoshell performance. Recall from Fig. 4.5 that effective drag area scales most strongly with r_c; therefore we set $r_c = 2$ m to make full use of the payload volume. The ADEPT vehicle experiences a peak stagnation heat flux of about 170 W/cm^2, which we use as an upper constraint for the DMPA trajectory design. With a nose radius $R_n = 1$ m and assuming the max stagnation heating occurs about halfway through the maneuver ($u_\infty \approx 22.25$ km/s), we find the maximum allowable atmospheric density $n_{\infty,\max} \approx 10^{21}$ m^{-3} from the Sutton-Graves heating equation [67]. In practice, this sets a minimum periapsis altitude. We have therefore constrained the value of three parameters at the design point (r_c, u_∞, and n_∞) that are all inputs to the analytical plasma model presented in Section 2.4.

The next step is to run simulations of the magnetoshell/flow interaction with these fixed inputs and an array of magnetic field strengths, B_0. From the model results, we determine a requirement on B_0 of 50 G to achieve the drag force $F_{D,\max}$ at the design point. Recall from the previous section that our magnetoshell design space consists of m_c, r_c, and B_0, the latter two of which have been prescribed. We now optimize for minimum total system mass m_{tot} via the coupled Eqs. (4.22), (4.23), (4.25), and (4.27). We assume aluminum wire is used for the magnet winding; the battery energy density is that of modern Li-ion cells, $\alpha_{b,g} = 250$ Wh/kg [68]; and the PPU specific mass scales as a modern electric propulsion unit, $\alpha_{\text{ppu}} = 6$ kg/kW [69]. The minimum total mass is $m_{\text{tot}} = 430$ kg with a coil mass of $m_c = 142$ kg and a discharge power of $P_m = 21$ kW. The ohmic heating rate from Eq. (4.26) is $\dot{T}_m \approx 10$ °C/min, posing no risk of internally overheating the magnet within the short maneuver duration.

Contrasted with the ADEPT system mass of 3,145 kg, this result suggests an over-

whelming improvement in final orbiter mass by using a 4 m-diameter, 50 G magnetoshell. However, this magnetic field is very weak; recall that the flow-sustained regime collapses below a certain field strength, and 50 G is near the edge of validity for the plasma model itself. At a max B_0 of 50 G, there is also only a small range to vary the field for continuous drag modulation. One mitigation is to simply increase the system power, as there is plenty of mass margin to enhance this design. However, we can also assess the use of magnetoshells to ease other challenging constraints. For instance, we used 170 W/cm^2 as a constraint on stagnation heating, but the large effective diameter suits magnetoshells for use higher in the atmosphere to reduce heat load to the spacecraft. Restricting the design to $B_0 > 200$ G, we find the system mass is minimized for a design point stagnation heating of 120 W/cm^2. The system design and performance parameters for this case are given in Table 4.1. We assume the magnetoshell vehicle requires the same TPS mass as the ADEPT vehicle, though in practice it may be less due to the reduced heat load [70].

A performance map of the magnetoshell design described in Table 4.1 is shown in Fig. 4.6. Here we plot the minimum ballistic coefficient β_{min} achieved by the magnetoshell [corresponding to its maximum $(C_{\text{D}}A)_{\text{eff}}$]. We also plot a DMPA trajectory that is propagated using the trajectory solver detailed in Section 4.3. The magnetoshell is deactivated near the end of the atmospheric pass and the spacecraft exits with an apoapsis of 340,000 km. We note that there is no modulation in this case; the magnet is maintained at the max field strength of 250 G (although in Section 4.5 we will implement continuous drag modulation). In addition to the reduced heat flux, we observe the dynamic pressure is reduced by an order of magnitude by flying at a higher altitude; ADEPT has a peak around 3 kPa while the periapsis of the magnetoshell trajectory reaches about 300 Pa. Along the entire trajectory the magnetoshell can achieve single-digit β_{min} values, with a best of $\beta_{\text{min}} = 4$. The magnetoshell can be powered off without jettisoning it, so the maximum β is higher ($\beta_{\text{max}} \approx 270$ kg/m^2) than that for the ADEPT case (121 kg/m^2), which necessarily loses vehicle mass in the modulation event. Thus, this DMPA architecture can achieve an unprecedented β ratio of 67. We reiterate that not only is there a large ratio of highest to lowest ballistic coefficients, it is also continuously controllable between these two extremes.

While we chose to design to an existing mission concept in this example, there are myriad

Table 4.1: System design comparison between the Neptune DMA mission architecture using an ADEPT drag skirt and a magnetoshell. ADEPT values are taken directly (or calculated) from [7]. Magnetoshell values are calculated for the trajectory shown in Fig. 4.6.

Neptune DMA system	*w/ ADEPT*	*w/ Magnetoshell*
Modulation scheme	Single-stage	Continuous
A/C system mass	3145 kg	2130 kg
TPS mass	1100 kg	1100 kg
Payload mass	1480 kg	2495 kg
Peak heat flux	170 W/cm^2	120 W/cm^2
Total heat load	40 kJ/cm^2	22 kJ/cm^2
Peak dynamic pressure	2.8 kPa	0.3 kPa
$C_{\mathrm{D}}A$	190 m^2	1430 m^2
Minimum β	30 kg/m^2	4 kg/m^2
β ratio	4	67
m_c	n/a	710 kg
P_m	n/a	105 kW
B_0	n/a	250 G

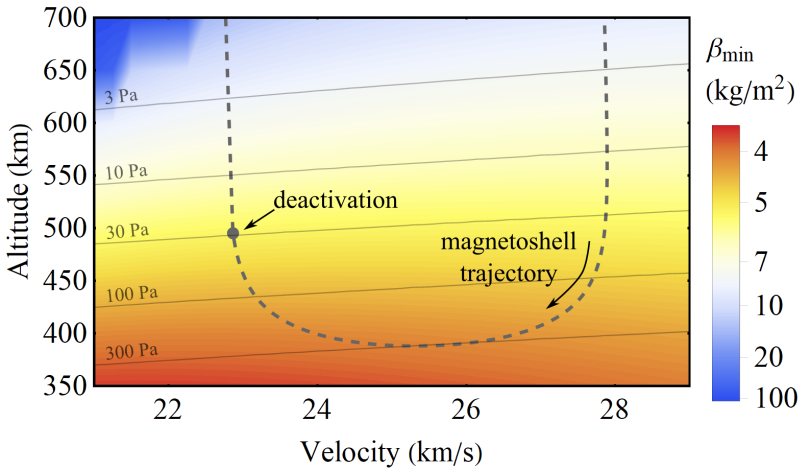

Figure 4.6: Map of best magnetoshell β for the flight envelope in Neptune's atmosphere using the DMPA architecture given in Table 4.1. Gray contours are level curves of dynamic pressure. The dashed gray curve shows a DMPA trajectory calculated with a drag force corresponding to the $\beta_{\min}$ shown.

ways to utilize the design framework presented here. For example, one can design a mission for minimizing discharge power in order to take PPU technology constraints into account. In this case, one would (1) select velocity and density design points based on the mission parameters and heat flux constraint; (2) determine a locus of r_c and B_0 combinations that satisfy the drag requirement; (3) find the (r_c, B_0) combination that minimizes $P_m \times m_c$, then; (4) compute the m_c that minimizes P_m subject to a constraint on m_{tot} (or, alternatively, the m_c that minimizes m_{tot} subject to P_m constraint). The model may also be refined and built upon to take other effects into account such as total heat load constraint, heat shield mass scaling, less conservative energy storage requirement, etc.

4.4.4 Additional Considerations

Finally, we consider some details of the implementation of such a magnetoshell design to ensure it is feasible. In the framework presented above, we explicitly omitted consideration of the electrical configuration of the magnet and battery system to focus on a few key mission design parameters. However, it is relevant to check whether such a magnet can be operated within the technical limits of its components. We show in Table 4.2 that the

magnet designed for the mission described in Table 4.1 and Fig. 4.6 can be built using an arrangement of six electrically parallel windings each receiving 64 A of current. This is achieved with 22 parallel strings of 72 Li-ion batteries each that discharge at 5.4× their nominal capacity, which is safe for this battery chemistry and for this single-use application. The volume occupied by a battery bank of this size is 28U (where 1U = 1 L) based on the volumetric energy density $\alpha_{b,V} = 680$ Wh/L [68]. It is worth mentioning that there is no available space-ready PPU that can handle the 105 kW battery discharge employed by this magnetoshell. However, the NASA NextSTEP partnership has led to development of a PPU capable of supporting a 200 kW nested Hall thruster [71]. This PPU has been demonstrated up to 66 kW output steady-state and 87.7 kW peak as of 2019, on track to eventually support power outputs in excess of 250 kW. We therefore do not anticipate PPU advancement being a bottleneck for magnetoshell technology development.

Another consideration for magnetoshell applicability is how easily the magnetic field can be modulated. This affects the design of a drag-modulation feedback controller that will drive a current through the magnet as an actuator. A magnet of this size and weight can have significant self-inductance that acts to inhibit rapid changes to the flow of current. In practice, this means that the response of the magnet to a control input is delayed on a timescale that may be significant compared to the maneuver duration. We therefore characterize the time constant of the system by considering the magnet as a simple RL circuit. In terms of the magnet design parameters, the inductance and circuit time constant are calculated as

$$L = \frac{\mu_0 m_c^2}{4\pi^2 \rho_w^2 A_w^2 r_c}\left[\ln\left(\frac{8r_c}{\sqrt{A_w/\pi}}\right) - 2\right], \tag{4.28}$$

$$\tau_{\mathrm{RL}} = \frac{L}{R} = \frac{\mu_0 m_c \sigma_w}{4\pi^2 r_c \rho_w}\left[\ln\left(\frac{8r_c}{\sqrt{A_w/\pi}}\right) - 2\right]. \tag{4.29}$$

Notice that unlike the previous magnet design parameters, L does depend on the choice of wire gauge. However, the value of τ_{LR} only increases 30% between 0 AWG and 20 AWG wire so the choice is more strictly driven by ampacity and coil configuration considerations. For the Neptune DMPA design in Table 4.2, the time constant is $\tau_{\mathrm{RL}} = 1.4$ s. This is negligible on the time scale of the aerocapture maneuver (350 s). However, this may have implications

Table 4.2: Sample design of the magnet presented for the Neptune DMPA mission described in Table 4.1.

Parameter	*Value*
Discharge power	105 kW
Wire gauge	5 AWG
Wire material	Aluminum
Total turns, N	1242
Coil thickness	15 cm
# of Parallel coils	6
Turns/coil	207
Current/coil	64 A
Voltage	262.5 V
Total # of 18650B batteries	1604
Battery configuration	72s22p
Battery discharge rate	5.4C
Battery volume	28U
Self-inductance, L	34.3 H
Time constant, τ_{RL}	1.4 s

for the ability of the magnetoshell to respond to rapid atmospheric disturbances. Also, smaller magnets or those with more windings can reasonably have response times on the order of 10 s, which must be taken into consideration in the design of a feedback controller for continuous drag modulation. In Section 4.5, we will examine the modulation demands of the magnetic field to see whether such response times are adequate.

We conclude by re-iterating that magnetoshells are still low-TRL. Past work has attempted to demonstrate technological feasibility in the lab with some positive results [15, 19]. However, the device has never been tested in a representative environment and therefore the key physics such as neutral drag on a dipole plasma and critical ionization sustainment of the magnetoshell are unproven experimentally. A novel technology demonstration experiment seeking to observe some of these crucial physics is detailed in Chapter 5. Ultimately, more advanced experimental facilities and significant investment in technology development are required for magnetoshells to reach space readiness.

4.5 DMPA Trajectories

We now use our understanding of the physics and performance of magnetoshells to analyze the capability of DMPA at Neptune in the face of atmospheric and trajectory uncertainties.

4.5.1 Reference Mission

Because of the unique spacecraft scaling described in Section 4.4 and the unprecedented effective drag area, we must identify a novel reference mission design as the basis for a sensitivity analysis. Several previous analyses of aerocapture at Neptune [72, 73, 7, 74] serve as a guide for general mission constraints such as spacecraft mass/state at atmospheric entry and final orbit parameters. Following these, we select a target orbit size of 4,000 km $\times$ 400,000 km altitude. Though a high inclination orbit is desirable for Triton flybys at this apoapsis [74], we assume an equatorial orbit for simplicity. The atmsopheric entry state is defined at an altitude of h_0 = 1,000 km and atmosphere-relative velocity of v_0 = 28 km/s. The vehicle is assumed to have mass m_{sc} = 5,000 kg with a 4 m diameter and drag coefficient of C_D = 1.7, giving a ballistic coefficient of β = 234 when the magnetoshell is

deactivated. Based on spacecraft size, the magnet is also assumed to have a 4 m diameter to maximize its size as discussed in Section 4.4.

With the orbit inclination, altitude, and velocity defined, determining the reference trajectory is a matter of finding an appropriate entry flight path angle (EFPA). The theoretical corridor width (TCW) describes the range of EFPAs between the steepest possible angle without crashing into the planet and the shallowest possible angle without failing to capture [74]. For the shallow boundary, we assume the magnetoshell stays at full field strength and propagate several trajectories with a series of EFPAs, finding $\text{EFPA}_{\text{min}} = -10.83$ deg for a max field strength of $B_0^{\text{max}} = 1.5$ kG. The steep boundary is computed as $\text{EFPA}_{\text{max}} = -13.32$ deg in the same manner assuming the magnetoshell is deactivated. This results in a TCW of 2.49 deg. Note that Neptune aerocapture studies typically require a TCW of 2.0 deg due to the large uncertainty in atmospheric knowledge [74, 72], something usually attainable only by high-L/D vehicles [73]. For the reference trajectory, we manually select a nominal EFPA of $\gamma_0 = -11.53$ deg, which is within the theoretical corridor. Table 4.3 summarizes the reference mission parameters.

To gain intuition for a DMPA trajectory, in Fig. 4.7(a) we show the flight profile of the reference mission described in Table 4.3. A final apoapsis altitude of $r_a = 397{,}070$ km is reached at the atmospheric exit state, less than 3,000 km below the target. Late in the trajectory, the guidance algorithm determines it has successfully achieved r_a^{targ} and shuts off the magnetoshell (noted by a star in Fig. 4.7) to coast ballistically for the remainder of the atmospheric pass. Fig. 4.7(b) shows the magnetic field actuation throughout this maneuver, varying around $B_0 = 0.3$ kG before going to zero when the magnetoshell is

Table 4.3: Parameters of the reference mission for the sensitivity study.

Spacecraft parameters		**Guidance & control**		**Entry state**	
Total mass	5,000 kg	Field strength	0.2–1.5 kG	Velocity	28 km/s
Vehicle diameter	4 m	Magnetic control gain K_B	0.1	Altitude	1,000 km
Drag coefficient C_D	1.7	Target apoapsis alt.	400,000 km	EFPA	-11.53 deg
Magnet diameter	4 m	Target periapsis alt.	4,000 km	Inclination	0 deg

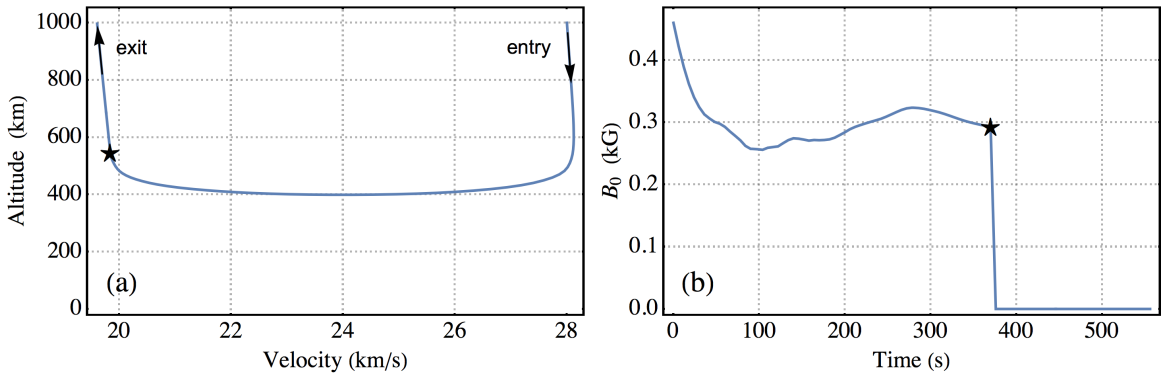

Figure 4.7: (a) Flight profile of the reference DMPA trajectory, showing altitude versus atmosphere-relative velocity. The star notes where the magnetoshell is deactivated. (b) Magnetic field control history during the maneuver.

deactivated. Recall that the field is modulated in response to off-nominal atmospheric density perturbations; we will now examine the sensitivity of the trajectory and magnetic field control to many different atmospheric profiles and EFPAs.

4.5.2 Sensitivity Analysis

To analyze the sensitivity of DMPA performance to density perturbations and EFPA uncertainty, we conduct a Monte Carlo simulation of 1,000 trajectories. The reference mission from Section 4.5.1 is used as the basis for the sensitivity analysis. A set of 200 perturbed Neptune density profiles is taken from the open source Aerocapture Mission Analysis Tool (AMAT) [65], generated using Neptune-GRAM with Fminmax = 0. The onboard density model is the nominal (unperturbed) density profile from AMAT. Each iteration of the Monte Carlo simulation, a truth atmospheric profile is randomly selected from the 200 perturbed cases and the EFPA is sampled from a normal distribution centered on $\gamma_0 = -11.53$ deg. Following Girija *et al.* [74], we use a 3-σ dispersion of 0.33 deg to the nominal EFPA.

Table 4.4 summarizes the results of the Monte Carlo simulation. Only 22 simulation runs result in a failure to reach orbit; the remaining 97.8% of successful aerocaptures are analyzed. The median apoapsis altitude at atmospheric exit is just 3,924 km above the target of 400,000 km, while 93% of all trajectories achieve an apoapsis within $\pm 50,000$ km.

The total Δv required to correct apoapsis and periapsis averages around 100 m/s. We use the Sutton-Graves equation [67] to compute stagnation point heating assuming the entry capsule has a nose radius of 1 m, finding values ranging from 64–138 W/cm^2. The resulting total heat load averages 15.9 kJ/cm^2. These heat metrics are a significant improvement over those for an aeroshell-only architecture. To characterize this benefit for heating and other performance metrics, we will now make a direct comparison to a hypothetical mission involving only an aeroshell drag device.

4.5.3 Magnetoshell vs. Aeroshell Comparison

Though many Neptune aerocapture analyses are present in literature, it is challenging to make direct comparisons with DMPA because it is a drag-only system with unique mission design considerations. Therefore, we run a second Monte Carlo analysis of a nearly identical mission architecture leveraging an aeroshell in a continuously-variable drag modulation aerocapture (CVDMA) scheme. The CVDMA mission is a 5,000 kg vehicle that can bidirectionally control its drag surface diameter between 4 m and 12 m for a β range of 26–234 kg/m^2. Assuming the same entry altitude, inclination, and velocity, the TCW is reduced to just 0.88 deg and we select a nominal EFPA of $\gamma_0 = -12.69$ deg. The area command is

Table 4.4: Statistics for the 97.8% of successfully captured DMPA trajectories.

	Min.	5^{th} %	**Median**	95^{th} %	Max.
Apoapsis altitude (km)	211,190	379,121	**403,924**	440,749	505,444
Periapsis altitude (km)	360.2	376.7	**399.0**	418.7	432.3
Orbit correction Δv (m/s)	86.9	88.0	**93.9**	155.5	663.4
Peak deceleration (Earth g)	5.7	6.1	**7.2**	13.9	43.4
Peak dynamic pressure (Pa)	110.0	146.6	**222.6**	344.8	550.7
Peak stagnation heating (W/cm^2)	64.2	74.9	**90.9**	105.5	138.0
Total heat load (kJ/cm^2)	11.2	12.9	**15.9**	19.7	24.5

actuated proportionally to the apoapsis error the same as in Eq. (4.16), i.e.

$$C_D A(t + \Delta t) = C_D A(t) \times \left(1 + K_B \frac{r_a^{\text{proj}} - r_a^{\text{targ}}}{r_a^{\text{targ}}} \right) , \tag{4.30}$$

using the same gain $K_B = 0.1$.

In Fig. 4.8 we show the statistical results of the DMPA vs. CVDMA comparison. In general, the CVDMA trajectories have a larger variance in performance than DMPA. Despite this, the high-level success metrics are very similar, with 94% of cases within $\pm 50,000$ km of the target apoapsis and 97.4% of cases successfully reaching orbit. DMPA stands out over CVDMA in Figs. 4.8(c)-(e) which demonstrate significantly reduced heat and pressure loads on the vehicle; dynamic pressure is lower by an order of magnitude while heat rate and total heat load are reduced by a factor of three. In practical terms, this comparison highlights the advantages of having a much larger area and range of β values available during drag modulation aerocapture. The implications of these improvements for vehicle design are discussed in Section 4.6.

4.6 Comparison with State-of-the-Art

The results of this sensitivity study indicate DMPA has a final orbit accuracy on par with other Neptune aerocapture architectures. The blunt-body aeroshell design of Girija *et al.* [74], targeting the same orbit as in this study, has varying levels of accuracy depending on atmospheric uncertainty. Excluding the worst-case conditions, they generally find 93-99% of cases reach an apoapsis within $\pm 50,000$ km of the target, comparable to DMPA performance. However, a clear advantage of DMPA is evidenced in the heating and dynamic pressure statistics. Lift/drag modulation architectures such as Girija [74] or Lockwood [73] experience stagnation heating on the order of 5-20 kW/cm^2, a full two orders of magnitude higher than in this study. Drag-only architectures like ADEPT [7] experience improved heat flux ($\sim$200 W/cm^2), but the dynamic pressure is still 10$\times$ higher than that of DMPA. These benefits are largely due to the high periapsis that is enabled by the large effective magnetoshell area; the average trajectory has a periapsis altitude of about 400 km, with the lowest being just 360 km. Compared to 100–200 km for blunt-body aeroshells and $\sim$300 km for ADEPT, DMPA enjoys substantially lower atmospheric density at its operational

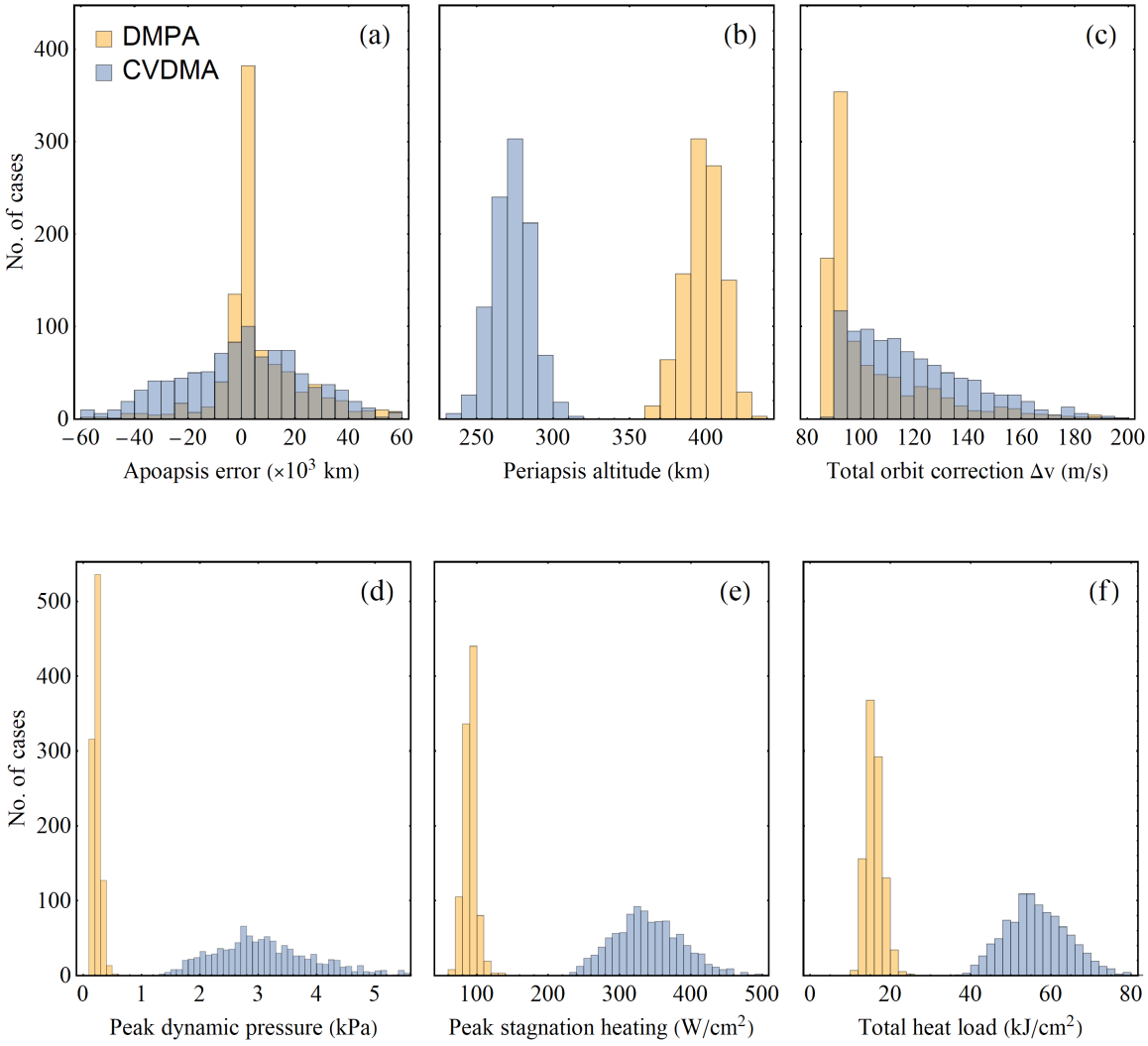

Figure 4.8: Histograms of (a) apoapsis error, (b) periapsis altitude, (c) total orbit correction Δv (periapsis raise and apoapsis correction), (d) peak dynamic pressure, (e) peak stagnation heating, and (f) total heat load for both the DMPA and CVDMA mission architectures.

altitudes. As a consequence, the DMPA entry vehicle does not require advanced TPS solutions and therefore becomes potentially mission-enabling. Venkatapathy *et al.* [75] identify a capability gap in TPS materials, finding no mass-efficient solution that can operate in the Neptune-relevant 1–10 kW/cm^2 heat range. In contrast, to withstand heat rates of ∼100 W/cm^2 as in DMPA, heritage TPS used on missions such as Mars Pathfinder or MSL may be employed. A secondary consequence is that due to the relationship between total heat

load and TPS mass [76], the fraction of the entry system mass devoted to TPS may be reduced by ∼40% [assuming a 3× reduction in heat load as in Fig. 4.8(e)].

In addition to reducing heat and dynamic loads, magnetoshells offer a path to true continuously-variable drag modulation. Putnam and Braun [9] analyzed the efficacy of CVDMA at Mars and Titan, showing that it offers greatly improved performance over single- and two-stage systems. Although they cite ADEPT [3] as a potential technology to achieve the proposed CVDMA scheme, this would require mechanically deploying and retracting the umbrella-like drag skirt during hypersonic atmospheric flight. To date, there is no assessment of the feasibility of such a scheme in the ADEPT literature. A morphable entry system similar to ADEPT has been proposed [77], though the mechanical systems are not considered. In contrast, a magnetoshell can achieve CV drag modulation with no moving parts and mostly leveraging currently available spacecraft technology (possible exceptions are discussed in Section 4.7). According to Table 4.1, magnetoshells are capable of improving the aerocapture system's β-ratio by more than an order of magnitude compared to the ADEPT DMA concept for Neptune [7]. Lifting bodies are capable of continuous trajectory control through bank angle modulation, though the low periapses that accompany such architectures necessitate next-generation heat shields for Neptune aerocapture [6]. Additionally, as shown in Section 4.5.1, DMPA is capable of achieving a TCW that would ordinarily require a high-L/D vehicle, thereby adding trajectory robustness without the additional risk of deep atmospheric flight.

4.7 DMPA Technology Considerations

Unlike other drag modulation aerocapture schemes, DMPA is an active system requiring power to control the magnet throughout the maneuver. Fig. 4.9(a) shows the time history of magnetic field strength for all trajectories in the Monte Carlo simulation of Section 4.5.2. Virtually all cases maintain B_0 in a range of $0.2 \sim 0.7$ kG, with a few exceptions that spike their control input in response to sudden changes in atmospheric density. A 4 m-diameter electromagnet requires significant power and wire mass to achieve these fields, placing constraints on the magnetoshell system design. Using our example mission design as a guide (Section 4.4.3), we make a conservative assumption that the electromagnet consists

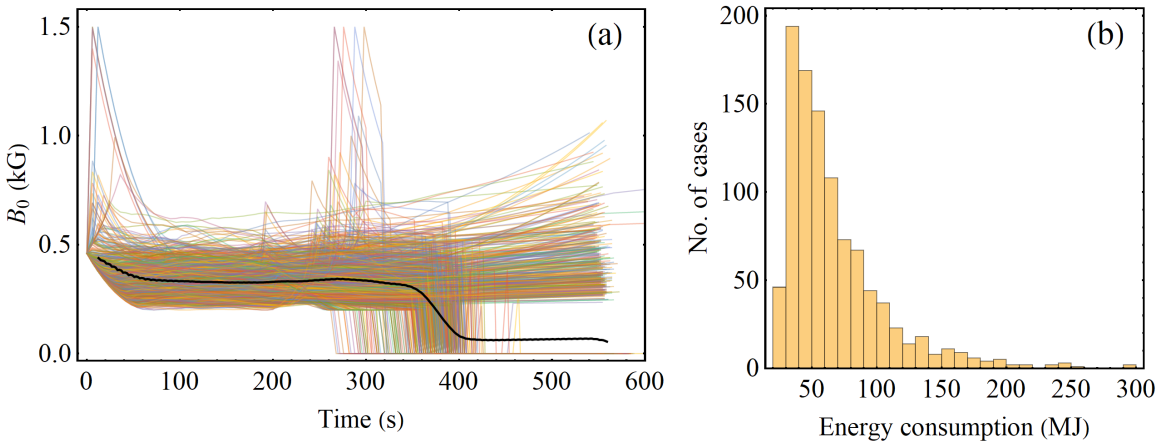

Figure 4.9: (a) Magnetic field, B_0, vs. time for trajectories in the Monte Carlo simulation, with the average shown in black. (b) Histogram of the energy requirement to generate the various $B_0(t)$ commanded in (a).

of 1,000 kg of aluminum wire and is powered by a bank of Li-ion batteries. Fig. 4.9(b) shows a histogram of the total energy required (magnet power integrated over the maneuver) for all Monte Carlo trajectories. The average energy requirement is 67 MJ while the absolute worst case is 298 MJ. With an energy density of 0.9 MJ/kg [68], Li-ion batteries can readily power the magnet at modest weight and would require less technology advancement than developing superconducting magnets for DMPA applications.

One open question concerning the feasibility of DMPA is that of the vehicle configuration. In Fig. 1.2 we depict the electromagnet trailing the vehicle on a tether. This configuration is advantageous in that it keeps the plasma distant from the physical surfaces of the spacecraft, preventing potential damage from plasma-surface interactions. Given its similarity to ballute aerocapture, many of the same considerations and mitigations in regard to stability and wake aerodynamics apply [78]. However, the development of a tether system that can both withstand the braking force and carry power/fuel to the magnetoshell would be a technological bottleneck. A simpler configuration is to have the magnet onboard the spacecraft or clamped to the backshell. This would reduce the complexity of mechanical systems and simplify the vehicle dynamics. However, the sustainment of the magnetoshell from flow energy relies on efficiently confining the plasma; the presence of the spacecraft would

induce large energy losses to walls. This effect may be mitigated by artificially energizing the plasma with more onboard energy, a technique shown in Fig. 4.1 to increase magnetoshell performance when in-situ energy is scarce. Future work must determine whether it is also sufficient to compensate for surface energy loss.

Finally, we note that this trajectory analysis uses a rudimentary numerical predictor-corrector (NPC) guidance scheme with proportional feedback control. Partially for this reason, we have limited the atmospheric uncertainty to Fminmax = 0 rather than a wider range as adopted by other studies. There are various recent advancements in aerocapture guidance that may improve the performance of DMPA. Deshmukh et al. [79] have developed a direct force control guidance algorithm, a more sophisticated NPC scheme that is suitable to controlling drag through magnetic field actuation. Optimal control of β has been investigated for Martian aerocapture [80] while multi-event drag modulation algorithms [81, 82] may also be adapted to the mechanics of bidirectional β control. Future simulation studies should assess whether existing guidance options are sufficient for DMPA under increased uncertainty or a novel approach is required.

4.8 Conclusion

The design framework presented here is intended as a tool for any engineer to generate basic DMPA architectures for trade studies of potential deep space missions. Detailed design of a DMPA mission will ultimately require more advanced considerations. For instance, the flight configuration of the magnetoshell still remains an open question. A trailing magnetoshell will require significant technology development to release a tethered, several-ton coil and maintain stability in flight; meanwhile, a magnet clamped to the vehicle may suffer performance degradation due to the loss of plasma energy to the spacecraft surfaces. Similarly, for planets with a magnetosphere, a large magnet could produce a non-negligible torque on the order of 1$\sim$100 Nm. It is expected that the massive drag force will keep the craft stable, but detailed vehicle-specific analysis is needed to determine if additional measures are required to maintain attitude stability in the presence of this disturbance. The DMPA scaling similarly does not consider TPS implementation for the trailed magnet, the effect of magnet temperature on performance, the reduced mass of capsule heat shielding

for higher altitudes, the effect of the craft's wake on plasma/flow interaction, and tuning the design to specific trajectories, among other things.

Although CV drag modulation trajectory performance has been studied before, this analysis is the first to consider the physical mechanics of a device capable of bidirectional β control. Using magnetic field as a control variable for magnetoshells would skirt the challenges of developing mechanical systems for aeroshells that actuate in high-dynamic-pressure hypersonic flight. Based on this first-order analysis, DMPA is a viable alternative to other proposed aerocapture methods. Future work is needed to assess robustness to increased levels of uncertainty in atmospheric density, velocity, and other mission parameters. A more complex plasma model considering molecular chemistry will also increase the fidelity of trajectory simulations. Despite their simplicity, the design framework and trajectory results presented here provide a useful starting point for the consideration of DMPA in mission design and will inform technology development toward eventual flight implementation of magnetoshells. In Chapter 5, we seek to experimentally confirm some of the key physical effects underlying magnetoshell performance.

Chapter 5

EXPERIMENTAL INVESTIGATION OF NEUTRAL FLOW INTERACTION WITH A MAGNETIZED PLASMA

The interaction between neutral flow and plasma in a magnetic field is relevant to space plasma studies [26, 83], laboratory plasmas [52, 53], and advanced propulsion [84] and atmospheric re-entry [85, 86] concepts. A primary focus is on the critical ionization phenomenon [27] that occurs when the plasma and flow exceed a relative velocity threshold. The effect is governed by the transfer of kinetic flow energy to the electron population which enables rapid and complete ionization of the neutral species. This energy feedback loop is ubiquitous among theoretical [31], simulation [29], and experimental [28] observations of critical ionization, relying crucially on the efficient transfer of energy to electrons.

As shown in Chapter 3, the feasibility of plasma aerocapture hinges on critical ionization-like sustainment of the magnetoshell as it interacts with the atmospheric flow. While our modeling has shown that plasma aerocapture performs well in high velocity (>10 km/s), low density ($<10^{20}$ m^{-3}) settings like Neptune's upper atmosphere [87], these conditions are challenging to reproduce in the lab. A previous technology demonstration used impinging flow on a plasma to show a massive enhancement to the drag force when a magnetic field was introduced [15]. However, the flow consisted of low-speed (<1 km/s) charged particles, obfuscating the role of critical ionization and subsequent momentum transfer in the interaction. An earlier critical ionization experiment with density and velocity regimes consistent with plasma aerocapture demonstrated a deceleration of plasma flow during interaction with a stationary neutral gas [54], lending credence to the proposed mechanism for drag. Still, no experiment has done so with neutrals flowing relative to a fixed plasma and magnetic field as is the case in DMPA.

In this experiment, we investigate the plasma/neutral interaction in a context relevant to plasma aerocapture. The goal of the experiment is to observe two of the key effects on

which plasma aerocapture performance depends: (1) the transfer of neutral kinetic energy to electrons to sustain flow ionization; and (2) the transfer of neutral flow momentum to the magnetic field via ionization and deflection. While a full-scale demonstration is beyond the scope of the current experimental capabilities, results of this work will pave the way for the design of future apparatus that can more thoroughly characterize the performance and physics of the interaction under investigation.

5.1 Experimental Apparatus

The experiment is carried out in the University of Washington SPACE Lab Dielectric Vacuum Facility (DVF). The DVF, shown in Fig. 5.1, is a cylindrical quartz section of 82 cm diameter and 125 cm length compressed between G10 fiberglass walls. On one end is a steel six-way cross with 10" OD flanges. At the other end is an optical viewport and various diagnostic feedthroughs. A 24" $\times$ 12" aluminum optical breadboard is rested on vibration-damping rubber pads in the quartz section to provide hardware mounting points and a stable surface for equipment inside the chamber. The DVF has a pumping speed of 1.1 kL/s and can reach base pressures of 1×10^{-6} Torr using an Osaka TG1113 turbomolecular pump backed by an Edwards E2M12 rotary vane pump.

The experiment consists of two major elements: the neutral beam source and the hollow cathode plasma. Fig. 5.2 gives an overview of the experimental configuration. The neutral beam is generated from within the steel cross and flows into the main chamber. The hollow cathode is mounted inside the quartz section downstream of and perpendicular to the neutral flow. Permanent magnets at both the cathode and anode establish an axial magnetic field ($\sim$1 kG) that collimates the plasma. This allows the hollow cathode to act as a high-density magnetized plasma target for the neutral flow, representative of the device used in plasma aerocapture. These two elements are now described in greater detail.

5.1.1 Neutral Beam Source

The neutral flow source is based on the design of Cuthbertson [88, 89] whose operating principle is summarized here. A plasma is generated in a background magnetic field. An electrically conducting plate is mounted at an angle with respect to the magnetic field lines

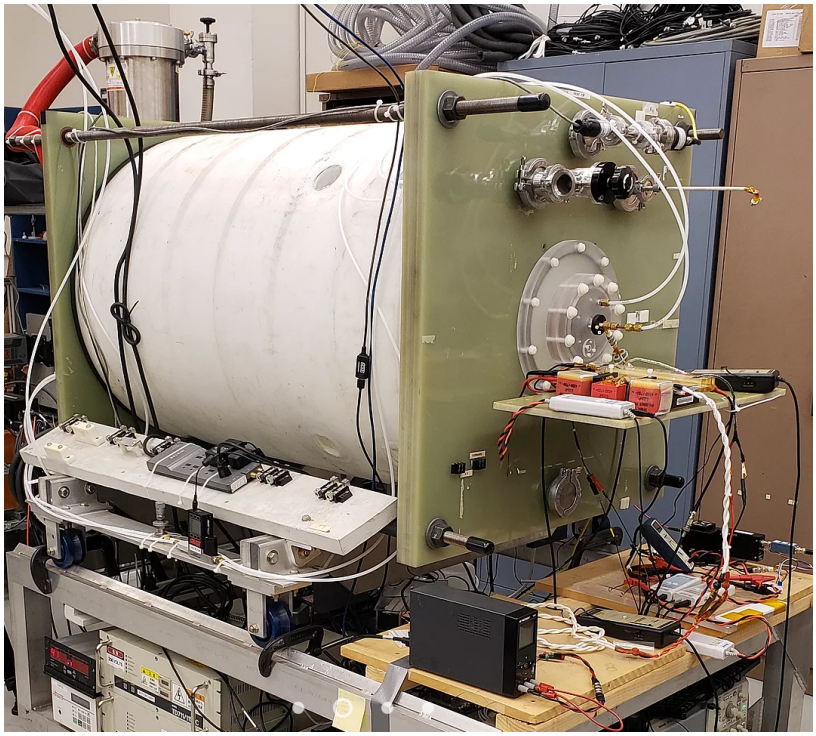

Figure 5.1: The Dielectric Vacuum Facility (DVF) at the University of Washington SPACE Lab.

(typically 45°) and biased to a voltage, V_{plate}, negative with respect to the plasma potential, V_{plasma}. As ions drift along the field, they reach the plate and are accelerated across the potential drop, striking the plate at a high velocity. The ion undergoes surface neutralization on contact provided that the plate material has a low work function and a higher molecular mass than the ionic species. After neutralization and reflection from the plate, the former ions now consitute a neutral flow orthogonal to the magnetic field lines. The flow velocity may be increased by more negatively biasing the neutralizer plate. Because the plate gives an electron to each ion that is neutralized, the current drawn by the plate, I_{plate}, is a direct measure of the flux of neutrals leaving its surface.

In our implementation of this device, we use a Helmholtz configuration of electromagnets wound around opposite sides of the cross flange. Both magnets consist of 300 turns of 19 AWG magnet wire and can generate an on-axis field strength of up to 50 G. A helicon

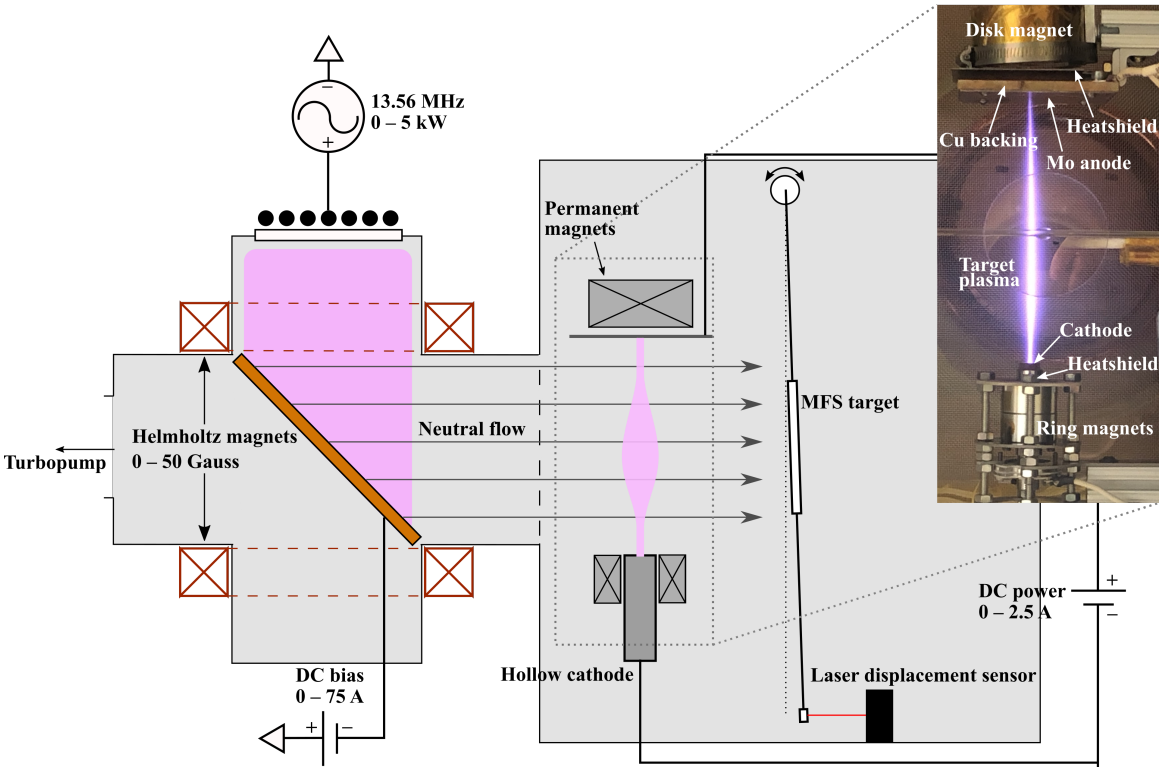

Figure 5.2: Overview of the experimental configuration (not to scale). The cross-shaped flange on the left houses the neutral beam source (helicon plasma and neutralizer plate). The neutral flow enters the main chamber where the hollow cathode and momentum flux sensor assemblies are mounted to an optical breadboard. Inset shows a photo of the cathode-anode system generating the axially magnetized target plasma.

plasma is created via inductive coupling with an antenna mounted externally to a 7.5" diameter, 1/2" thick borosilicate window. The antenna is a water-cooled flat spiral geometry consisting of 3.5 turns of 1/4" OD copper tube. The antenna is driven by a Comdel CB5000 supply capable of providing up to 5 kW of RF power (P_{rf}) at 13.56 MHz. The antenna and Helmholtz coils are shown in Fig. 5.3. Impedance matching is achieved using a Comdel CPMX-6000 self-tuning match network connected to the antenna with copper stripline. A faraday cage is constructed around the antenna and stripline assembly to shield instruments and operators from RF radiation; a copper mesh is also placed inside the vacuum chamber over the opening to the helicon section to shield equipment inside the chamber. All experimental runs presented here use argon injected near the antenna window at a background

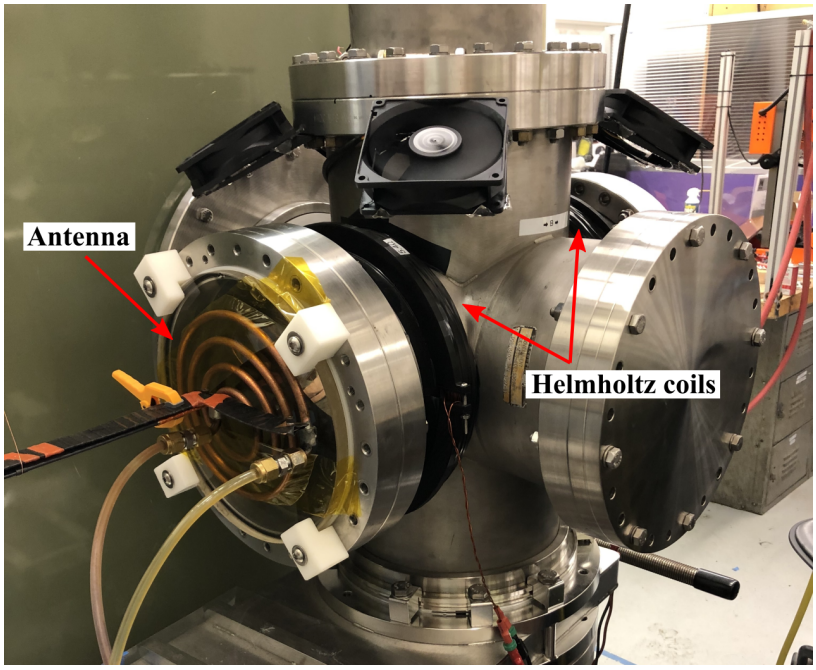

Figure 5.3: Cross-shaped flange section of the experiment on which the flat-spiral antenna and Helmholtz magnet coils are mounted. The electromagnets are air-cooled during operation by four computer fans.

pressure of around 5 mTorr.

The neutralizer plate is constructed of a 1/32" thick molybdenum face bolted to a 1/8" thick copper backing that acts as a heat sink and conductor. The plate is fashioned into an ellipse such that, when mounted at 45° inside the flange, its projection parallel to the magnetic field lines occupies the full 8" inner diameter. The entire plate assembly is sting-mounted to a blank flange opposite the antenna so that it is easily removed to allow physical access to hardware inside the cross. Fig. 5.4 shows the assembly. Because of the potential to draw large currents during operation, the plate is biased using a Lambda ESS DC power supply that can provide up to 75 A of current at up to 200 V. The positive lead is Earth-grounded and the negative lead is connected to the neutralizer plate to provide negative bias voltage. Kapton tape is applied to the entire copper back and around the border of the molybdenum to prevent arcing to the steel chamber wall.

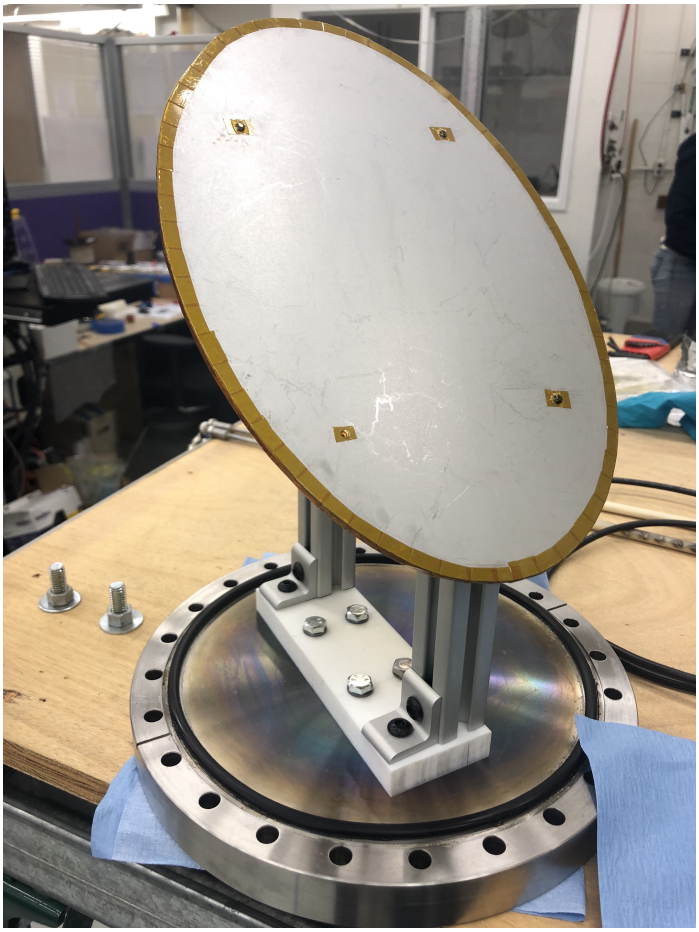

Figure 5.4: The neutralizer plate assembly is mounted to a blank flange for easy removal from the experiment.

5.1.2 Hollow Cathode

The target plasma in the experiment is generated by a heaterless hollow cathode originally developed for a 500 W magnetically shielded Hall thruster. The cathode uses a barium-based porous tungsten emitter manufactured by Plasma Controls [90]. The emitter is housed in a 1/8" tantalum tube with a 0.51 mm orifice. The tube is electrically and thermally insulated from the stainless steel keeper assembly by a 1/4" alumina tube. An interchangable graphite keeper electrode is mounted at the end of the keeper assembly 3 mm from the cathode orifice. For the duration of testing, a 1 mm diameter keeper orifice was used. A 4" square anode

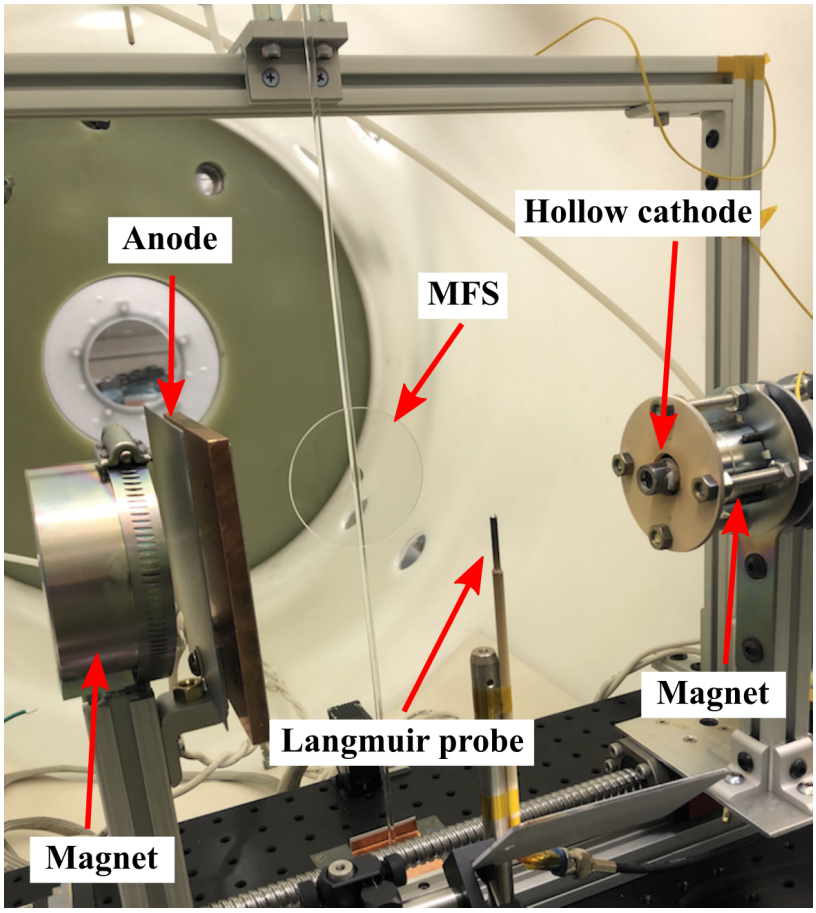

Figure 5.5: The target plasma apparatus consists of the hollow cathode, anode plate, and permanent magnets to generate an axial field. A Langmuir probe is inserted just below the cathode-anode central axis. The momentum flux sensor (MFS) pendulum is suspended downstream of the target plasma region.

is positioned facing the cathode at a separation distance of about 20 cm. The anode is a 1/32" thick molybdenum plate bolted to a 1/8" thick copper backing plate. Fig. 5.5 shows the cathode/anode assemblies in the chamber.

To enhance the density and temperature of the hollow cathode plasma, an axial magnetic field is applied between the cathode and anode [91]. Two grade N42 neodymium ring magnets of 1.5" OD and 3/4" length each are mounted concentrically around the keeper assembly (Fig. 5.2, inset). A 3" OD, 1.5" thick disk magnet (grade N52) is mounted behind the anode assembly. Molybdenum heatshields are installed between the keeper and

ring magnets and between the anode and cylindrical magnet to protect the magnets from demagnetization due to radiative heat flux. The field at the both the keeper orifice and anode is 2 kG. The cathode is mounted on a translation stage to modulate the electrode spacing and therefore adjust the axial magnetic field strength. The minimum axial field strength is 0.5–1.5 kG depending on this spacing. In this experiment, the cathode orifice is kept at a fixed distance of 20 cm from the anode for a minimum axial field of 1 kG.

The main and keeper discharges are driven by TDK-Lambda 600-2.6 and 600-1.3 DC power supplies, respectively. Flyback diodes and ballast are used to control the ignition which is initiated at 1 A on the main discharge and 0.75 A on the keeper. The high axial field necessitates a modified startup procedure in which the keeper and main discharges are initiated simultaneously to increase stability. Steady state is achieved within 30 seconds of ignition and the keeper current is reduced to 0.15 A after the insert reaches emission temperature. The cathode is operated on 30 sccm of argon with the current varied between 0.5–2.5 A and a background chamber pressure of 4–8 mTorr.

Fig. 5.6(a) shows the hollow cathode during experimental operation at five currents from $I_{\mathrm{hc}} = 0.5$ A to 2.5 A. The axial magnetic field effectively collimates the plume which appears dim and pink at 0.5 A. As the current is increased, the plasma core increases in size slightly and gets brighter, eventually turning a bright blue at 2.5 A. The glass disk used for the MFS target is visible in these photos between the viewer and the plasma, its transparency enabling observation during the experiment. In Fig. 5.6(b) the exit plume of the hollow cathode is shown while the neutral beam is active; the helicon plasma source is seen beyond the target plasma against the backdrop of the neutralizer plate.

5.1.3 Diagnostics and Data Analysis

Both the neutral flow and the target plasma must be characterized independently and during their interaction. Three primary diagnostics are employed to analyze the system: (1) a momentum flux sensor placed downstream in the neutral flow; (2) an RF-compensated Langmuir probe inserted in the helicon plasma; and (3) a Langmuir probe inserted in the hollow cathode plasma. In addition to these, which are described in detail below, the current

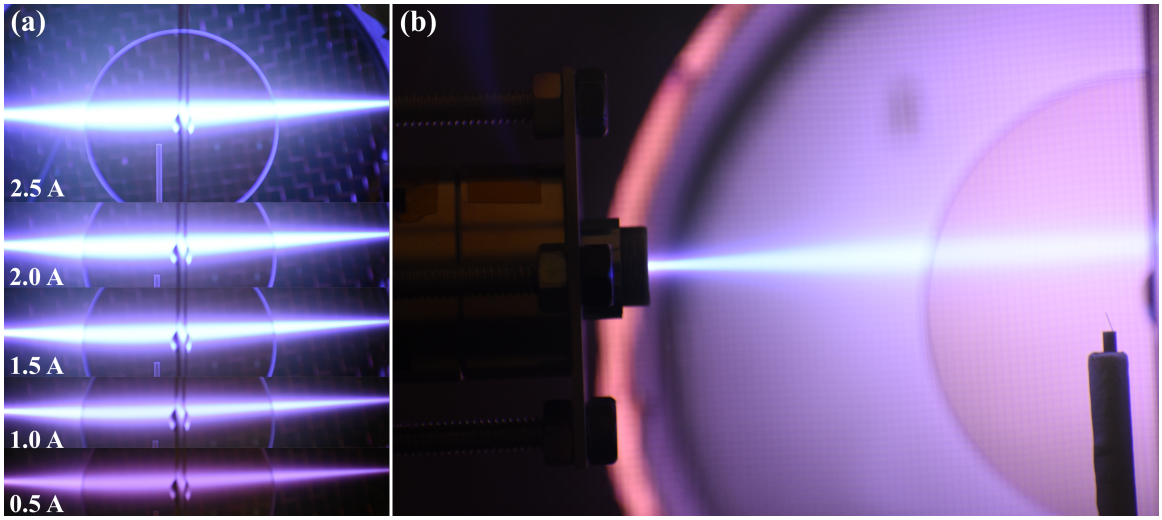

Figure 5.6: (a) Hollow cathode plasma operating at five currents from 0.5 A to 2.5 A. (b) View of the hollow cathode exit plume with the neutral beam helicon plasma source operating in the backgound.

drawn by the neutralizer plate is measured using a shunt resistor in series with the Lambda ESS power supply output.

Momentum Flux Sensor

A momentum flux sensor (MFS) is a target mounted on a pendulum arm that is immersed in a particle flow. The flux of particles impacting the target causes a drag force, F_D, that deflects the pendulum arm. The deflection is measured to obtain F_D and make inferences about the flow. MFS are typically employed in the exhaust of electric propulsion devices as an indirect thrust measurement technique [92, 93, 94] and their operating principle lends itself well to application in our experiment. We base our MFS on the design of West *et al.* [95].

Fig. 5.5 shows the MFS pendulum. A glass disk of 3" diameter is used as the MFS target. The target is attached with epoxy to a 5 mm diameter glass rod. The rod is suspended from a metal plate with the use of two spikes functioning as a virtually frictionless fulcrum. From the fulcrum, the distance to the pendulum assembly center of mass is 20.9 cm, to the target

is 32.5 cm, and to the end of the rod is 55.5 cm. The total mass of the pendulum assembly is 66.7 g. Two small magnets are mounted below the pendulum that damp its oscillation through eddy interaction with a small piece of 1/64" thick copper sheet that is epoxied to the end of the rod. The copper sheet is bent 90° upward on the leeward side of the pendulum and a strip of white tape is applied to the bent face. This tape serves as a reflective surface for the beam of a Keyence IL-065 laser displacement sensor. The displacement is read by an oscilloscope with a Keyence IL-1000 amplifier unit having a sensitivity of 350 mV/mm. An analog lowpass filter is used at the oscilloscope input to reduce RF noise in the signal while the neutral beam is firing.

The MFS is calibrated in the manner described by West *et al.* [95] using a 25 mm moment arm and successive weights up to 8 g. From this process we determine a conversion of 2.2 μN/mV for the target force measurement. During experiment runs, we operate the neutral flow in 10 s pulses, allowing the MFS to reach a mostly damped equilibrium displacement. Fig. 5.7 shows a typical trace obtained from the MFS. The raw data collected by the oscilloscope appears as an underdamped step response starting when the neutral flow is turned on at $t = 0$. After smoothing the data with a numerical filter, we see the center of oscillation steadily rises in the first few seconds while the matching network fine-tunes the power coupling to the helicon plasma. The steady-state deflection signal is extracted once the match has reached equilibrium and is taken as the mean of the filtered signal over three oscillation periods. The signal error is the standard deviation of the raw data in the extraction region.

Langmuir Probes

To measure characteristics of the target plasma, a Langmuir probe is inserted in the plume of the hollow cathode directly in front of the MFS target. It is offset 1 cm below the plasma core to avoid overheating the tip and mitigate disturbance to the plume. The cylindrical electrode is tungsten wire of 0.12 mm diameter and 3.42 mm exposed length. It is shielded by a 2.4 mm OD alumina tube slotted inside a 6.6 mm OD grounded steel shield that is insulated from the plasma with alumina paint. The probe is swept from -45–30 V with a

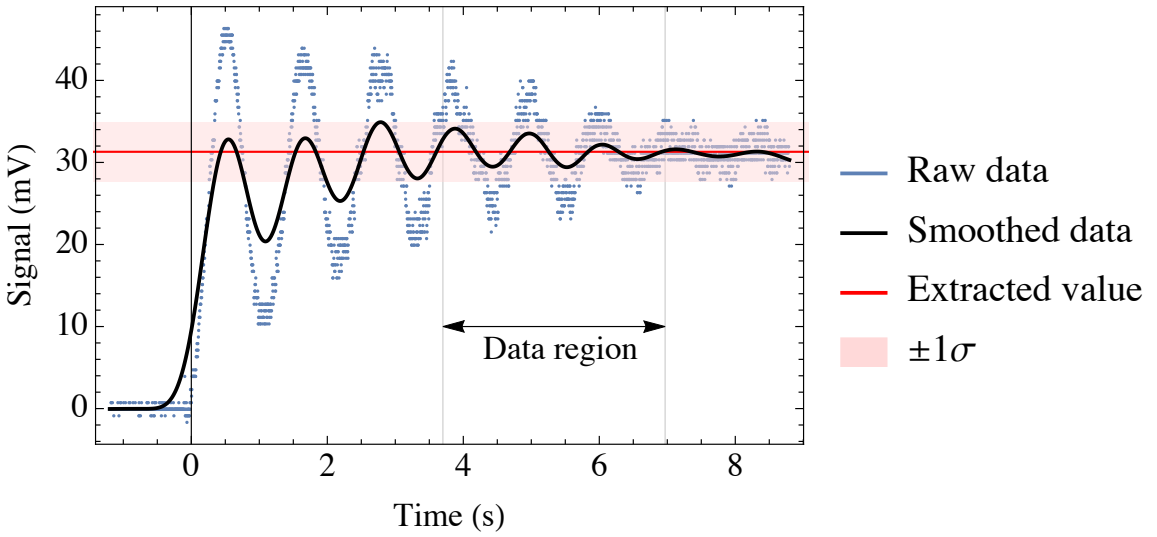

Figure 5.7: A typical MFS trace during neutral beam operation. Extracting the steady-state deflection of the MFS involves numerically smoothing the raw data and extracting the mean of the signal over three oscillation periods after the helicon plasma has reached a match condition. The force on the target corresponding to this trace is $F_D = 67.7 \pm 7.8$ μN.

Kepco BOP-500M power supply driven by a 10 Hz triangle wave function. The I-V trace is captured by a Tektronix TPS 2024B oscilloscope. Ion saturation current is determined by linear fit to voltages below the floating potential; this is subtracted from the trace to determine electron current, I_e. Electron temperature, T_e, is found from the inverse slope of $\ln I_e$ in the electron retarding region of the curve. Because of the small diameter probe tip, sheath expansion must be accounted for to compute ion density, n_i. An iterative algorithm is applied (described in Section II.F of Lobbia *et al.* [96]) to converge on valid solutions for T_e and n_i according to transitional and orbital motion-limited sheath theory. Finally, quasineutrality is assumed such that $n_i = n_e$.

The helicon plasma poses a greater diagnostic challenge due to the kW-level RF power environment. For this reason, an RF-compensated Langmuir probe (RF-LP) is constructed to circumvent the distortion caused by rapidly fluctuating potentials. The RF-LP compensates for locally oscillating plasma potential with a pair of notch filters embedded near the tip which filter out signals in narrow bands centered on 13.56 MHz and its first harmonic,

27.12 MHz. A reference electrode is exposed to the plasma near the collecting electrode and is capacitively coupled to the collection/filter circuit to reduce the high-frequency current load at the tip. The RF-LP is built following the circuit architecture shown in Fig. 13 of Lobbia *et al.* [96]. The reference electrode is a 1 cm section of steel tube exposed to the plasma. The collecting electrode is a cylindrical tungsten wire of 0.13 mm diameter and 1.75 mm length. The probe is inserted in the center of the helicon plasma at a distance of 6 cm from the neutralizer plate using a grounded steel shield nested inside an 8 mm OD alumina tube. The last 1 cm of the RF-LP extending beyond the reference electrode is 3 mm OD alumina to reduce local disturbance of the plasma. The voltage is swept from -40–40 V and data analysis is conducted in the same manner as above.

5.2 Neutral Beam Scaling

We characterize the neutral beam by combining measurements from the RF-LP, neutralizer plate, and MFS. Data is collected for input conditions of V_{plate} = -15 to -75 V in -15 V increments and P_{rf} = 300 to 1,500 W in 200 W increments. The working gas is argon and the helicon plasma is ignited at background pressures of ∼5 mTorr. In Fig. 5.8 we show the helicon plasma source density and temperature measured by the RF-LP. Densities are on the order of 1–5×10^{18} m^{-3} and the electron temperature ranges from 3–8 eV. Note there is an increasing trend in n_i and T_e with P_{rf} which we will later show strengthens the neutral flow.

Fig. 5.9(a) shows the drag force on the MFS target, F_D, as a function of the current drawn by the neutralizer plate from the helicon plasma, I_{plate}. Following Cuthbertson [88], we assume the plate collects an ion saturation current at sufficiently negative voltages. At the field strengths and RF powers used in this experiment, the plasma is assumed to be singly ionized [97]. Thus, I_{plate} corresponds directly to the flux of neutrals leaving the plate. We note that I_{plate} is divided by $(1+\gamma_i)$, where $\gamma_i = 0.122$ is the secondary electron emission coefficient for argon impacting molybdenum in the energy range of interest (10–100 eV) [88]. Fig. 5.9 shows that F_D scales strongly with I_{plate} which strongly indicates the presence of a neutral beam. To confirm that a charged particle flow is not causing the MFS deflection, the downstream Langmuir probe was activated during neutral beam operation and no charged

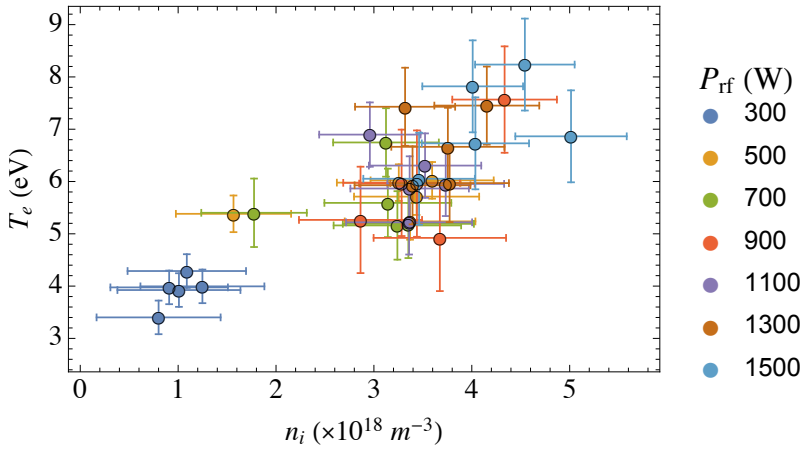

Figure 5.8: Electron temperature, T_e, versus ion density, n_i, in the neutral source helicon plasma reveals two distinct modes governed by the RF power input, P_{rf}.

particle population was detected above the diagnostic sensitivity of around 10^{15} m^{-3}.

To better understand the efficiency of converting the helicon plasma to a directed neutral flow, we wish to examine how the flow dynamic pressure changes between being accelerated to the neutralizer plate and reaching the MFS target. The dynamic pressure of the ion flow striking the plate is $q_{\mathrm{plate}} = m_i(n_i u_i)_{\mathrm{p}} u_i/2$. The quanitity $(n_i u_i)_{\mathrm{p}}$ is the ion flux at the plate surface. This is measured experimentally as the plate current where $I_{\mathrm{plate}} = e(n_i u_i)_{\mathrm{p}} A_{\mathrm{plate}}$ for a plate area $A_{\mathrm{plate}} = 146$ cm^2. The ion velocity at the plate can be estimated following Cuthbertson [88] as

$$u_i = \sqrt{\frac{e(V_{\mathrm{plasma}} - V_{\mathrm{plate}})}{m_i}} \tag{5.1}$$

where V_{plasma} is the helicon plasma potential as measured by the RF-LP. Combining the measured ion flux and estimated velocity, the ion dynamic pressure at the plate is

$$q_{\mathrm{plate}} = \frac{I_{\mathrm{plate}}}{2A_{\mathrm{plate}}} \sqrt{\frac{m_i(V_{\mathrm{plasma}} - V_{\mathrm{plate}})}{e}}. \tag{5.2}$$

The neutral flow dynamic pressure at the MFS target is much simpler:

$$q_{\mathrm{target}} = \frac{F_D}{C_D A_{\mathrm{target}}}, \tag{5.3}$$

where $C_D \approx 2$ is the drag coefficient of a disk in hypersonic free molecular flow [98] and $A_{\mathrm{target}} = 45.6$ cm^2 is the area of the disk. Fig. 5.9(b) shows the relationship between q_{target}

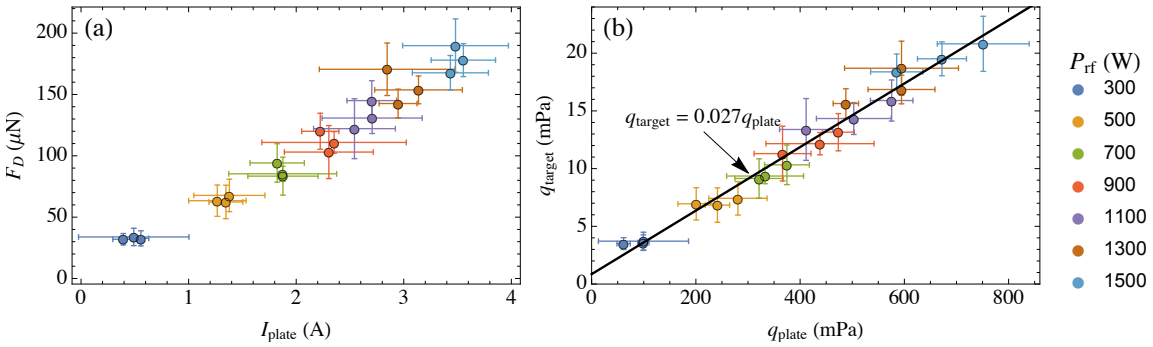

Figure 5.9: (a) The drag force on the target, F_D, scales linearly with the neutralizer plate current, I_{plate}, indicating the presence of a neutral beam. (b) Dynamic pressure measured at the MFS target, q_{target}, corresponds to dynamic pressure of ions striking the neutralizer plate, q_{plate}.

and q_{plate}. Note that these two quantities are measured by independent diagnostics. We find that there is a strong linear correlation described by $q_{\text{target}} \approx 0.027 q_{\text{plate}}$. Thus, about 97.3% of the flow energy density is lost in striking the plate, becoming neutralized, reflecting from the plate, and diverging/colliding with background neutrals as it travels downstream to the MFS target. Despite this, Fig. 5.9(a) indicates there is still a force on the order of 100 μN, easily resolvable by the μN-sensitive MFS system.

In Fig. 5.10 we show how the neutral beam performance scales with the operating parameters P_{rf} and V_{plate}. As anticipated, F_D increases as both the RF power is increased and the plate voltage is made more negative. These reflect an increase in the density and velocity, respectively, of the neutral flow. The general scaling observed is consistent with the results of Cuthbertson [88]. These results serve as a baseline of neutral flow performance that will inform our analysis of its interaction with the hollow cathode plasma.

5.3 Plasma-Flow Interaction

5.3.1 Hollow Cathode Plasma Characteristics

Here we examine the effect of the neutral beam on the hollow cathode plasma. The neutral beam source is operated at RF powers of $P_{\text{rf}} = 500$–$2{,}000$ W in 250 W increments and plate voltages of $V_{\text{plate}} = \text{-}10 - \text{-}40$V in -10 V increments. The hollow cathode is operated at

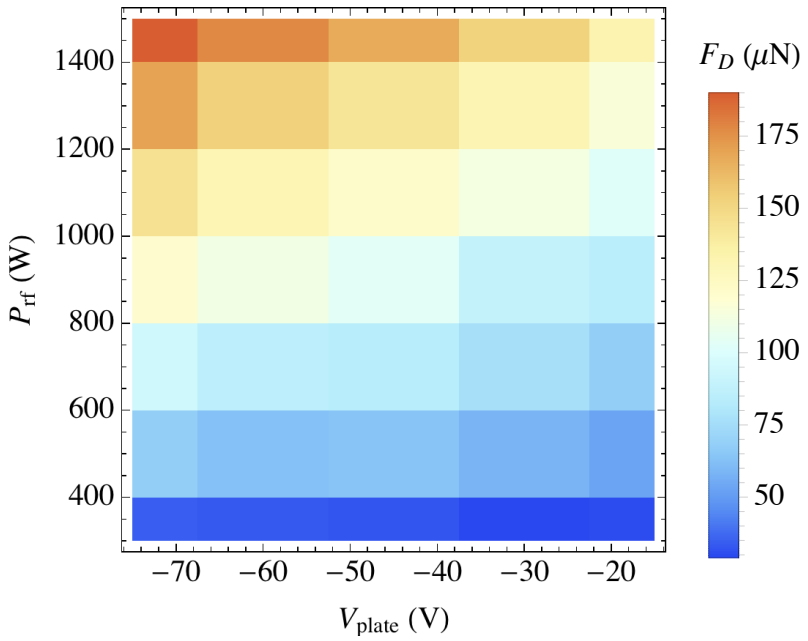

Figure 5.10: Drag force on the MFS target, F_{D}, scales strongly with the RF power applied to the neutral beam source, P_{rf}, and bias voltage of the neutralizer plate, V_{plate}.

currents of $I_{\mathrm{hc}} = 1$–2.5 A in 0.5 A increments. A baseline Langmuir probe measurement of the target plasma is taken between each distinct neutral beam firing. The plasma parameters during neutral beam operation are compared to the preceding baseline measurement to ensure any changes to the target plasma resulting from flow interaction are distinguished from drifting steady state conditions over the hours-long test campaign.

In Fig. 5.11(a), we show the electron temperature and ion density of the unperturbed plasma (i.e. without the neutral beam running) measured by a Langmuir probe inserted about 1 cm below the central axis. Note that these represent all the baseline measurements taken between firings, hence there is some scatter in plasma parameters for the same I_{hc}. Regardless, n_i and T_e are fairly consistent across different hollow cathode currents, except for the $I_{\mathrm{hc}} = 1$ A case which is of a lower density. Fig. 5.11(b) depicts the same parameters in the case where the neutral beam is actively flowing across the target plasma. These data represent all the combinations of V_{plate} and P_{rf}; scaling with these inputs is discussed later. There is a noticeable increase in plasma density, temperature, or both compared to the

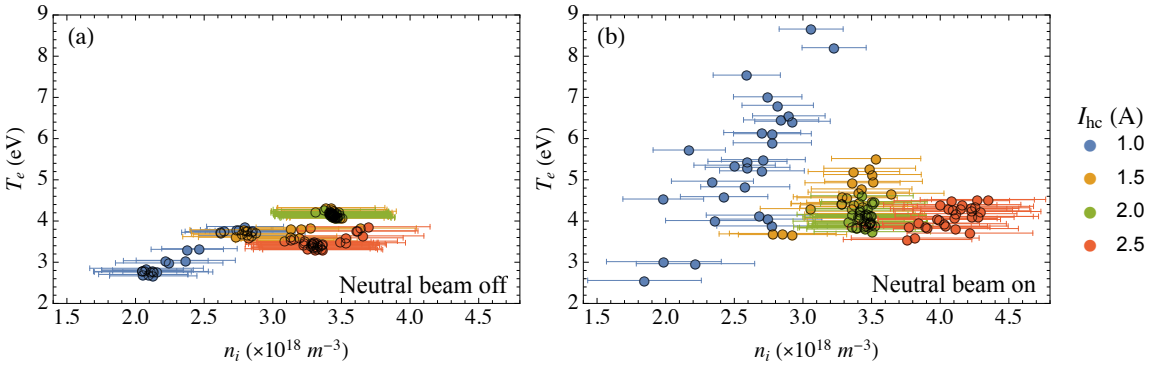

Figure 5.11: Electron temperature, T_e, and ion density, n_i, of the hollow cathode plasma for (a) unperturbed and (b) neutral beam on conditions.

unperturbed conditions. The $I_{hc} = 1$ A case exhibits the strongest change, experiencing a significant increase in T_e by up to a factor of two. At $I_{hc} = 2.5$ A, there is a modest increase in both n_i and T_e by ~20%. Regardless of the magnitude of change, it is notable that the hollow cathode exhibits different steady-state parameters in response to the neutral flow. This suggests some interaction between the two that influences the plasma.

To further characterize this influence, we examine the voltage required to sustain the hollow cathode discharge, V_{hc}. Fig. 5.12 shows how the discharge is affected by the neutral beam. We observe that for all I_{hc}, the unperturbed plasma ($P_{rf} = 0$ W) requires a higher V_{hc} than the flow-interacting case and V_{hc} decreases monotonically as P_{rf} is increased. Since the power sustaining the hollow cathode is $P_{hc} = I_{hc}V_{hc}$, this reflects a decrease in the power injected to the target plasma as the neutral beam power increases. The power drop ranges from 0.5–3.5 W (roughly 1–5% of P_{hc}). This again suggests an interaction between the neutral flow and hollow cathode that affects the energy balance of the target plasma. In the following section, we investigate the various channels for energy gain and loss to better understand the results seen in Figs. 5.11 and 5.12.

5.3.2 Energy Transfer

A key effect in critical ionization is the transfer of kinetic energy from the neutral flow to electrons that sustain the discharge. To assess the energy transfer in our experiment, we

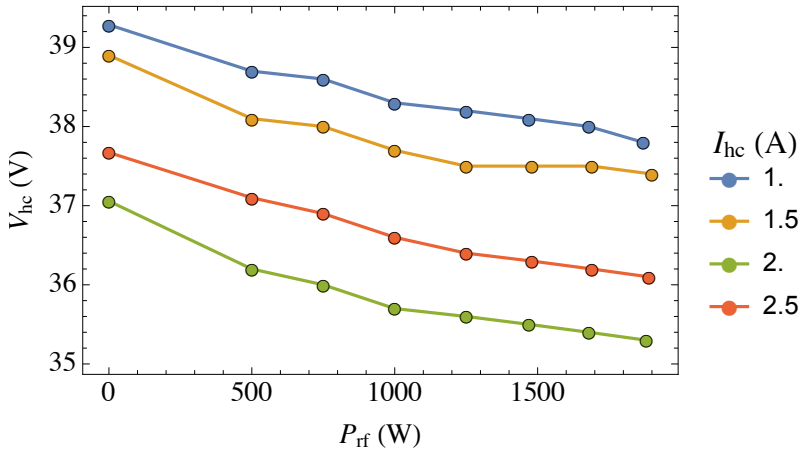

Figure 5.12: The hollow cathode discharge voltage, V_{hc}, decreases as the neutral beam RF power, P_{rf}, is increased. Conditions shown are for $V_{\text{plate}} = -20$ V.

represent the hollow cathode plasma with a 0-D power balance model:

$$P_{\text{hc}} + P_{\text{nb}} = P_{\text{diff}} + P_{\text{wall}} + P_{\text{ion}}. \tag{5.4}$$

The two terms on the lefthand side of Eq. (5.4) are the power deposited to the plasma by the hollow cathode power source (P_{hc}) and the neutral beam itself (P_{nb}). The righthand side represents the power lost from the system due to cross-field diffusion (P_{diff}), wall losses from parallel diffusion to the cathode and anode (P_{wall}), and effective ionization losses (P_{ion}). We assume an effective energy loss timescale, τ_e, such that energy is lost at a rate scaling with n_e/τ_e. Assuming $T_e \gg T_i$, the energy lost from the system per ion-electron pair is $\frac{5}{2}T_e + \varepsilon_{\text{ion}}$, where ε_{ion} is the effective ionization cost including scattering and excitation losses. Therefore, Eq. (5.4) can be rewritten as a volume-averaged power balance,

$$P_{\text{hc}} + P_{\text{nb}} = \frac{n_e}{\tau_e}\left(\frac{5}{2}T_e + \varepsilon_{\text{ion}}\right)V, \tag{5.5}$$

where V is the volume of the plasma. We wish to quantify P_{nb} while P_{hc}, n_e, T_e, and $\varepsilon_{\text{ion}}(T_e)$ are known or computed from experimental measurements. The cylindrical volume V is estimated from photographic determination of the radius of the bulk plasma, $r_{\text{plasma}} = 5$ mm, and the separation distance between anode and cathode, $L_{\text{plasma}} = 20$ cm. Therefore we must determine the scaling of τ_e with known parameters in order to estimate P_{nb}.

With the neutral beam off, i.e. $P_{\rm nb} = 0$, the characteristic energy loss timescale is

$$\tau_e = \frac{n_e \left(\frac{5}{2} T_e + \varepsilon_{\rm ion}\right) V}{P_{\rm hc}} \tag{5.6}$$

from rearrangement of Eq. (5.5). We calculate τ_e using experimental measurements of n_e, T_e, and $P_{\rm hc}$ with the neutral beam off. For this calculation we use the approximate function for $\varepsilon_{\rm ion}(T_e)$ in argon provided by Lieberman [45]. Fig. 5.13 shows that at different current settings of the hollow cathode, there is a linear relationship between τ_e and the ratio n_e/T_e. The slope of the linear fit decreases as the hollow cathode current is increased. The fits are described by the same relationship,

$$\tau_e(n_e, T_e, I_{\rm hc}) \approx \frac{14.1}{I_{\rm hc}} (n_e/T_e) \times 10^{-18} \ , \tag{5.7}$$

for τ_e in μs, n_e in m^{-3}, T_e in eV, and $I_{\rm hc}$ in A. Eq. (5.7) supports the assumption of diffusion as the primary loss mechanism; the scaling with $1/T_e$ is consistent with Bohm, but the scaling with n_e suggests a classical effect as well. This plasma may be in a transitional diffusion regime between the two, as has been described by Yoshikawa and Rose [99] in a similar axially-magnetized hollow cathode. This transitional regime exists at moderate field strength [100] such as that used in this experiment.

Using the linear fit for τ_e as a function of experimentally measured quanitities, we can now estimate $P_{\rm nb}$ using Eq. (5.5) and data taken during neutral beam operation. We conservatively assume the plasma volume is unchanged for this calculation. In Fig. 5.14(a), we show the results of computing $P_{\rm nb}$ in the manner described. $P_{\rm nb}$ is plotted against the characteristic reaction rate of a neutral with the plasma,

$$1/\tau_{\rm cap} = n_i (R_{\rm ion} + R_{\rm cx}), \tag{5.8}$$

where $R_{\rm ion}$ and $R_{\rm cx}$ are the reaction rate coefficients for ionization and charge exchange given by Lieberman [45] and Phelps [101], respectively. The power deposited by the neutral beam is a positive linear function of the reaction rate. This relationship supports the hypothesis that the neutral beam is indeed transferring energy to the plasma; as neutrals interact with the plasma and become ions at a faster rate, more kinetic energy is deposited to the hollow cathode discharge. This is also consistent with the findings of previous global modeling

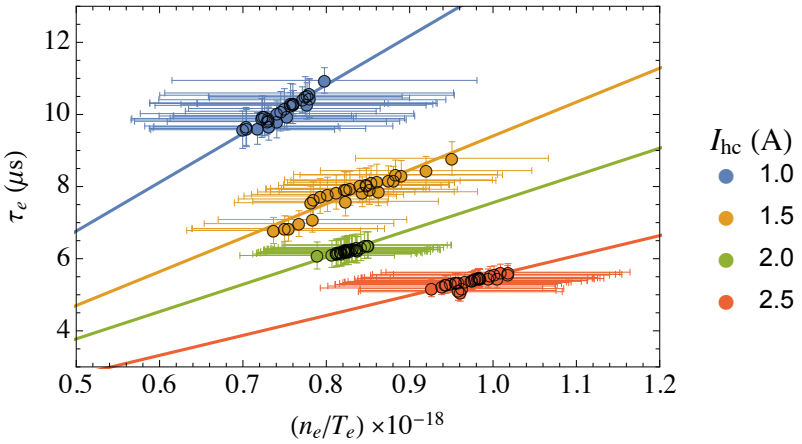

Figure 5.13: The characteristic energy loss timescale, τ_e, is a linear function of n_e/T_e whose slope depends decreases with hollow cathode current, I_{hc}. These data are taken between firings of the neutral beam and the scatter at each current is due to drifting steady-state operating conditions.

which showed that as the reaction rate increases, the contribution of neutral flow to the overall power balance grows relative to the injected power [35].

Fig. 5.14(b) shows the effect of the neutral beam on the electron temperature. Note that P_{nb} is expressed as a percentage of P_{hc} and electron heating is expressed as a percent increase from the unperturbed temperature. There is a clear positive correlation between power deposition and electron heating. This suggests that a portion of the energy absorbed from the neutral beam is transferred to the electrons, a process that is necessary for critical ionization to occur. However, $P_{nb} < P_{hc}$, a feature of the "injection regime" found in global modeling [35] in which plasma energy gain is dominated by injected power rather than flow absorption. Electron heating is consistent with modeling in this regime; cooling would be observed at higher deposited powers due to increased ionization losses once critical ionization initiates. Fig. 5.14(b) therefore provides evidence that energy is transferred from the flow to the plasma, though there is insufficient transfer to reach a critical ionization regime in this experiment. In Section 5.4, we investigate how this experimental architecture may scale to enable such a regime.

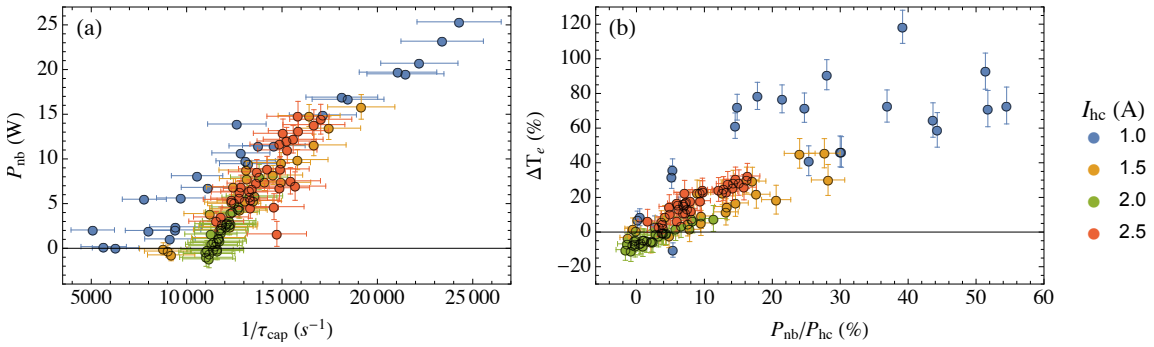

Figure 5.14: (a) Power deposition by the neutral beam to the plasma, P_{nb}, correlates positively with the characteristic reaction rate of neutrals with the plasma, $1/\tau_{\mathrm{cap}}$. (b) The increase in electron temperature from unperturbed to flow-on conditions, ΔT_e, correlates with the ratio of neutral beam power to injected power, $P_{\mathrm{nb}}/P_{\mathrm{hc}}$.

5.3.3 Momentum Transfer

Section 5.3.2 demonstrates that there is some interaction between the plasma and flow enabling an exchange of energy. For plasma aerocapture applications, it is essential to determine whether this interaction can lead to a force on the magnets, i.e. a transfer of momentum from flow to plasma. While this cannot be measured directly in this experimental setup, it may be inferred by comparing MFS measurements taken with and without a hollow cathode plasma present. Any transfer of momentum to the plasma would result in a decrease in neutral flux to the MFS, and therefore a decrease in F_D. We characterize this change in measured force as

$$\Delta F_D = \frac{F_D^{\mathrm{on}} - F_D^{\mathrm{off}}}{F_D^{\mathrm{off}}}, \tag{5.9}$$

where F_D^{on} and F_D^{off} are the drag of the flow on the MFS target with the hollow cathode on and off, respectively.

Curiously, the raw data show an *increase* in the force on the MFS target while the hollow cathode plasma is present, with $\Delta F_D \approx 25$–65% and generally increasing with I_{hc}. We observed during experimental testing that the pendulum exhibits a steady-state deflection (without the neutral beam running) that grows larger as I_{hc} is increased. To characterize this effect, we sampled this deflection across a range of hollow cathode currents from 0.2–2.5

A. Fig. 5.15(a) shows the results of this sweep in which we find the deflection force, F_{def}, to scale most strongly with the plasma pressure, $n_e k_b T_e$. There is a linear correlation of $F_{\text{def}} \approx 33.8 n_e k_b T_e$. Thus, it is likely that the pressure acting on the plasma-facing side of the target causes this deflection. As shown in Fig. 5.11, the presence of the neutral beam induces a higher electron pressure in the hollow cathode plasma; any reduction in F_D resulting from magnetic deflection of ionized flow may be more than offset by enhanced plasma pressure, causing spuriously high measurements.

Taking the difference in plasma pressure between neutral beam on and off cases, we use the linear correlation shown in Fig. 5.15(a) to calibrate out this extrinsic force. Fig. 5.15(b) shows the resulting ΔF_D for four different hollow cathode currents from 1–2.5 A. The process of subtracting the pressure force introduces errors of ±10–40% to ΔF_D due to the inherent uncertainty of Langmuir probe measurements. As a result, for many of the data points it is not possible to determine whether there is an increase or decrease in F_D due to plasma-flow interaction. However, we do observe a generally decreasing trend as P_{rf} is increased, consistent with observations of enhanced interaction at higher neutral beam powers (Fig. 5.12). Additionally, the four distinct I_{hc} data are distributed both above and below $\Delta F_D = 0$. This suggests there may be higher order effects contributing to the force balance on the MFS that are unaccounted for by our analysis. For instance, the plasma may not only change in pressure but also in radial profile when the neutral beam is active, leading to higher forces than inferred by our static probe measurements. Alternatively, if fast-moving neutrals are being ionized, the flow may be acting to accelerate the bulk plasma toward the MFS [50], thereby enhancing the net force. An improved experimental design is ultimately required to investigate and nullify such effects and determine the nature of momentum transfer to the plasma. Considerations for future experimentation are now discussed.

5.4 Experiment Scaling

This experiment has revealed promising insights about the interaction of a stationary magnetized plasma with a hypersonic neutral flow. Here, we discuss how this experiment may scale to conditions relevant for a full validation of the critical ionization and drag effects

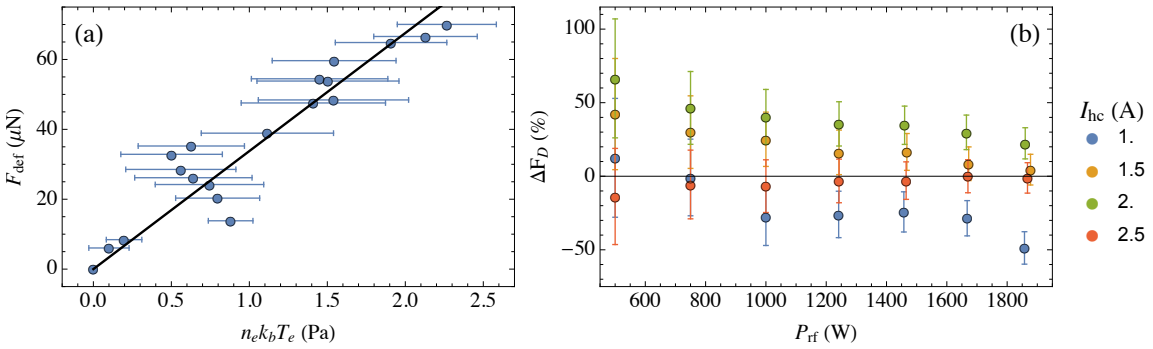

Figure 5.15: (a) Deflection force on MFS target, F_{def}, as a function of the hollow cathode plasma pressure, $n_e k_b T_e$, for I_{hc} ranging from 0.2–2.5 A. (b) Change in drag force on the MFS target compared to the force of the neutral beam with the hollow cathode off.

underlying plasma aerocapture. These conditions dictate that the power incident on the target plasma, P_{target}, should dominate the injected power, P_{inj} [34]. Fig. 5.14 shows this criteria is not met by the current experiment. Additionally, the pumping limitations of the DVF cause a fairly high background pressure of $p_0 \approx 5$ mTorr during experimental operation with 100 sccm Ar. This infringes on the neutral flow interaction with the hollow cathode as the mean free path for collisions with background gas, λ_0, is significantly shorter than the distance the beam travels from the neutralizer plate to the target, d_{plate}. To have a flow interaction dominated by collisions with target plasma ions rather than scattering collisions with background gas, we require $\lambda_0/d_{\text{plate}} > 1$.

In Fig. 5.16 we show the design space of the experimental architecture presented in this paper. The design parameters $\lambda_0/d_{\text{plate}}$ and $P_{\text{target}}/P_{\text{inj}}$ are shown on the horizontal and vertical axes, respectively. The blue region highlights the operating regime of the present experiment which is clearly below the stated requirements. We now map some design parameters onto this regime plot to inform the development of future experiments that may operate in the required regime, shown in green. First, let us assume the incident flow power diminishes as a result of collisions with background neutrals such that $P_{\text{target}} \propto e^{-d_{\text{plate}}/\lambda_0}$. We define the characteristic flow power as $P_{\text{nb},0} = \dot{m}_n u_\infty^2/2$, where $\dot{m}_n$ is the neutral mass flow rate supplied to the beam. Recall that we measured the ratio of energy incident on the target to energy incident on the neutralizer plate in Fig. 5.9 to be 2.7%. Similarly,

Cuthbertson [88] provides a value of 21.7% for the flow energy immediately after reflection compared to the energy striking the plate. Using these as proxies for $P_{\text{target}}/P_{\text{nb,0}}$ at their respective locations of $d_{\text{plate}} = 0$ and 30 cm, we can solve an approximate expression of the incident beam power as a function of distance and mean free path,

$$P_{\text{target}}(d_{\text{plate}}, \lambda_0) \approx \frac{1}{2}\dot{m}_n u_\infty^2 \exp\left(-\frac{d_{\text{plate}}}{11.6\lambda_0}\right). \tag{5.10}$$

Curves of $P_{\text{target}}/P_{\text{inj}}$ are shown in Fig. 5.16 for three different neutral flow rates ($\dot{m}_n = 2$, 10, and 50 mg/s) corresponding to three maximum incident powers ($P_{\text{target}} = 106$ W, 530 W, and 2.6 kW). Here we assume $P_{\text{inj}} = 92$ W from the average of experimental cases at $I_{\text{hc}} = 2.5$ A and $u_\infty = 10$ km/s, which is roughly the averge of cases in our experiment calculated using Eq. (5.1). Note that the curves level off as $\lambda_0/d_{\text{plate}}$ approaches and exceeds unity, at which point the neutral flow rate drives the incident power.

It is clear from the black curves in Fig. 5.16 that mass flow rates of tens of mg/s and mean free paths of tens of cm are required to sustain an incident power sufficient for the desired regime. We wish to determine the capability of an experimental facility to support these requirements. The mean free path for background neutral collisions is $\lambda_0 = (n_n\sigma_0)^{-1}$ for background neutral density n_n and cross section σ_0. In turn, n_n is linked to the background pressure in the chamber, $p_0 = n_n k_b T_n$, for neutral temperature T_n. To maintain a given p_0, a pumping speed $S_{\text{v}} = c_{\text{v}}\dot{m}_n/p_0$ is required, where $c_{\text{v}} = 5.67 \times 10^7$ Pa-L/kg is a constant. Combining these expressions, we obtain a function for the sustainable mass flow rate for a given pumping speed,

$$\dot{m}_n = \frac{k_b T_n S_{\text{v}}}{c_{\text{v}}\sigma_0\lambda_0}. \tag{5.11}$$

By substituting this into Eq. (5.10), we plot level curves of constant S_{v} in Fig. 5.16 from 100 L/s up to 3 ML/s. With a max pumping speed of about 1 kL/s (and an effective speed of 250 L/s under load in the current experiment), the DVF is incapable of reaching the required regime. Fig. 5.16 indicates $S_{\text{v}} > 4$ kL/s is needed to operate in the green region, and in reality, $S_{\text{v}} > 30$ kL/s is required to reach incident powers that far exceed the injected power. To achieve very high neutral flow power such as the 2.6 kW curve shown in Fig. 5.16, a facility with much greater pumping capability ($S_{\text{v}} > 100$ kL/s) is needed. Chambers that test high-power electric propulsion systems are generally well-suited for this type of study

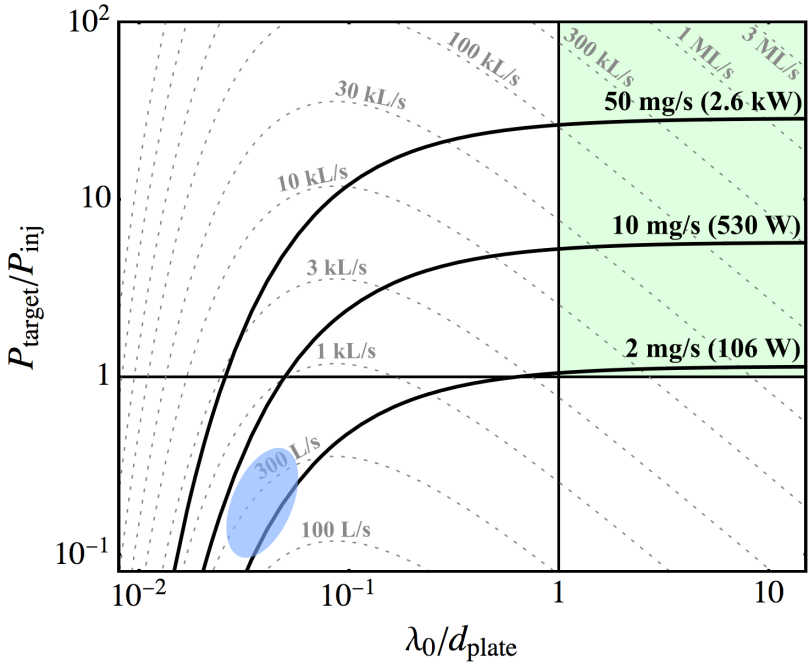

Figure 5.16: The experimental regime map of flow-incident power normalized by injected power on the target plasma, $P_{\text{target}}/P_{\text{inj}}$, and the mean free path for scattering collisions normalized by distance from the neutralizer plate to the target, $\lambda_0/d_{\text{plate}}$. The blue region shows the current experiment's operating regime while the green region shows the desired regime for a comprehensive validation of critical ionization and drag effects for plasma aerocapture. Eq. (5.10) is plotted in black for three neutral flow rates, $\dot{m}_n$, from 2–50 mg/s, corresponding to max incident powers of 106 W–2.6 kW. Gray dashed lines show curves of $P_{\text{target}}/P_{\text{inj}}$ for fixed pumping speeds, S_{v}, from 100 L/s to 3 ML/s.

[102]. To generate a neutral beam of this power, a simple volume-average model of the helicon plasma (similar to [103]) suggests an RF power of >10 kW is needed to generate the high source density required. While the general architecture of this experiment is sound, this scaling suggests major equipment upgrades to the vacuum facility and neutral source would be needed to achieve a comprehensive demonstration of critical ionization and plasma drag.

5.5 Conclusion

In this chapter, we presented for the first time a novel experiment to investigate the interaction of a stationary magnetized plasma with a hypersonic neutral flow. The neutral flow is generated by accelerating ions from a high-power helicon plasma along magnetic field lines to a negatively biased molybdenum plate. After surface neutralization and reflection from the plate, a collimated flow of neutrals impacts an axially-magnetized hollow cathode plasma. Their interaction is analyzed by measuring the target plasma with a Langmuir probe before and during flow operation. A momentum flux sensor is used to determine whether the interaction leads to deflection of the flow indicating drag on the plasma. This work has led to a few key takeaways:

1. We have demonstrated experimentally that there is a transfer of energy from the flow to the target plasma by invoking a power balance model. We find evidence that some of the absorbed energy goes into heating the electron population. While not a full demonstration of the effect, this supports one of the key assumptions of plasma aerocapture that the plasma absorbs flow kinetic energy to sustain a critical ionization discharge.

2. The current experimental setup is insufficient to resolve momentum transfer from the flow to the plasma. However, results suggest there may be higher-order effects dictating the exchange of momentum, such as acceleration of the target plasma or changes to its structure. Ultimately, we cannot draw any conclusions about the hypothesized drag on the magnetized plasma from the current data without improving the signal-to-noise ratio of MFS deflection. Future experiments may mitigate this by increasing the separation between the MFS and plasma and/or reducing the MFS target area with respect to the plasma cross section.

3. This is the first attempt at a plasma/flow interaction experiment using this neutral beam architecture, opening the door to studies with hypersonic free-molecular flows that are absent from literature in recent decades [104, 105]. The neutral beam provides particle flows in the sub-Pa dynamic pressure, several-eV stagnation temperature

regime that cannot be achieved using traditional wind tunnel and arcjet facilities. The device upon which it is based was only 2 cm in diameter and operated in a pulsed mode [88]; we have demonstrated here that it can scale to at least ten times this size and generate steady flows with no indication of performance limitation. With some equipment upgrades to the helicon plasma source and the vacuum chamber, this experiment architecture is capable of demonstrating the elusive critical ionization and plasma drag effects that govern plasma aerocapture performance.

This experiment is a proof-of-concept that justifies more advanced study of plasma aerocapture and opens doors in many other research areas. Previous critical ionization experiments accelerate plasma into a stationary gas and magnetic field [28]. However, there are numerous applications where the inverse is desired, including the progenitor of critical ionization theory in which Alfvén posits neutral gas falling through a magnetized plasma as an origin of planetary satellites [26]. The experimental approach presented here may thus be employed to widen the scope of critical ionization research through the use of a similar neutral flow tool. For example, with a better-confined target plasma, this basic architecture can enable experimental validation of the CX regime from Chapter 3 which cannot practically exist with a flowing plasma configuration. It is also a starting point for a wide variety of other experiments, such as low-altitude spacecraft surface interaction studies, MHD aerobraking demonstrations, and testing particular magnetoshell designs for DMPA. The findings presented here pave the way for such applications and may ultimately enable more sophisticated plasma aerocapture experiments to thoroughly characterize its technological feasibility.

Chapter 6

CONCLUSION

In this dissertation, we have taken a three-pronged approach to assessing the feasibility of plasma aerocapture. First, we developed a novel analytical model to describe the interaction between a magnetoshell and atmospheric gas flow. In this model, we examined how individual neutral particles become ionized and react to the presence of a dipole plasma to gain insight into the physical process of absorbing flow and generating drag force. This newfound understanding informed the development of a global control volume model that solves the nonlinear coupled physics of flow/plasma interaction. We used the global model to determine scaling laws governing the physics and performance of magnetoshells in both argon and hydrogen environments. Second, we developed a framework for the design and analysis of preliminary DMPA mission architectures. This framework couples spacecraft scaling, mission analysis, and, crucially, the self-consistent plasma physics generated by the global model. We also developed a custom trajectory propagator that enables continuously-variable magnetic field drag modulation throughout simulated aerocapture maneuvers. Together, the framework and trajectory simulator allowed us to determine mission applications and characterize DMPA performance against other technologies. Finally, we designed, built, and operated a novel experiment to demonstrate some of the key effects that make plasma aerocapture work. The experiment leveraged a neutral flow tool capable of achieving flow densities and velocities in the regime relevant to upper-atmospheric aerocapture, something most wind tunnels (and previous magnetoshell demonstrations) are unable to achieve.

6.1 Contribution of This Thesis

In Chapter 1, we posed four questions to answer in order to characterize the physics, performance, and feasibility of DMPA. Let us now discuss our findings as they pertain to answering these questions.

Question 1: What are the underlying physical processes governing the interaction between a magnetoshell and neutral flow? In Chapter 2, we find through single-particle simulations that the dipole plasma captures flow particles that are ionized inside a certain boundary, $\psi > \psi^*$, implying that the magnetoshell can absorb mass and energy from the flow. These simulations also reveal that force is imparted on the magnet as a result of magnetically deflecting, capturing, or reflecting flow particles that are ionized by the plasma. In Chapter 3 we discover three physical regimes dictating the steady state behavior of the magnetoshell/flow system. In the I regime, the interaction is dominated by the mass and energy that is artificially injected into the magnetoshell to seed the plasma. A negligible amount of flow is absorbed by the magnetoshell. In the CX regime, charge exchange provides both neutrals to ionize into the plasma and the energy required to ionize them. The magnetoshell is sustained by the flow in this fashion. In the CIV regime, the magnetoshell is still sustained by the flow, except flow neutrals are directly ionized by the electrons. The transition between these regimes is broadly governed by the balance between effective ionization losses, diffusive losses, and energy capture from the flow. While the CIV regime is a classical manifestation of critical ionization, the CX regime is a mode of critical ionization driven by charge exchange that has not been explicitly found in literature until now.

Question 2: How do these physics scale with spacecraft and environmental parameters like magnet size, field strength, velocity, and density? In Chapter 3, we show that, consistent with critical ionization theory, there are threshold velocities marking the transitions between the I, CX, and CIV regimes. The CIV regime may only be met at a velocity that is necessarily higher than Alfvén's critical ionization velocity, u_{cr} [Eq. (3.1)]. However, the CX regime exists below the CIV regime and, in some cases, at velocities lower than u_{cr}. Because the system behavior is dominated by diffusive effects, we also find that there are thresholds for magnetic field strength, density, and magnet size. In any case, transitions between regimes result in massive performance gains for the magnetoshell. For example, going from the I to the CX regime leads to a tenfold increase in drag force and up to a hundredfold increase in mass/energy capture by the magnetoshell.

Crucially, increasing the magnetic field strength even within the CX or CIV regime leads to a monotonic increase in drag force, confirming the ability of magnetoshells to achieve continuously-variable drag modulation through the magnet.

Question 3: What is the implication of this scaling for the use of magnetoshells in aerocapture at atmospheric celestial bodies? Because magnetoshell performance depends on these physical regimes, we determine that the device must leverage the in-situ flow to successfully perform aerocapture. In other words, the magnetoshell must operate in a CX or CIV mode during aerocapture in order to avoid needing massive onboard fuel and power systems. As a result, the CX threshold velocity imposes a lower bound on spacecraft speed, dictating the applicable destinations. DMPA at Mars and Titan, where the velocities to enter into orbit are <5 km/s [1], is likely not possible according to the performance scaling found in Chapter 3. However, magnetoshells may fit into mission architectures that enable fast trip times and therefore much higher entry velocities. DMPA at Earth and Venus, where atmospheric entry velocity is ∼11 km/s, will pose challenges that are not addressed by this thesis.[1] Instead, we focus our attention on the outer planets Jupiter, Saturn, Uranus, and Neptune, where entry velocities are well over 20 km/s (up to 60 km/s) and therefore play into the advantages of magnetoshell performance scaling. For Neptune specifically, we find that a DMPA mission can be feasibly designed with an architecture similar to existing aerocapture concepts. Such a mission would improve the final orbiter mass, reduce heat/pressure loads, and provide greater controllability than its aeroshell-only counterpart. We also find that modulating drag through control of the magnetic field strength is sufficient to achieve trajectory robustness to perturbations in atmospheric density and entry flight path angle. While continuously-variable drag modulation was already known to perform well theoretically [9], the comprehensive findings of Chapters 3 and 4 represent the first presentation of technological feasibility of a device capable of achieving this elusive control scheme.

---

[1]For a discussion of DMPA at Venus, Earth, Mars, and Titan, see [49].

Question 4: Can the feasibility of magnetoshells be experimentally demonstrated before a flight implementation is developed? In Chapter 5, we present the first attempt to demonstrate the physics of magnetoshells experimentally with a DMPA-representative flow environment. The novel experiment architecture is basic and consists of two major elements. A target plasma acting as a magnetoshell stand-in is generated by a hollow cathode with an applied axial magnetic field to enhance density and temperature. The neutral flow is generated by extracting ions from a helicon plasma source, accelerating them to hypersonic velocity, and neutralizing/reflecting them as a collimated beam. The use of this type of neutral flow device enables testing in a low dynamic pressure, high velocity environment that is necessary for DMPA simulation but not possible to achieve with existing wind tunnels. We successfully observe the transfer of energy from the neutral flow to the electron population in the target plasma, a process that is crucial to achieving critical ionization as found in Chapter 3. This confirms experimentally that the magnetoshell can absorb flow energy. Due to limitations in the current experiment, we are unable to confirm that the flow imparts a drag force on the magnetic field. However, we discuss how the experiment may be scaled such that it can successfully demonstrate both plasma drag and critical ionization. While the requirements for such an experiment exceed the capabilities of our current facilities, they are not infeasible with modern laboratory equipment. Therefore, an experimental demonstration of magnetoshell feasibility using the architecture implemented in Chapter 5 is possible.

6.2 Future Work

There are some areas highlighted by this work that warrant further investigation or improvement to the current approach. Recommendations for future work have been discussed throughout this thesis, but they are summarized here for clarity.

- The global model presented in Chapters 2 and 3 had several simplifications that may be expanded in future iterations. The biggest of these is to implement the model using molecular species instead of atomic. A natural next step is to build a model describing an H_2 flow as that more accurately represents the aerocapture environment at the

outer planets, whose atmospheres are majority molecular hydrogen, and involves less complexity than highly interactive species such as air (Earth) or CO_2 (Mars, Venus). Higher physical fidelity may also be achieved by incorporating more realistic density profiles for both plasma and secondary neutrals.

- The analysis of DMPA trajectories at Neptune in Chapter 4 may be conducted with increased atmospheric dispersions, errors in delivery state, and trajectory knowledge uncertainty. Further, while the present work demonstrates feasibility for Neptune, a similar analysis may be conducted for the other three giant planets to determine any advantages of DMPA. Enhancements to the guidance and control algorithm that take advantage of the unique physics of magnetoshell drag modulation will likely improve DMPA performance compared to that presented here.

- The specifics of magnetoshell configuration aboard a spacecraft should be investigated further to determine whether advanced technologies are required. In particular, there is a trade space determining whether to tether or clamp the magnetoshell that, while similar to that for ballutes, is not well understood in the context of DMPA. These tradeoffs must be fleshed out to better understand tethered vehicle dynamics, wake effects on the magnetoshell, potential attitude control during DMPA, and surface-plasma interactions.

- The experiment described in Chapter 5 is a first step toward demonstrating the physics of plasma aerocapture in the laboratory. However, to achieve a full-fledged experimental proof of the critical ionization and drag physics crucial to DMPA, significant facility and equipment upgrades are required. The neutral beam power incident on the target plasma must be increased by at least an order of magnitude while the background pressure of the vacuum chamber must be significantly reduced. These entail pumping speeds of 10$\sim$100 kL/s and RF powers of $\sim$10 kW, both far beyond the capabilities of the present experiment. However, the novel architecture of the experiment presented here may continue to be leveraged in future laboratory investigations.

6.3 Publications

The research conducted in pursuit of this degree has resulted in numerous publications. They are listed here in chronological order.

1. **Kelly, C.** & Shimazu, A. (2017). Revolutionizing Orbit Insertion with Active Magnetoshell Aerocapture. In *35th International Electric Propulsion Conference*. Atlanta, GA.

2. **Kelly, C. L.** (2018). Magnetoshell Aerocapture: Advances Toward Concept Feasibility. University of Washington.

3. **Kelly, C. L.** & Little, J. M. (2019). Energy and Mass Utilization During Drag-Modulated Plasma Aerocapture. In *2019 IEEE Aerospace Conference*. Big Sky, MT.

4. **Kelly, C. L.** & Little, J. M. (2019). Performance Scaling and Mission Applications of Drag-Modulated Plasma Aerocapture. In *36th International Electric Propulsion Conference*. Vienna, Austria.

5. Little, J. M. & **Kelly, C. L.** (2020). Neutral flow interaction with a magnetic dipole plasma: I. Theory and scaling. Physics of Plasmas, 27(11), 113512.

6. **Kelly, C. L.** & Little, J. M. (2020). Neutral flow interaction with a magnetic dipole plasma: II. Global modeling. Physics of Plasmas, 27(11), 113511.

7. **Kelly, C. L.** & Little, J. M. (2021). Performance and Design Scaling of Magnetoshells for Outer Planet Drag-Modulated Plasma Aerocapture. In *2021 IEEE Aerospace Conference*. Virtual Event.

8. **Kelly, C. L.** & Little, J. M. (submitted 2021). Experimental Investigation of Hypersonic Neutral Flow Interaction with a Magnetized Plasma. Plasma Sources Science and Technology (in review).

6.4 Awards

The research conducted in pursuit of this degree has been recognized with various awards, listed chronologically here.

1. *2017 IEPC Young Visionary Award:* First place in paper competition at the 35th International Electric Propulsion Conference for "exceptional skill at promoting new ideas using a unique combination of technical knowledge, foresight, and articulation."

2. *2018 NASA Space Technology Research Fellowship:* Selected as one of 56 graduate students nationwide for a competitive fellowship to conduct PhD research on plasma aerocapture.

3. *2021 A&A Student Excellence Award for Doctoral Research:* Awarded to one doctoral student annually recognizing distinguished achievements and sustained progress in research in the A&A department.

BIBLIOGRAPHY

[1] Jeffery L. Hall, Muriel A. Noca, and Robert W. Bailey. Cost-Benefit Analysis of the Aerocapture Mission Set. *Journal of Spacecraft and Rockets*, 42(2):309–320, 2005.

[2] Stephen J. Hughes, F. McNeil Cheatwood, Anthony M. Calomino, Henry S. Wright, Mary Elizabeth Wusk, and Monica F. Hughes. Hypersonic Inflatable Aerodynamic Decelerator (HIAD)Technology Development Overview. Technical report, NASA Langley Research Center, San Jose, CA, 2013.

[3] Ethiraj Venkatapathy, Kenneth Hamm, Ian Fernandez, James Arnold, David Kinney, Bernard Laub, Alberto Makino, Mary McGuire, Keith Peterson, Dinesh Prabhu, David Empey, Ian Dupzyk, Loc Huynh, Prabhat Hajela, Peter Gage, Austin Howard, and Dana Andrews. Adaptive Deployable Entry and Placement Technology (ADEPT): A Feasibility Study for Human Missions to Mars. In *21st AIAA Aerodynamic Decelerator Systems Technology Conference and Seminar*, Dublin, Ireland, may 2011. American Institute of Aeronautics and Astronautics.

[4] Reuben R Rohrschneider and Robert D Braun. Survey of Ballute Technology for Aerocapture. *Journal of Spacecraft and Rockets*, 44(1):10–23, 2007.

[5] Thomas R Spilker, James A. Cutts, Evgeniy Sklyanskiy, Eric M. Slimko, and Patricia M. Beauchamp. Atmospheric Entry Conditions for Planetary Missions. In *10th VEXAG Meeting*, Washington, DC, 2012.

[6] Thomas R. Spilker, Mark Adler, Nitin Arora, Patricia M. Beauchamp, James A. Cutts, Michelle M. Munk, Richard W. Powell, Robert D. Braun, and Paul F. Wercinski. Qualitative Assessment of Aerocapture and Applications to Future Missions. *Journal of Spacecraft and Rockets*, pages 1–10, 2018.

[7] P Wercinski, A Austin, A Nelessen, B Strauss, K Hogstrom, D Landau, E Luthman, J Ravich, M Lobbia, G Allen, A Cassell, D Prabhu, B Yount, and E Venkatapathy. A Neptune Orbiter Concept using Drag Modulated Aerocaptue (DMA) and the Adaptable , Deployable Entry and Placement Technology (ADEPT). In *Outer Planets Assessment Group Meeting*, 2019.

[8] G. Falcone, J. W. Williams, and Z. R. Putnam. Assessment of aerocapture for orbit insertion of small satellites at Mars. *Journal of Spacecraft and Rockets*, 56(6):1689–1703, 2019.

[9] Zachary R. Putnam and Robert D. Braun. Drag-Modulation Flight-Control System Options for Planetary Aerocapture. *Journal of Spacecraft and Rockets*, 51(1):139–150, jan 2014.

[10] John Slough, David Kirtley, and Anthony Pancotti. Plasma Magnetoshell for Aerobraking and Aerocapture. In *32nd International Electric Propulsion Conference*, Wiesbaden, Germany, 2011.

[11] Michelle McClary and Zachary R. Putnam. Assessment of Hypersonic Separation Dynamics For Drag Modulation Systems at Mars. In *AIAA SciTech Forum*, Virtual Event, 2021.

[12] Kazuhiko Yamada, Yasunori Nagata, Takashi Abe, Kojiro Suzuki, Osamu Imamura, and Daisuke Akita. Suborbital reentry demonstration of inflatable flare-type thin-membrane aeroshell using a sounding rocket. *Journal of Spacecraft and Rockets*, 52(1):275–284, 2015.

[13] R Keith Johnson, F Mcneil Cheatwood, Anthony M Calomino, Stephen J Hughes, Ashley M Korzun, John M Dinonno, and Mike C Lindell. HIAD Advancements and Extension of Mission Applications. In *International Planetary Probe Workshop*, Laurel, MD, 2016.

[14] Alan M Cassell, Paul F Wercinski, Ethiraj Venkatapathy, Michael Aftosmis, and Michael C Wilder. Adaptive Deployable Entry Placement Technology (ADEPT) Development for Small Sat Class Venus Missions. In *Venus Exploration Analysis Group 16th Meeting*, Laurel, MD, 2018.

[15] David Kirtley. A Plasma Aerocapture and Entry System for Manned Missions and Planetary Deep Space Orbiters. Technical report, 2014.

[16] Bret G. Drake, Stephen J. Hoffman, and David W. Beaty. Human Exploration of Mars, Design Reference Architecture 5.0. In *2010 IEEE Aerospace Conference*. IEEE, 2010.

[17] Robert Bailey, Jeffrey Hall, Thomas Spilker, and Nora O'Kongo. Neptune Aerocapture Mission and Spacecraft Design Overview. In *Joint Propulsion Conference and Exhibit*, Reston, Virigina, jul 2004. American Institute of Aeronautics and Astronautics.

[18] Sean M. Hancock, Robert W. Moses, and Christopher Goyne. Magnetoshell Aerocapture Performance Opportunities at Mars. In *2018 AIAA SPACE and Astronautics Forum and Exposition*, number September, pages 1–14, 2018.

[19] David Kirtley. ISS Launched CubeSat Demonstration of Variable-Drag Magnetoshell Aerocapture: Phase I Final Report. Technical report, 2014.

[20] Charles L. Kelly. *Magnetoshell Aerocapture: Advances Toward Concept Feasibility.* Master's thesis, University of Washington, 2018.

[21] Charles L. Kelly and Justin M. Little. Energy and Mass Utilization During Drag-Modulated Plasma Aerocapture. In *2019 IEEE Aerospace Conference*, Big Sky, MT, 2019.

[22] Erik T. Karlson. Streaming of a plasma through a magnetic dipole field. *Physics of Fluids*, 6(5):708, 1963.

[23] Oscar Buneman, Torsten Neubert, and Ken-Ichi Nishikawa. Solar wind-magnetosphere Interaction as Simulated by a 3-D EM Particle Code. *IEEE Transactions on Plasma Science*, 20(6):810–816, 1992.

[24] A. Hasegawa, Liu Chen, and M. E. Mauel. A D-3He fusion reactor based on a dipole magnetic field. *Nuclear Fusion*, 30(11):2405–2413, 1990.

[25] R. M. Winglee, J. Slough, T. Ziemba, and A. Goodson. Mini-Magnetospheric Plasma Propulsion: Tapping the energy of the solar wind for spacecraft propulsion. *Journal of Geophysical Research: Space Physics*, 105(A9):21067–21077, 2000.

[26] H. Alfvén and J. M. Wilcox. On the origin of the satellites and the planets. *Astrophysical Journal*, 136:1016–1022, 1962.

[27] Nils Brenning. Review of the CIV phenomenon. *Space Science Reviews*, 59:209–314, 1992.

[28] A. Piel. Review of laboratory experiments on Alfven's critical ionization velocity. *Advances in Space Research*, 10(7):7–16, 1990.

[29] S. Machida and C. K. Goertz. A simulation study of the critical ionization velocity process. *Journal of Geophysical Research*, 91(A11):11965–11976, 1986.

[30] S Machida and C K Goertz. The Electromagnetic Effect on the Critical Ionization Velocity Process. *Journal of Geophysical Research*, 93(A10):11495–11506, 1988.

[31] M. A. Raadu. The role of electrostatic instabilities in the critical ionization velocity mechanism. *Astrophysics and Space Science*, 55(1):125–138, 1978.

[32] William J. McNeil, Shu T. Lai, and Edmond Murad. Interplay between collective and collisional processes in critical velocity ionization. *Journal of Geophysical Research*, 95(A7):10345–10356, 1990.

[33] E Möbius, K Papadopoulos, and A Piel. On the turbulent heating and the threshold condition in the critical ionization velocity interaction. *Planetary and Space Science*, 35(3):345–352, 1987.

[34] Justin M. Little and Charles L. Kelly. Neutral flow interaction with a magnetic dipole plasma: I. Theory and scaling. *Physics of Plasmas*, 27(11):113512, 2020.

[35] Charles L. Kelly and Justin M. Little. Neutral flow interaction with a magnetic dipole plasma: II. Global modeling. *Physics of Plasmas*, 27(11):113511, 2020.

[36] J. D. Jackson. *Classical Electrodynamics*. John Wiley & Sons, Inc, New York, 1962.

[37] A.C. Hindmarsh and L.R. Petzold. LSODA, Ordinary Differential Equation Solver for Stiff or Non-Stiff System, 2005.

[38] James A. Rome and Y-K.M.‘ Peng. The topology of tokamak orbits. *Nuclear Fusion*, 19(9):1193, 1979.

[39] J. Kesner, D. T. Garnier, and M. E. Mauel. Fluctuation driven transport and stationary profiles. *Physics of Plasmas*, 18(5), 2011.

[40] Matthew S. Davis, M. E. Mauel, Darren T. Garnier, and Jay Kesner. Pressure profiles of plasmas confined in the field of a magnetic dipole. *Plasma Physics and Controlled Fusion*, 56(9), 2014.

[41] Sergei I. Krasheninnikov, Peter J. Catto, and R. D. Hazeltine. Magnetic dipole equilibrium solution at finite plasma pressure. *Physical Review Letters*, 82(13):2689–2692, 1999.

[42] E. T. Meier and U. Shumlak. A general nonlinear fluid model for reacting plasma-neutral mixtures. *Physics of Plasmas*, 19(7), 2012.

[43] Kazunori Takahashi and Akira Ando. Laboratory Observation of a Plasma-Flow-State Transition from Diverging to Stretching a Magnetic Nozzle. *Physical Review Letters*, 118(22), 2017.

[44] S. I. Braginskii. Transport processes in a plasma, 1965.

[45] Michael A. Lieberman and Allan J. Lichtenberg. *Principles of Plasma Discharges and Materials Processing*. Hoboken, NJ, second edition, 2005.

[46] Robert J Goldston and Paul H Rutherford. *Introduction To Plasma Physics*, volume 01. Institute of Physics Publishing, Bristol and Philadelphia, 1995.

[47] M. Vellante, M. Piersanti, and E. Pietropaolo. Comparison of equatorial plasma mass densities deduced from field line resonances observed at ground for dipole and IGRF models. *Journal of Geophysical Research: Space Physics*, 119:2623, 2014.

[48] D. T. Garnier, A. C. Boxer, J. L. Ellsworth, J. Kesner, and M. E. Mauel. Confinement improvement with magnetic levitation of a superconducting dipole. *Nuclear Fusion*, 49, 2009.

[49] Charles L. Kelly and Justin M. Little. Performance Scaling and Mission Applications of Drag-Modulated Plasma Aerocapture. In *36th International Electric Propulsion Conference*, Vienna, 2019.

[50] J. F. McKenzie and R. K. Varma. The interaction of a moving neutral gas with a stationary magnetized plasma. *Journal of Plasma Physics*, 25(3):491–497, 1981.

[51] B. Lehnert. Ionization process of a plasma. *Physics of Fluids*, 9(4):774, 1966.

[52] Lars Danielsson. Experiment on the interaction between a plasma and a neutral gas. *Physics of Fluids*, 13(9):2288–2294, 1970.

[53] G. Himmel, E. Möbius, and A. Piel. Investigation of the Structure and the Plasma Parameters in a Critical Velocity Rotating Plasma. *Zeitschrift fur Naturforschung - Section A Journal of Physical Sciences*, 31(8):934–941, 1976.

[54] N. Venkataramani and S. K. Mattoo. Plasma retardation in Alfvén's critical velocity phenomenon. *Physics Letters A*, 79A(5,6):393–398, 1980.

[55] N. Brenning and I. Axnäs. Critical ionization velocity interaction: some unsolved problems. *Astrophysics and Space Science*, 144:15–30, 1988.

[56] Sumire Kobayashi, Barrett N. Rogers, and William Dorland. Gyrokinetic simulations of turbulent transport in a ring dipole plasma. *Physical Review Letters*, 103(5):1–4, 2009.

[57] M. H. Brennan and R. Morrow. Proton-hydrogen atom momentum transfer cross section at approximately 5 eV. *Journal of Physics B: Atomic and Molecular Physics*, 4(7), 1971.

[58] C F Barnett, J A Ray, E Ricci, M I Wilker, E W McDaniel, E W Thomas, and H B Gilbody. *Atomic Data for Controlled Fusion Research*. 1977.

[59] Peter Banks. Collision frequencies and energy transfer: Electrons. *Planetary and Space Science*, 14(11):1085–1103, 1966.

[60] G. S. Voronov. A practical fit formula for ionization rate coefficients of atoms and ions by electron impact: Z = 1-28. *Atomic Data and Nuclear Data Tables*, 65:1–35, 1997.

[61] Justin M Little. Performance Scaling of Magnetic Nozzles for Electric Propulsion. (January), 2015.

[62] JV Dugan and RJ Sovie. Volume ion production costs in tenuous plasmas: A general atom theory and detailed results for helium, argon, and cesium. Technical report, NASA Lewis Research Center, Cleveland, Ohio, 1967.

[63] Ping Lu, Christopher J. Cerimele, Michael A. Tigges, and Daniel A. Matz. Optimal Aerocapture Guidance. *Journal of Guidance, Control, and Dynamics*, 38(4):553–565, 2015.

[64] N. X. Vinh. *Studies in Astronautics 2: Optimal Trajectories in Atmospheric Flight.* Elsevier Scientific Publishing Company, Amsterdam, The Netherlands, 1981.

[65] Athul P. Girija, Sarag J. Saikia, James M. Longuski, and James A. Cutts. AMAT: A Python package for rapid conceptual design of aerocapture and atmospheric Entry, Descent, and Landing (EDL) missions in a Jupyter environment. *Journal of Open Source Software*, 6(67):3710, 2021.

[66] E Venkatapathy, A Austin, A Cassell, D Ellerby, J Elliott, P Gage, M Lobbia, A Nelessen, D Prabhu, B Strauss, and P Wercinski. Enabling Entry Technologies for Ice Giant Missions. In *Ice Giants Systems*, page 2020, London, UK, 2020.

[67] Kenneth Sutton and Jr. Graves, Randolph A. A general stagnation-point convective-heating equation for arbitrary gas mixtures. Technical report, Langley Research Center, Hampton, VA, 1971.

[68] Panasonic. Lithium Ion NCR18650B Datasheet, 2012.

[69] Richard R. Hofer, Benjamin A. Jorns, James E. Polk, Ioannis G. Mikellides, and John Steven Snyder. Wear test of a magnetically shielded Hall thruster at 3000 seconds specific impulse. *33rd International Electric Propulsion Conference*, pages 1–24, 2013.

[70] Elizabeth Kolawa. Extreme Environments Technologies for Future Space Science Missions. Technical report, NASA Jet Propulsion Laboratory, Pasadena, CA, 2007.

[71] Sarah W.H. Shark, Scott J. Hall, Benjamin A. Jorns, Richard R. Hofer, and Dan M. Goebel. High power demonstration of a 100 kW nested hall thruster system. In *AIAA Propulsion and Energy Forum and Exposition, 2019*, Indianapolis, IN, 2019.

[72] National Aeronautics and Space Administration. Ice Giants Pre-Decadal Survey Mission Study Report. 2017.

[73] Mary Kae Lockwood, Karl T Edquist, Brett R Starr, Brian R Hollis, Glenn A Hrinda, Robert W Bailey, Jeffery L Hall, Thomas R Spilker, Muriel A Noca, N O 'kongo, Robert J Haw, Carl G Justus, Aleta L Duvall, Vernon W Keller, James P Masciarelli, David A Hoffman, Jeremy R Rea, Carlos H Westhelle, Claude A Graves, Naruhisa Takashima, Kenneth Sutton, Joseph Olejniczak, Y K Chen, Michael J Wright, Bernard Laub, Dinesh Prabhu, R Eric Dyke, and Ramadas K Prabhu. Aerocapture Systems Analysis for a Neptune Mission. Technical report, NASA Langley Research Center, Hampton, VA, 2006.

[74] Athul Pradeepkumar Girija, Sarag J. Saikia, James M. Longuski, Shyam Bhaskaran, Matthew S. Smith, and James A. Cutts. Feasibility and Performance Analysis of Neptune Aerocapture Using Heritage Blunt-Body Aeroshells. *Journal of Spacecraft and Rockets*, pages 1–18, 2020.

[75] Ethiraj Venkatapathy, Donald Ellerby, Peter Gage, Dinesh Prabhu, Matthew Gasch, Cole Kazemba, Charles Kellerman, Sarah Langston, Benjamin Libben, Milad Mahzari, Frank Milos, Alexander Murphy, Owen Nishioka, Keith Peterson, Carl Poteet, Scott Splinter, Margaret Stackpoole, Joseph Williams, and Zion Young. Entry System Technology Readiness for Ice-Giant Probe Missions. *Space Science Reviews*, 216(22), 2020.

[76] Robert D Braun. Planetary Entry, Descent and Landing (EDL Shortcourse), 2008.

[77] Rohan G. Deshmukh, Jannuel V. Cabrera, and David A. Spencer. Smallsat aerocapture using a generalized numerical predictor corrector guidance architecture. In *AIAA Scitech 2021 Forum*, Virtual Event, 2021.

[78] Kevin L Miller, Doug Gulick, Jake Lewis, Bill Trochman, Jim Stein, Daniel T Lyons, and Richard G Wilmoth. Trailing Ballute Aerocapture: Concept and Feasibility Assessment. In *Joint Propulsion Conference and Exhibit*, 2003.

[79] Rohan G. Deshmukh, David A. Spencer, and Soumyo Dutta. Investigation of direct force control for aerocapture at Neptune. *Acta Astronautica*, 175(September 2019):375–386, 2020.

[80] Hongwei Han, Dong Qiao, and Hongbo Chen. Optimal ballistic coefficient control for Mars aerocapture. In *2016 Chinese Guidance, Navigation, and Control Conference*, Nanjing, China, 2016. IEEE.

[81] Evan Roelke. Multi-Event Drag Modulation Aerocapture Guidance Under Uncertainty AAS 20-566 MULTI-EVENT DRAG MODULATION AEROCAPTURE

GUIDANCE. In *AAS/AIAA Astrodynamics Specialist Conference*, South Lake Tahoe, CA, 2020.

[82] Evan Roelke, Jay W. McMahon, Robert D. Braun, and Philip D. Hattis. Multi-Event Jettison Guidance Approaches for Drag-Modulation Aerocapture. *Journal of Spacecraft and Rockets*, pages 1–13, 2021.

[83] Patrick T. Newell. Review of the critical ionization velocity effect in space. *Reviews of Geophysics*, 23(1):93–104, 1985.

[84] Jeremiah Brackbill, Jean Luc Cambier, Natalia E. Gimelshein, and Sergey F. Gimelshein. Numerical analysis of neutral entrainment effect on field-reversed configuration thruster efficiency. *Journal of Propulsion and Power*, 30(6):1450–1458, 2014.

[85] Robert W. Moses. Regenerative aerobraking. *AIP Conference Proceedings*, 746:1361–1370, 2005.

[86] Daniel R. Smith, David E. Gildfind, Peter A. Jacobs, Timothy G. Cullen, Christopher M. James, Yu Liu, Rowan Gollan, and Timothy J. McIntyre. Magnetohydrodynamic drag measurements in an expansion tunnel with argon test gas. *AIAA Journal*, 58(10):4495–4504, 2020.

[87] Charles L. Kelly and Justin M. Little. Performance and Design Scaling of Magnetoshells for Outer Planet Drag-Modulated Plasma Aerocapture. In *IEEE Aerospace Conference*, Virtual Event, 2021.

[88] John William Cuthbertson. *Reflection of plasma ions from metals (and its use as a hyperthermal neutral beam source)*. PhD thesis, Princeton University, 1991.

[89] John W. Cuthbertson, Robert W. Motley, and William D. Langer. High-flux source of low-energy neutral beams using reflection of ions from metals. *Review of Scientific Instruments*, 63(11):5279–5288, 1992.

[90] Ryan K. Ham, John D. Williams, Seth J. Thompson, and Shawn C. Farnell. A Low Erosion Instant Start Ignition Process for Heaterless Hollow Cathodes. In *AIAA Propulsion and Energy Forum*, page 3377, Virtual Event, 2021.

[91] F. Fietzke and B. Zimmermann. Plasma characterization and technological application of a hollow cathode plasma source with an axial magnetic field. *Surface and Coatings Technology*, 205(5):1491–1496, 2010.

[92] Donald G. Chavers and Franklin R. Chang-Diaz. Momentum flux measuring instrument for neutral and charged particle flows. *Review of Scientific Instruments*, 73(10):3500–3507, oct 2002.

[93] Benjamin W. Longmier, Bryan M. Reid, Alec D. Gallimore, Franklin R. Chang-Diaz, Jared P. Squire, Tim W. Glover, Greg Chavers, and Edgar A. Bering. Validating a Plasma Momentum Flux Sensor to an Inverted Pendulum Thrust Stand. *Journal of Propulsion and Power*, 25(3):746–752, 2009.

[94] Daisuke Kuwahara, Yushi Koyama, Shuhei Otsuka, Takamichi Ishii, Hiroki Ishii, Hiroaki Fujitsuka, Shimpei Waseda, and Shunjiro Shinohara. Development of direct thrust measurement system for the completely electrodeless helicon plasma thruster. *Plasma and Fusion Research*, 9(2), 2014.

[95] Michael D. West, Christine Charles, and Rod W. Boswell. A high sensitivity momentum flux measuring instrument for plasma thruster exhausts and diffusive plasmas. *Review of Scientific Instruments*, 80(5):053509, may 2009.

[96] Robert B. Lobbia and Brian E. Beal. Recommended practice for use of langmuir probes in electric propulsion testing. *Journal of Propulsion and Power*, 33(3):566–581, 2017.

[97] Tianliang Zhang, Ruilin Cui, Wanying Zhu, Qian Yuan, Jiting Ouyang, Kaiyin Jiang, Haibao Zhang, Chenwen Wang, and Qiang Chen. Influence of neutral depletion on blue core in argon helicon plasma. *Physics of Plasmas*, 28(7), 2021.

[98] Y. Y. Lin Wang and J. V. Sengers. Drag force on objects in the nearly free molecular flow regime as a function of speed ratio. Technical report, Institute for Molecular Physics, College Park, MD, 1974.

[99] S. Yoshikawa and D. J. Rose. Anomalous diffusion of a plasma across a magnetic field. *Physics of Fluids*, 5(3):334–340, 1962.

[100] Hideo Okuda and John M. Dawson. Theory and numerical simulation on plasma diffusion across a magnetic field. *Physics of Fluids*, 16(3):408–426, 1973.

[101] A. V. Phelps. Cross Sections and Swarm Coefficients for Nitrogen Ions and Neutrals in N2 and Argon Ions and Neutrals in Ar for Energies from 0.1 eV to 10 keV. *Journal of Physical and Chemical Reference Data*, 20(3):557–573, 1991.

[102] James S. Sovey, Robert H. Vetrone, Stanley P. Grisnik, Roger M. Myers, and James E. Parkes. Test facilities for high-power electric propulsion. *Journal of Propulsion and Power*, 10(1):18–24, 1994.

[103] Kazunori Takahashi, Atsushi Komuro, and Akira Ando. Effect of source diameter on helicon plasma thruster performance and its high power operation. *Plasma Sources Science and Technology*, 24(5), 2015.

[104] A. P. Nikiforov and A. I. Omelik. An aerodynamic wake in a hypersonic free-molecular gas flow. *Fluid Dynamics*, 11:168–171, 1976.

[105] M. Cevdet Celenligil and James N. Moss. Hypersonic rarefied flow about a delta wing-direct simulation and comparison with experiment. *AIAA 26th Thermophysics Conference, 1991*, 30(8):2017–2023, 1991.

[106] Yukikazu Itikawa. Effective collision frequency of electrons in atmospheric gases. *The Physics of Fluids*, 16:831–835, 1973.

[107] K. G. Harstad. Transport equations for gases and plasmas obtained by the 13-moment method - a summary. Technical report, NASA Jet Propulsion Lab, Pasadena, CA, 1968.

[108] B. M. Smirnov. *Introduction to Plasma Physics.* Mir, Moscow, 1977.

Appendix A

GLOBAL PLASMA MODEL IMPLEMENTATION

Here we detail the implementation of the plasma model developed for Chapters 2 and 3. All units are SI (with temperatures in J) unless otherwise specified.

Coulomb interaction

Braginskii[44] defines the ion-electron collision time as

$$\tau_{ie} = \frac{m_i}{m_e} \frac{3.44 \times 10^{11}}{\ln \Lambda e^{3/2}} \frac{T_e^{3/2}}{n_e} \tag{A.1}$$

after converting from cgs units to SI, where $\ln \Lambda$ is the Coulomb logarithm. The normalized form of this appearing in Eqs. (2.67) and (2.68) is

$$\hat{\tau}_{ie} = \frac{3.44 \times 10^{11}}{\ln \Lambda e^{3/2}} \frac{T_\infty^{3/2} u_\infty}{n_\infty r_c} \ . \tag{A.2}$$

Plasma diffusion

The Bohm diffusion coefficient D_B is given by Lieberman and Lichtenberg[45] as

$$D_B = \frac{T_e}{16eB} \ , \tag{A.3}$$

where e is the elementary charge. For electron diffusion due to collisions with heavy particles, the diffusion coefficient D_c is given by Goldston and Rutherford[46] as

$$D_c = \frac{m_e(\nu_{ei} + \nu_{en})}{e^2 B^2}(T_e + T_i) \ , \tag{A.4}$$

where ν_{ei} and ν_{en} are the electron-ion and electron-neutral collision frequencies respectively. The electron-ion collision frequency is given by Goldston and Rutherford[46], Eq. (11.22), as a function of n_i and T_e,

$$\langle \nu_{ei} \rangle = \frac{\sqrt{2} e^4 \ln \Lambda}{12 \pi^{3/2} \varepsilon_0^2 \sqrt{m_e}} \frac{n_i}{T_e^{3/2}} \ , \tag{A.5}$$

where ε_0 is the vacuum permittivity. The electron-neutral collision frequency is modeled by Itikawa [106] as

$$\langle \nu_{en} \rangle = \frac{8}{3} \left(\frac{2\pi T_e}{m_e} \right)^{1/2} \sigma_{en} n_{2n} \tag{A.6}$$

where σ_{en} is the average electron-neutral momentum transfer cross section. Energy-dependent values of σ_{en} are sourced from Harstad [107]. The normalized forms of these diffusion coefficients appearing in Eqs. (2.64), (2.67), and (2.68) are

$$\hat{D}_B = \frac{T_\infty}{16 e B_0 r_c u_\infty} \ , \tag{A.7}$$

$$\hat{D}_c = \frac{m_e T_\infty n_\infty}{e^2 B_0^2 r_c u_\infty I_{\psi^\alpha}} \left(\bar{\nu}_{ei} \hat{N}_i + \bar{\nu}_{en} \hat{N}_{2n} \right) \ , \tag{A.8}$$

where $\bar{\nu}_{ej} = \langle \nu_{ej} \rangle / n_j$ is defined to remove the spatial dependence of D_c. Note that $\hat{D}_c$ depends on model ouputs $\hat{N}_i$ and $\hat{N}_{2n}$ and thus changes with time.

Argon Model

Empirical data on reaction rates and cross sections for argon are compiled from various sources. We identify these here.

Charge exchange The charge exchange reaction rate is modeled after Meier and Shumlak [42]. After integrating over the distribution function to find $\langle \sigma v \rangle$, they obtain

$$\dot{n}_i^{\text{cx}} \approx n_i n_n \sigma_{\text{cx}} V_{\text{cx}} \ , \tag{A.9}$$

where n_n is the neutral species density and V_{cx} is an effective collision velocity. In our model there are two neutral species. The two effective velocities are

$$V_{\text{cx},sn} = \sqrt{\frac{4}{\pi} v_{T,i}^2 + u_\infty^2} \ , \tag{A.10}$$

$$V_{\text{cx},2n} = \sqrt{\frac{4}{\pi} \left(v_{T,i}^2 + v_{T,2n}^2 \right)} \tag{A.11}$$

for thermal velocities $v_{T,j}$. The CX cross section, $\sigma_{\text{cx}}(V_{\text{cx}})$ is sourced from Phelps [101] using the effective velocity to calculate the collision energy. The heat transfer associated with CX between species j and k is described by Meier and Shumlak[42] with the parameter $Q_{j,k}$

that depends on thermal and fluid velocities. After normalization, the heat transfer term appearing in Eqs. (2.67) and (2.69) is

$$\hat{Q}_{j,k} = \frac{\hat{v}_{T,k}^2}{\sigma_{cx} n_\infty r_c} \sqrt{\frac{4}{\pi}\hat{v}_{T,j}^2 + \frac{64}{9\pi}\hat{v}_{T,k}^2 + \hat{v}_{j,k}^2} \ , \tag{A.12}$$

$$\hat{v}_{T,j} = \frac{\sqrt{2T_j/m_j}}{u_\infty} \ , \tag{A.13}$$

$$\hat{v}_{j,k} = \frac{u_j - u_k}{u_\infty} \ , \tag{A.14}$$

where σ_{cx} is that for j-k charge exchange.

Ionization The ionization reaction rate is given analytically by Table 3.3 of Lieberman and Lichtenberg [45] as

$$R_{\text{iz}} = 2.34 \times 10^{-14} T_e^{0.59} \exp(-17.44/T_e) \tag{A.15}$$

for T_e in eV. The effective ionization cost, ϵ_{ion}, is also given in eV units by Lieberman and Lichtenberg in Eq. (3.5.8) as

$$\epsilon_{\text{ion}} = (R_{\text{iz}} U_{\text{iz}} + R_{\text{ex}} U_{\text{ex}} + 3M_{e/i} R_{\text{el}} T_e)/R_{\text{iz}} \tag{A.16}$$

for T_e in eV. Here, $U_{\text{ex}} = 12.14$ eV is the first excitation energy of argon and $U_{\text{iz}} = 15.76$ eV is the first ionization energy. R_{el} and R_{ex} are the elastic scattering and first excitation reaction rates, respectively, and are also given in Table 3.3 as

$$\begin{aligned} R_{\text{el}} &= 2.336 \times 10^{-14} T_e^{1.609} \\ &\quad \times \exp\left[0.0618 \ln(T_e)^2 - 0.1171 \ln(T_e)^3\right] , \end{aligned} \tag{A.17}$$

$$R_{\text{ex}} = 2.48 \times 10^{-14} T_e^{0.33} \exp(-12.78/T_e) \tag{A.18}$$

for T_e in eV.

Neutral diffusion Lieberman and Lichtenberg[45] give a general form for gas diffusion, which adapt for two collision types, $2n$-$2n$ gas-kinetic and i-$2n$ momentum transfer. This yields the secondary neutral diffusion coefficient,

$$D_{2n} = \left(n_i \sigma_{Q_m} + n_{2n} \sigma_{gk}\right)^{-1} \left(\frac{\pi T_{2n}}{m_{2n}}\right)^{1/2} \ , \tag{A.19}$$

where σ_{Q_m} and σ_{gk} are the cross sections of ion-neutral momentum transfer and neutral-neutral collisions respectively. The Ar-Ar^+ momentum transfer cross section, σ_{Q_m}, is sourced from Phelps[101]. We use the highest tabulated value, 1.57×10^{-18} m^2, to represent a worst-case diffusion of secondary neutrals, noting that this value changes by less than a factor of two over the energy range of interest for this study. The gas-kinetic cross section, $\sigma_{gk} = 5 \times 10^{-19}$ m^2, is given by Lieberman[45] in Table 9.3, reproduced from Smirnov[108]. The normalized diffusion coefficient appearing in Eqs. (2.65) and (2.69) is

$$\hat{D}_{2n} = \left(\frac{4\pi}{3}\right)^{1/2} \left(\frac{\hat{N}_i}{\hat{\lambda}_{Q_m}} + \frac{\hat{N}_{2n}}{\hat{\lambda}_{gk}}\right)^{-1} . \tag{A.20}$$

Note again that $\hat{D}_{2n}$ is dependent on model outputs $\hat{N}_i$ and $\hat{N}_{2n}$ and thus varies with time.